AD-A118 288 PENNSYLVANIA STATE UNIV UNIVERSITY PARK APPLIED RESE--ETC F/G 20/11
VARIATION OF THE PINNING FORCE WITH MICROSTRUCTURE AND WITH THE--ETC(U)
SEP 81 P J JAVIER N00024-79-C-6043
UNCLASSIFIED ARL/PSU/TM-81-182 NL

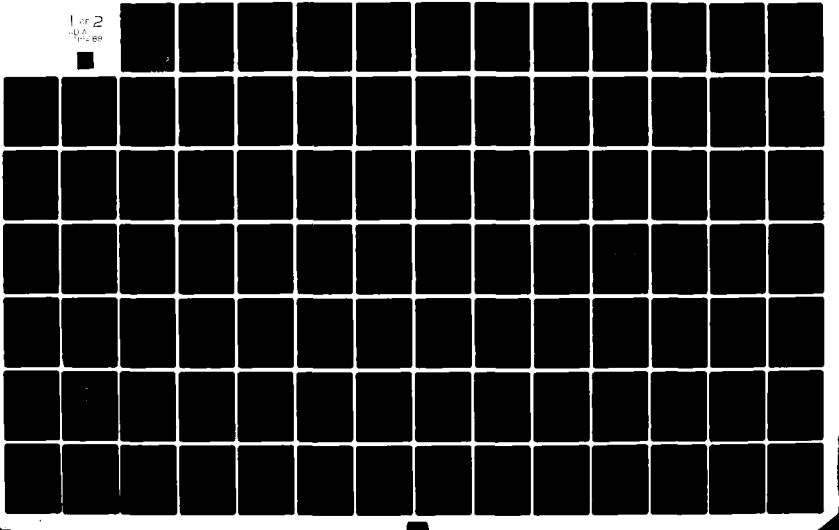

(6)

VARIATION OF THE PINNING FORCE WITH MICROSTRUCTURE AND WITH THE GINZBURG-LANDAU PARAMETER IN TYPE II SUPERCONDUCTORS

Pedro J. Javier

Technical Memorandum
File No. TM 81-182
September 1, 1981
Contract No. N00024-79-C-6043

Copy No. 9

The Pennsylvania State University
Intercollege Research Programs and Facilities
APPLIED RESEARCH LABORATORY
Post Office Box 30
State College, PA 16801

NAVY DEPARTMENT

NAVAL SEA SYSTEMS COMMAND

UNCLASSIFIED

SECURITY CLASSIFICATION OF THIS PAGE *(When Data Entered)*

REPORT DOCUMENTATION PAGE		READ INSTRUCTIONS BEFORE COMPLETING FORM
1. REPORT NUMBER 81-182	2. GOVT ACCESSION NO. AD-A118288	3. RECIPIENT'S CATALOG NUMBER
4. TITLE *(and Subtitle)* VARIATION OF THE PINNING FORCE WITH MICROSTRUCTURE AND WITH THE GINZBURG-LANDAU PARAMETER IN TYPE II SUPERCONDUCTORS		5. TYPE OF REPORT & PERIOD COVERED Ph.D. Thesis, August 1982 6. PERFORMING ORG. REPORT NUMBER 81-182
7. AUTHOR(s) Pedro J. Javier		8. CONTRACT OR GRANT NUMBER(s) N00024-79-C-6043
9. PERFORMING ORGANIZATION NAME AND ADDRESS The Pennsylvania State University Applied Research Laboratory, P.O. Box 30 State College, PA. 16801		10. PROGRAM ELEMENT, PROJECT, TASK AREA & WORK UNIT NUMBERS
11. CONTROLLING OFFICE NAME AND ADDRESS Naval Sea Systems Command Department of the Navy Washington, DC 20362		12. REPORT DATE September 1, 1981 13. NUMBER OF PAGES 177 pages
14. MONITORING AGENCY NAME & ADDRESS*(if different from Controlling Office)*		15. SECURITY CLASS. *(of this report)* Unclassified, Unlimited 15a. DECLASSIFICATION/DOWNGRADING SCHEDULE

16. DISTRIBUTION STATEMENT *(of this Report)*

Approved for public release, distribution unlimited,
per NSSC (Naval Sea Systems Command), 10/1/81

17. DISTRIBUTION STATEMENT *(of the abstract entered in Block 20, if different from Report)*

18. SUPPLEMENTARY NOTES

19. KEY WORDS *(Continue on reverse side if necessary and identify by block number)*

thesis, vanadium, pinning, force

20. ABSTRACT *(Continue on reverse side if necessary and identify by block number)*

The variation of the pinning force with microstructure and with the Ginzburg-Landau parameter is studied for 53 vanadium and vanadium alloy specimens. Vanadium-carbide precipitates are used as pinning centers. The Ginzburg-Landau parameter is varied by alloying the vanadium with small quantities of gallium or niobium. Alloy compositions of V-0.20a/o Ga, V-1.05a/o Ga, V-2.96a/o Ga, and V-4.01a/o Nb are used. These yield a range of the Ginzburg-Landau parameter from less than 2 for the pure vanadium specimens, to more than

DD FORM 1 JAN 73 1473 EDITION OF 1 NOV 65 IS OBSOLETE

UNCLASSIFIED

SECURITY CLASSIFICATION OF THIS PAGE (When Data Entered)

20 for the V-2.96a/o Ga specimens.

The pinning force is not described by a universal scaling law for all specimens. The pinning force for a specific reduced magnetic field is determined by the depinning mechanism active at that field. There are at least three depinning mechanisms. Two of these can be identified with the plastic-deformation mechanism and the line-pinning mechanism, which are predicted by Kramer [1]. A previously unidentified depinning mechanism is the prevailing factor in specimens with large pinning centers.

The empirical line-pinning force of our specimens varies with the individual precipitate volume cubed times the density of precipitates. The pinning force in the plastic-deformation region varies as the cube-root of the density of precipitates. A dependence on the Ginzburg-Landau parameter squared can be observed for the magnitude of the pinning force for most of the reduced field regions.

ABSTRACT

The variation of the pinning force with microstructure and with the Ginzburg-Landau parameter is studied for 53 vanadium and vanadium alloy specimens. Vanadium-carbide precipitates are used as pinning centers. The Ginzburg-Landau parameter is varied by alloying the vanadium with small quantities of gallium or niobium. Alloy compositions of V-0.20a/o Ga, V-1.05a/o Ga, V-2.96a/o Ga, and V-4.01a/o Nb are used. These yield a range of the Ginzburg-Landau parameter from less than 2 for the pure vanadium specimens, to more than 20 for the V-2.96a/o Ga specimens.

The pinning force is not described by a universal scaling law for all specimens. The pinning force for a specific reduced magnetic field is determined by the depinning mechanism active at that field. There are at least three depinning mechanisms. Two of these can be identified with the plastic-deformation mechanism and the line-pinning mechanism, which are predicted by Kramer [1]. A previously unidentified depinning mechanism is the prevailing factor in specimens with large pinning centers.

The empirical line-pinning force of our specimens varies with the individual precipitate volume cubed times the density of precipitates. The pinning force in the plastic-deformation region varies as the cube-root of the density of precipitates. A dependence on the Ginzburg-Landau parameter squared can be observed for the magnitude of the pinning force for most of the reduced field regions.

TABLE OF CONTENTS

TABLE OF CONTENTS (Continued)

LIST OF TABLES

LIST OF FIGURES

LIST OF FIGURES (Continued)

LIST OF FIGURES (Continued)

LIST OF SYMBOLS

A	area
$\vec{A}$	magnetic vector potential
a_o	fluxoid lattice parameter
α,β	Ginzburg-Landau constants
$B,\vec{B}$	magnetic induction
C,C_a,C_p	scaling law parameters that are a function of microstructure, temperature, and the Ginzburg-Landau parameter
c	speed of light
c_L,c_{11},c_{44},c_{66}	elastic constants of the fluxoid lattice
D_1	scaling law parameter that is a function of κ_1
$d,d_{\|\|},d_\perp$	precipitate diameters
Δ	energy gap
E	energy
e	electronic charge
e^*	charge of the Cooper pair
E_s	elastic energy of the fluxoid lattice
$F(U)$	Labush's interaction tensor
f,f_m,f_s	Hemholtz free-energy densities
$f(h)$	form factor of the scaling law
f^*	effective interaction force
F_L	Lorentz force
F_p	pinning force density

LIST OF SYMBOLS (Continued)

f_p	interaction force
F_v	force per unit volume
G	Schmucker's Green function
g	perturbation of the reduced order parameter
γ	electronic specific heat
$H,\vec{H}$	magnetic field
h	reduced field
h	Planck's constant
H_c	thermodynamical critical field
H_{c_1}	lower critical field
H_{c_2}	upper critical field
H_{c_3}	surface-current critical field
$J,\vec{J}$	current density
$\vec{J}_c$	critical current density
$\vec{J}_s$	superconducting current density
K	kelvin
K_a,K_1,K_p,K_v	scaling law constants that are a function of the microstructure and the Ginzburg-Landau parameter
κ_B	Boltzmann's constant
κ,κ_o,κ_1	Ginzburg-Landau Parameters
κ_1	first Maki parameter, also referred to as a Ginzburg-Landau parameter
ℓ	mean free path
$\lambda,\lambda(T)$	penetration depth

LIST OF SYMBOLS (Continued)

λ_L	London's penetration depth
m^*	mass of the Cooper pair
N	density of electronic states
n	exponent of H_{c_2} in the temperature dependence of F_p, quantum number in flux quantization
η	constant of the $H_{c_2}(T)$ and the $K_1(T)$ temperature dependence
n_L	density of pinning centers per unit length of fluxoid
n_s^*	density of Cooper pairs
P	pressure
ϕ	phase of the order parameter
Φ	magnetic flux
Φ_o	fluxoid quantum
$\Psi, \Psi(r)$	order parameter
Ψ_o	unperturbed order parameter
ψ	reduced order parameter
Q	pinning force per pinning center
q	basic scaling law constants
r_1, r_2	resistance ratios
R_o	low temperature resistance
R_{295}	room temperature resistance
ρ	resistivity, density of precipitates
ρ_e	electronic resistivity

LIST OF SYMBOLS (Continued)

ρ_L	density of pinned fluxoids per cross-sectional area of the specimen
ρ_o	low temperature resistivity
ρ_{295}	room temperature resistivity
S	area of the Fermi surface
$s, \vec{s}$	path of integration
T	temperature
t	reduced temperature
	precipitate thickness
T_c	critical temperature
T_{c_o}	intrinsic critical temperature
τ, τ_{xy}	shear stress
τ_{max}	maximum shear stress
U	interaction potential
V	precipitate volume
v_F	Fermi velocity
v_c	fluxoid velocity
$\overline{V}, V_1, V_2, V_3$	precipitate volume which lies inside a fluxoid core
$\xi, \xi(T)$	coherence length
ξ_o	Pippard's coherence length

PREFACE

This research is based on the work of A.J. Marker on "Fluxoid Pinning by Vanadium Carbide Precipitates in Superconducting Vanadium" [2]. Our original goal was to expand on Marker's research by alloying vanadium in order to modify the superconducting properties of that metal. However, early in the project, there were signs of possible Joule heating at the current contacts to the specimens. It was suspected that the same problem might have troubled Marker. Therefore, the decision was made to incorporate pure vanadium in the present research. All efforts have been made to minimize the Joule heating and its effects. There is confidence that the present data reflects little, if any, Joule heating.

The author wishes to thank Professor R.W. Reed for suggesting this investigation and for his interest, assistance, and encouragement during its course.

Special thanks are due to Professor F. G. Brickwedde for his continuing advice and encouragement.

The author is deeply indebted to Professor W. R. Bitler and K. Moll for their participation in the preparation and characterization of the specimens used in this study.

Special thanks are due to A. J. Marker for his valuable assistance in the early stages of the project.

The support of the Applied Research Laboratory of The Pennsylvania State University under contract with the Naval Sea Systems Command is also acknowledged.

CHAPTER I

INTRODUCTION

Superconductors are materials which lose all electrical resistance at low temperatures. Although superconductivity was discovered in 1911 [3], successful technological applications have been developed only during the last twenty years. An example is the use of superconducting windings in high field magnets. These magnets play a prominent role in high-energy particle accelerators and in plasma containers for controlled fusion reactors. Superconducting computers, power lines, generators, and even the superconducting magnetic-levitation of trains are in advanced experimental stages. However, the understanding of the superconducting phenomena, mainly the ability to carry high densities of lossless currents, lags behind the technological success of superconductors.

A superconductor carries a lossless current only below a threshold defined by the temperature, the magnetic field, and the transport current density. The critical values of these three factors depend on the composition and microstructure of the material. The magnetic field penetrates a type of superconductor, called a Type II superconductor, in quantized bundles called fluxoids. The critical current of a Type II superconductor is dictated by the Lorentz force which causes the fluxoids to move. The movement of the fluxoids dissipates energy and thus terminates the lossless state. However, metallurgical defects in

the microstructure of the superconductor can create a "pinning force" which can prevent the movement of the fluxoids, thus maintaining the lossless state.

It has been suggested that the pinning force density, F_p, obeys a scaling law of the form [4]

$$F_p = K_p[H_{c_2}(T)]^n f(h) \quad , \tag{1.1}$$

where $H_{c_2}(T)$ is the upper critical field, f(h) is a form factor, and h is the reduced field H/H_{c_2}. The constant K_p depends on the microstructure of the superconductor and may depend on certain superconducting parameters of the material, e.g. the coherence length, ξ, and the Ginzburg-Landau parameter, κ.

The purpose of this investigation is to find the dependence of the scaling law on the specimen microstructure and on the Ginzburg-Landau parameter. Vanadium, which superconducts below 5.4K, is the basic material used in this study. Vanadium-carbide precipitates provide a controllable source of pinning centers. The Ginzburg-Landau parameter is varied by alloying the vanadium with small concentrations of gallium or niobium. The validity of the scaling law is also tested.

CHAPTER II

THEORY

The properties of a superconductor can roughly be divided in two categories, namely, the intrinsic or fundamental properties, which usually are reversible, and the mostly irreversible properties like flux pinning. The fundamental properties, like the critical temperature and critical fields, depend mostly on the thermodynamic and/or the electronic characteristics of the material. The irreversible properties, while also being dependent on the electronic and thermodynamic characteristics, depend heavily on the microstructure of the superconductor. The dependence of the irreversible properties on the thermodynamic and electronic parameters can be expressed in terms of the fundamental or reversible parameters. It is for this reason that the fundamental properties will be discussed first.

Gaussian (cgs) units are used through the text. In this system of units, and for the geometry of our experiment, the magnetic field, H, is numerically equal to the magnetic induction, B. Therefore, the magnetic field is used instead of the magnetic induction in many of our results.

This next section introduces basic concepts concerning superconductivity. It is not meant to be an exhaustive

treatise on the subject; several excellent books are available for this purpose [5,6,7]. The next section introduces and elaborates on the fluxoid concept. For more information on fluxoids, the reader is encouraged to read Huebener [8]. The last sections in this chapter deal with fluxoid pinning. Campbell [9] may be consulted for more information on the basic pinning interactions.

A) Fundamental Properties of Superconductors

The state of a superconductor depends on three external factors: the temperature, the magnetic field, and the transport current. In the absence of electrical current or magnetic fields, the normal-superconducting transition occurs at the critical temperature T_c. The critical temperature for pure metals and alloys vary from below 1K to near 24K. For pure vanadium, T_c equals 5.4K [10].

The effect of a magnetic field on a superconductor depends on the type of superconductor; there are two types. Type I superconductors exhibit nearly perfect diamagnetism up to a critical field H_c, where they become normal. This diamagnetic behavior is called the Meissner State after its discoverer [11]. The energy density needed to exclude the magnetic field from the bulk, given by $H_c^2(T)/8\pi$, can be equated to the difference in

Helmholtz free-energy densities, $f_n(T)$ and $f_s(T)$, of the normal and conducting state [12]. Hence, the critical field, H_c, can be defined thermodynamically as

$$\frac{H_c^2(T)}{8\pi} = f_n(T) - f_s(T) \quad . \tag{2.1}$$

The dependence of the critical field H_c on the temperature as seen in Figure 1 is given approximately by

$$H_c(T) \approx H_c(0)[1-t^2] \quad , \tag{2.2}$$

where t is the reduced temperature T/T_c.

The second kind of superconductors, called the Type II superconductors, show nearly perfect diamagnetism only up to a field H_{c_1}, which is below H_c (see Figure 2). Above H_{c_1}, in what is called the mixed state, magnetic flux starts to penetrate the material in quantized units of flux called fluxoids. At a field H_{c_2}, which is usually far above H_c, the bulk of the material becomes normal. Small lossless currents may still flow, in a thin surface layer, up to a field H_{c_3}, which is higher than H_{c_2}.

The diamagnetism of the Meissner State is perfect only in the bulk of the superconductor. The magnetic field is not abruptly excluded at the surface; it drops off exponentially, entering the bulk with a penetration depth λ. London's local theory of superconductivity [13] predicts a penetration depth given by

$$\lambda_L = \left(\frac{m^* c^2}{4\pi e^{*2} n_s^*} \right)^{1/2} \tag{2.3}$$

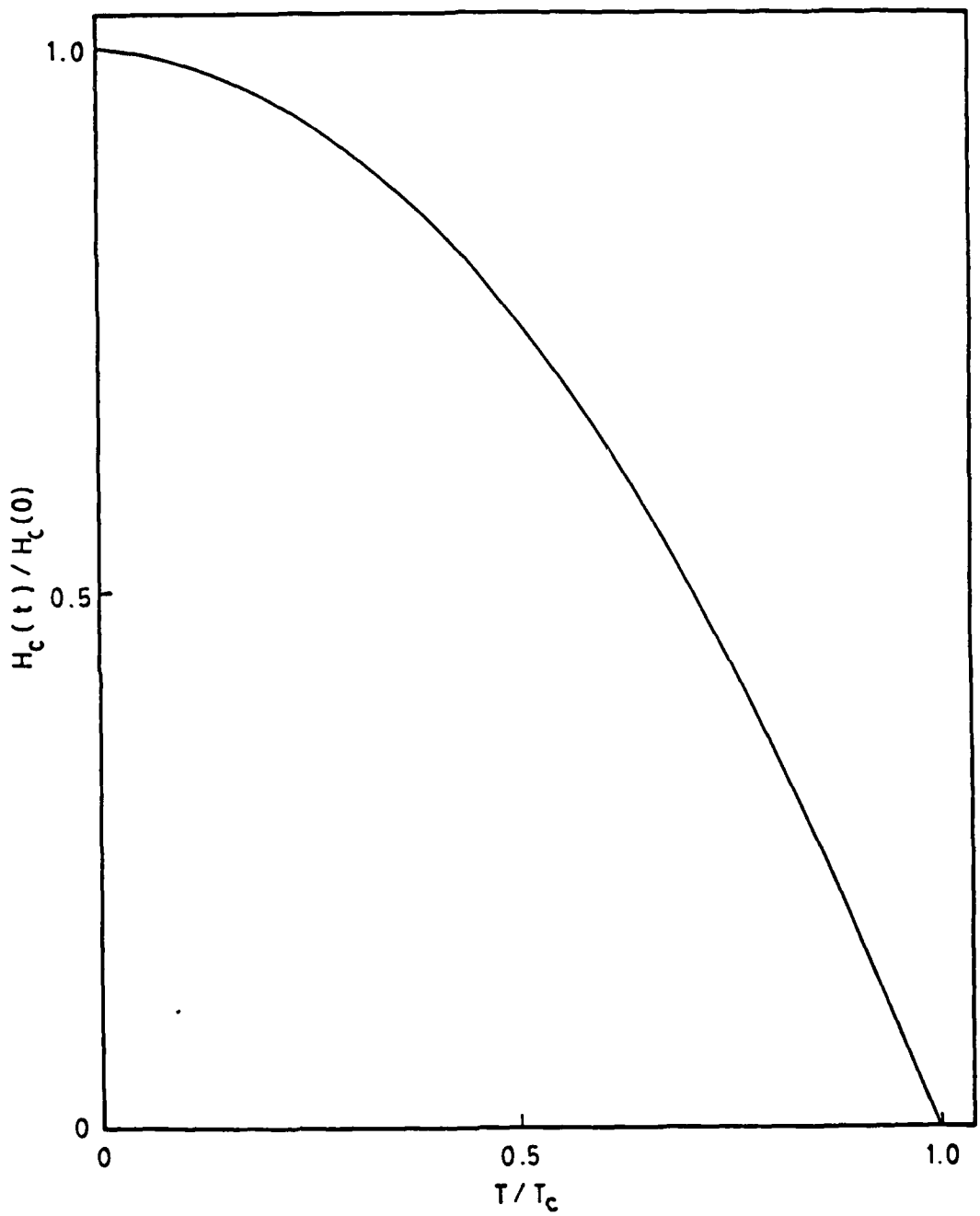

Figure 1) Variation of the critical field H_c with temperature.

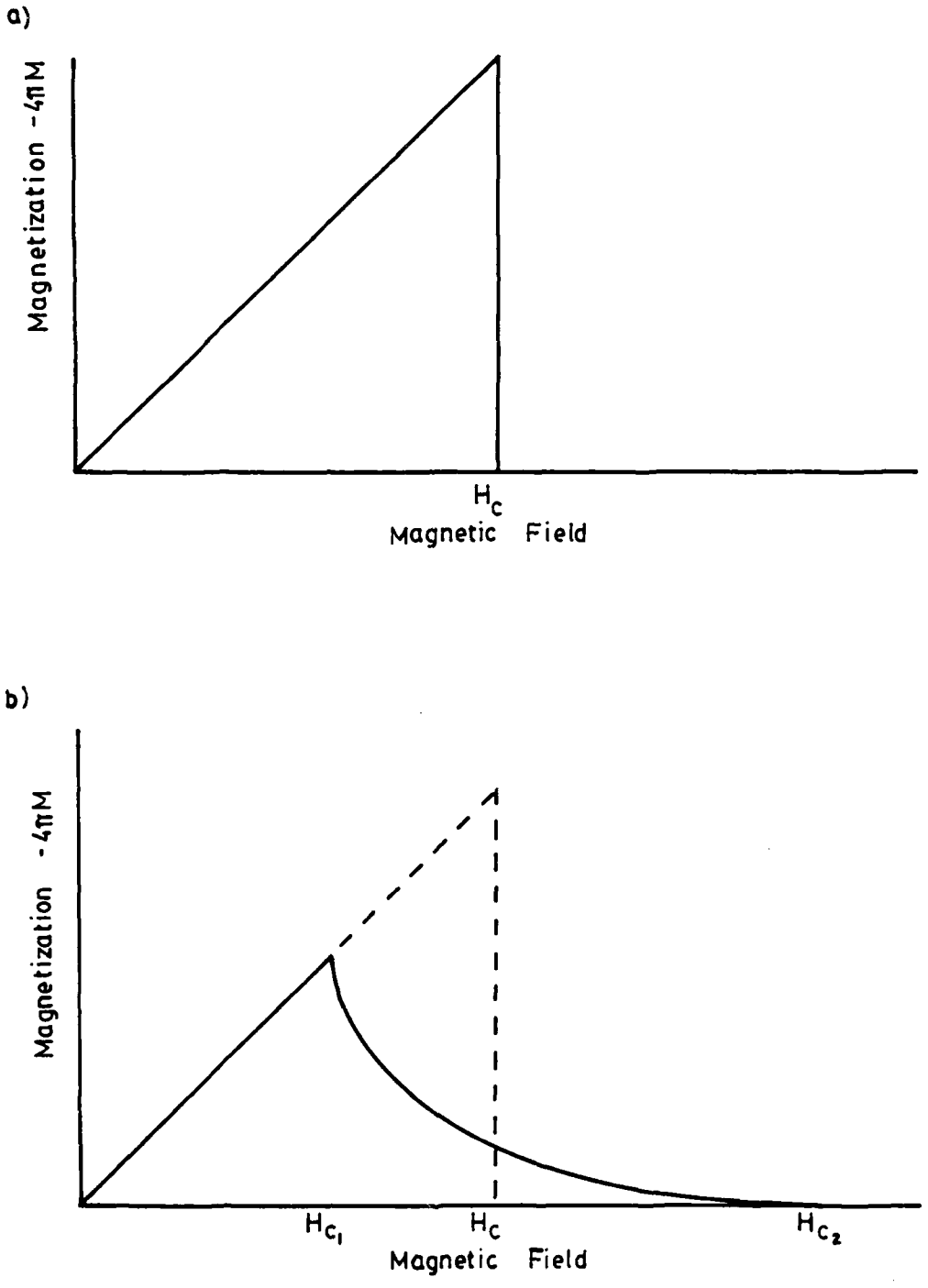

Figure 2) Magnetization as a function of magnetic field for a) a Type I superconductor, and b) a Type II superconductor.

where m^*, e^* and n_s^* are the effective mass, charge and density, respectively, of the superconducting charge carriers. The penetration depth at zero temperature is typically on the order of 10^{-6} cm.

Pippard [14] proposed a non-local theory of superconductivity in order to improve on London's local theory. Pippard's theory introduces another characteristic length, the coherence length ξ. The coherence length describes the range over which there are strong correlations between superconducting electrons. The coherence length of a pure metal is [15]

$$\xi_0 = \frac{a\hbar V_F}{k_B T_c} \quad , \tag{2.4}$$

where k_B is Boltzmann's constant, V_F is the Fermi velocity, and a is a constant which empirically equals 0.15 [15]. Pippard proposes that, in the presence of scattering, the coherence length should be

$$\frac{1}{\xi} = \frac{1}{\xi_0} + \frac{1}{\ell} \quad , \tag{2.5}$$

where ℓ is the electronic mean free path of the normal metal at the same temperature.

In 1957 Bardeen, Cooper and Schrieffer (BCS) published their successful microscopic theory of superconductivity [16]. This quantum-mechanical theory demonstrates that a weak attraction can bind, in pairs, electrons near the Fermi surface. The attraction that binds these "Cooper pairs" comes from an interaction of the

electrons with the lattice phonons. This interaction extends through a distance given by the coherence length ξ. The coherence length of the pure metal given by the BCS theory is

$$\xi_o = \frac{\hbar V_F}{\pi \Delta} = \frac{0.18 \hbar V_F}{k_B T_c} \quad , \tag{2.6}$$

where Δ is the energy gap of the superconductor. Cooper pairs have an effective mass m^* and a charge e^*, equal to twice the mass and charge, respectively, of the free electron.

In 1950 Ginzburg and Landau [17] proposed a phenomenological theory of superconductivity based on Landau's theory of second-order phase transitions. Landau's theory [18] states:

i) that the state of the material can be characterized by an order parameter, Ψ, which describes the "degree of ordering" associated with the increase in symmetry of the system as it goes through a second-order transition. The order parameter is zero at the transition point.

ii) that the free energy can be expanded in powers of the order parameter.

iii) that the coefficients of expansion are functions of the temperature.

Thus, the Helmholtz free-energy density can be written as

$$f' = f + \alpha(T)|\Psi|^2 + \frac{\beta(T)}{2}|\Psi|^4 + \ldots \tag{2.7}$$

Ginzburg and Landau apply this concept to the superconducting transition in a quantum-mechanical way. They treat the order parameter $\Psi(r)$ as a pseudowavefunction which describes the center-of-mass motion of the Cooper pairs, with $|\Psi|^2$ being the local density of superconducting Cooper pairs, n_s^*. They include a term for the magnetic energy and a term for momentum, obtaining

$$f_s = f_n + \alpha|\Psi|^2 + \frac{\beta}{2}|\Psi|^4 + \frac{1}{2m^*}\left|\left(\frac{\hbar\vec{\nabla}}{i} - \frac{e^*\vec{A}}{c}\right)\Psi\right|^2 + \frac{H^2}{8\pi} \quad . \tag{2.8}$$

Again, m^* and e^* are the effective mass and charge of the Cooper pairs, that is, twice the mass and charge of the electron.

The free energy can be minimized with respect to spatial variations of $\Psi(r)$ and with respect to $A(r)$. This procedure yields the two Ginzburg-Landau differential equations

$$0 = \alpha\Psi + \beta|\Psi|^2\Psi + \frac{1}{2m^*}\left(\frac{\hbar\vec{\nabla}}{i} - \frac{e^*\vec{A}}{c}\right)^2\Psi \quad . \tag{2.9}$$

and

$$\vec{J}_s = \frac{e^*\hbar}{2m^*i}\left(\Psi^*\vec{\nabla}\Psi - \Psi\vec{\nabla}\Psi^*\right) - \frac{e^{*2}}{m^*c}\Psi^*\Psi\vec{A} \quad . \tag{2.10}$$

In the absence of gradients or fields, equation (2.9) yields

$$|\Psi|^2 = \frac{-\alpha}{\beta} = n_s^* \quad . \tag{2.11}$$

This result can be used on equation (2.8) under the above condition yielding

$$f_n - f_s = \frac{\alpha^2}{2\beta} \quad , \tag{2.12}$$

which, using equation (2.1) becomes

$$\frac{\alpha^2}{\beta} = \frac{H_c^2}{4\pi} \quad . \tag{2.13}$$

One can solve simultaneously equations (2.11) and (2.13) obtaining

$$\alpha = \frac{- H_c^2}{4\pi n_s^*} \tag{2.14}$$

and

$$\beta = \frac{H_c^2}{4\pi n_s^{*2}} \quad . \tag{2.15}$$

London's penetration depth, λ_L, can be obtained from equation (2.10). For weak magnetic fields, $|\Psi|^2$ can be replaced by its equilibrium value $|\Psi_o|^2$, so that

$$\vec{J}_s = \frac{e^* \hbar}{2m^* i} (\Psi^* \vec{\nabla} \Psi - \Psi \vec{\nabla} \Psi^*) - \frac{e^{*2}}{m^* c} |\Psi_o|^2 \vec{A} \quad . \tag{2.16}$$

One can take the curl on both sides of this equation, obtaining

$$\text{curl } \vec{J}_s = \frac{-e^{*2}}{m^* c} |\Psi_o|^2 \vec{H} \quad . \tag{2.17}$$

The Maxwell equation

$$\text{curl } \vec{H} = \frac{4\pi}{c} \vec{J} \quad , \tag{2.18}$$

can be used to express equation (2.17) as

$$\frac{c}{4\pi} \text{ curl curl } \vec{H} = \frac{-e^{*2}}{m^* c} |\Psi_o|^2 \vec{H} \quad , \tag{2.19}$$

and one obtains

$$\frac{m^* c^2}{4\pi e^{*2} |\Psi_0|^2} \nabla^2 \vec{H} = \vec{H} \quad . \tag{2.20}$$

This equation yields a magnetic field penetration that agrees with London's (Equation 2.3).

The Ginzburg-Landau theory provides a temperature dependent coherence length. If $\psi^2 = |\Psi|^2/|\Psi_0|^2 = |\Psi|^2(-\beta/\alpha)$ is substituted into equation (2.9) in the absence of magnetic field, one obtains

$$0 = \psi - \psi^3 = \frac{\hbar^2}{2m^*|\alpha|} \frac{d^2\psi}{dx^2} \quad . \tag{2.21}$$

One can substitute $\psi(x) = 1 + g(x)$, where $g(x) \ll 1$, yielding

$$0 = -2g - 3g^2 - g^3 + \frac{\hbar^2}{2m^*|\alpha|} \frac{d^2g}{dx^2} \quad . \tag{2.22}$$

This equation can be approximated, to the first order of g, by

$$4 \frac{m^*|\alpha|}{\hbar^2} g(x) = \frac{d^2g(x)}{dx^2} \quad . \tag{2.23}$$

The function g(x) will decay to 1/2g(0) at a characteristic length

$$\xi(T) = \frac{\hbar}{(2m^*|\alpha(T)|)^{1/2}} \quad , \tag{2.24}$$

called the temperature dependent coherence length. Equations (2.3) and (2.14) can be used to express α as

$$\alpha(T) = \frac{-4e^2}{m^* c^2} H_c^2(T)\lambda^2(T) \quad , \tag{2.25}$$

Now the coherence length can be expressed as

$$\xi(T) = \frac{\hbar c}{2\sqrt{2}\, e H_c(T) \lambda_{eff}(T)} \quad . \tag{2.26}$$

The coherence length $\xi(T)$ denotes the characteristic decay-length for small variations of the order parameter . It is not the same as Pippard's coherence length ξ, (Equation 2.5) which denotes the smallest possible size of the superconducting electron wave-packets. However, Gor'kov [19] shows that there is a relation between the GL coherence length $\xi(T)$ and Pippard's coherence length for pure metals, ξ_o (Equation 2.4).

Gor'kov [19] demonstrates that the GL theory is a limiting case, near T_c, of the BCS theory. The BCS theory can then be used to approximate the GL critical lengths near T_c for two limits: the pure limit, where the electronic mean free path, ℓ, is much larger than the penetration depth λ_L, and the dirty limit, where $\ell \ll \lambda_L$. For these limits, the critical lengths are given by [5,19].

$$\xi(T) = 0.74 \frac{\xi_o}{(1-t)^{1/2}} \tag{2.27}$$

pure limit

$$\lambda(T) = \frac{\lambda_L(o)}{[2(1-t)]^{1/2}} \tag{2.28}$$

and

$$\xi(T) = 0.855\ \frac{(\xi_{o}\ell)^{1/2}}{(1-t)^{1/2}} \qquad \text{dirty limit} \tag{2.29}$$

$$\lambda(T) = \lambda_{L}(o)\left[\frac{\xi_{o}}{2.66\ell(1-t)}\right]^{1/2} \tag{2.30}$$

where $\lambda_{L}(o)$ is London's penetration depth at zero temperature, and t is the reduced temperature, T/T_{c}.

Both the penetration depth (Equations 2.28 and 2.30) and the GL coherence length (Equations 2.27 and 2.29), have the same temperature dependence near T_{c}. A GL parameter, κ, can then be defined by

$$\kappa(T) = \frac{\lambda(T)}{\xi(T)} \ , \tag{2.31}$$

which near T_{c} becomes temperature independent and equal to

$$\kappa_{o} = 0.96\ \frac{\lambda_{L}(o)}{\xi_{o}} \qquad \text{for pure metals} \tag{2.32}$$

and

$$\kappa_{\ell} = 0.715\ \frac{\lambda_{L}(o)}{\ell} \qquad \text{for dirty metals.} \tag{2.33}$$

Goodman [20] shows that for intermediate values of ℓ, κ can be approximated by

$$\kappa = \kappa_{o} + \kappa_{\ell} \ . \tag{2.34}$$

The GL parameter, κ, plays an important role in determining if a superconductor is Type I or Type II. There is a negative energy

associated with the expulsion of the magnetic field from the bulk of the material. On the other hand, there is a positive energy which is the result of forming normal/superconducting interfaces. Their sum is called the surface energy. For κ less than $1/\sqrt{2}$, the surface energy is positive. This inhibits the formation of normal/superconducting surfaces within the bulk, creating the Meissner effect. Abrikosov [21] finds that for κ greater than $1/\sqrt{2}$, the surface energy is negative, so that normal-superconducting interfaces are encouraged. This induces the magnetic field to penetrate in the form of fluxoids. The GL parameter can then be used to define the type of superconductor:

$$\kappa < 1/\sqrt{2} \equiv \text{Type I superconductor,}$$

and

$$\kappa > 1/\sqrt{2} \equiv \text{Type II superconductor .}$$

There is a unitless parameter, $\kappa_1(T)$, which relates the upper critical field H_{c_2} to the thermodynamic critical magnetic field H_c by

$$H_{c_2}(t) = \sqrt{2}\,\kappa_1(t) H_c(t) \quad . \tag{2.35}$$

At the critical temperature, $\kappa_1(T_c)$ equals κ. Marker [2] finds that the temperature dependence of $\kappa_1(t)$ can be approximated by

$$\kappa_1(t) \approx \frac{\kappa(1+\eta)}{(1+\eta t^2)} \quad , \tag{2.36}$$

where η is a parameter on the order of unity.

B) Fluxoids

Magnetic flux, as noted previously, penetrates a superconductor for fields above $H_{c_2}(T)$. It penetrates in quantized bundles called fluxoids [22]. The fluxoids are a direct result of the second GL differential equation

$$\vec{J} = \frac{e^* \hbar}{2m^* i} (\psi^* \vec{\nabla} \psi - \psi \vec{\nabla} \psi^*) \frac{-e^{*2}}{m^* c} \psi^* \psi \vec{A} \quad . \tag{2.37}$$

The order parameter can be separated into a magnitude $|\psi|$ and a phase ϕ obtaining

$$\vec{J} = \frac{e^* \hbar}{m^*} |\psi|^2 \vec{\nabla} \phi - \frac{e^{*2}}{m^* c} |\psi|^2 \vec{A} \quad . \tag{2.38}$$

One can substitute n_s^* for $|\psi|^2$ and rearrange this equation obtaining

$$\frac{c\hbar}{e^*} \vec{\nabla} \phi = \frac{m^* c}{e^{*2} n_s^*} \vec{J} - \vec{A} \quad . \tag{2.39}$$

An integration over a closed path s inside the superconducting material yields

$$\frac{c\hbar}{e^*} \oint \vec{\nabla} \phi \cdot d\vec{s} = \frac{m^* c}{e^* n_s^*} \oint \vec{J} \cdot d\vec{s} - \oint \vec{A} \cdot d\vec{s} \tag{2.40}$$

$$= \frac{m^* c}{e^* n_s^*} \oint \vec{J} \cdot d\vec{s} - \Phi \quad . \tag{2.41}$$

The order parameter must be a single valued function, so for a loop around the path s, the phase ϕ must vary by $2\pi n$. When this fact is applied to the integral on the left one obtains the fluxoid quantization

$$\frac{nch}{e^*} = \frac{m^* c}{e^* n_s} \oint \vec{J} \cdot d\vec{s} - \Phi \quad . \tag{2.42}$$

This equation describes a magnetic entity, the fluxoid, which is composed of a superconducting current vortex surrounding a magnetic flux column (see Figure 3a). The number of superconducting electrons decreases toward the center of the vortex, creating a normal core of radius $\xi(T)$ (see Figure 3b). The magnetic flux quantum, Φ_o, is given by

$$\Phi_o = \frac{hc}{e^*} = \frac{hc}{2e} = 2.07 \times 10^{-7} \text{ gauss-cm}^2 \quad . \tag{2.43}$$

This relation can be used together with Equations (2.26) and (2.31) to express the coherence length as

$$\xi(T) \approx \left[\frac{\Phi_o}{2\pi H_{c_2}(T)} \right]^{1/2} \quad . \tag{2.44}$$

A fluxoid is repelled by the magnetic field of neighboring fluxoids. This mutual repulsion induces them to form in a periodic lattice array which is usually triangular. The geometry of the crystal lattice can deform the fluxoid lattice angles, and can even

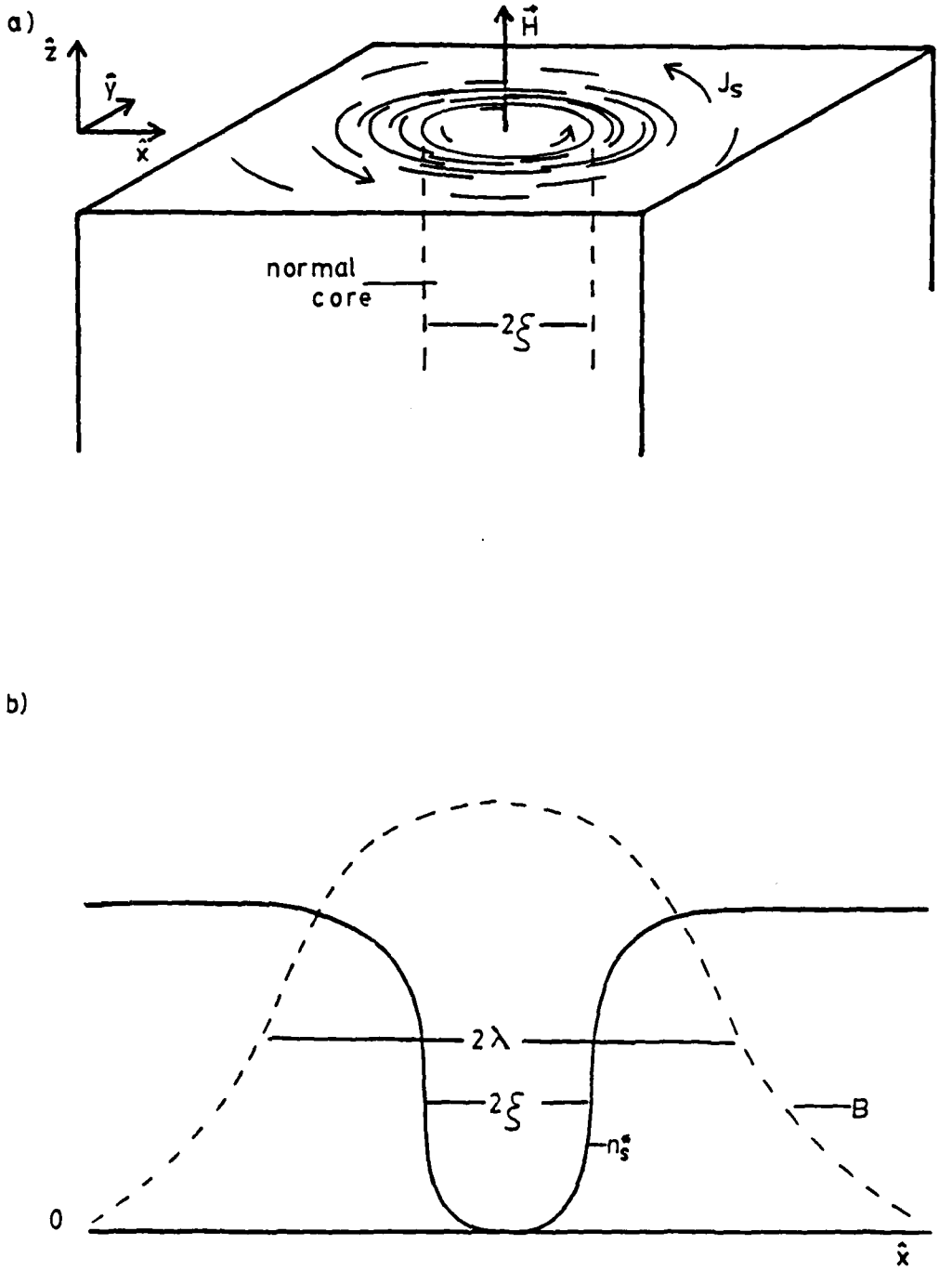

Figure 3) Schematic representation of a fluxoid showing a) the supercurrent distribution around the normal core, and b) the density of superconducting electrons and the magnitude of the magnetic induction.

dictate a square fluxoid lattice [8]. The distance between fluxoids in a triangular lattice is given by the fluxoid lattice parameter a_o

$$a_o = \left(\frac{2\Phi_o}{\sqrt{3}B} \right)^{1/2} . \qquad (2.45)$$

The Flux Line Lattice (FLL) responds elastically to applied forces. Any elastic reaction of the lattice can be described by a combination of the following elastic moduli given by Labush [23]:

c_L - which changes the cross-sectional area of a fluxoid lattice cell but not its shape,

c_{44} - which tilts the fluxoids away from the z-direction, and

c_{66} - which shears the lattice in the x-y plane (see Figure 4).

The elastic moduli for magnetic fields near H_{c_2} are given by [23]:

$$c_L = \frac{B^2}{4\pi} \frac{\partial H}{\partial B} \qquad (2.46)$$

$$c_{44} = \frac{BH}{4\pi} \qquad (2.47)$$

$$c_{66} = \frac{.48(1-h)^2 H_{c_2}^2}{8\pi(2\kappa^2-1)\beta_T^2} \qquad (2.48)$$

where h is the reduced field H/H_{c_2}, and, for a triangular lattice, β_T is equal to 1.16. Although these results are strictly correct only in fields near H_{c_2}, they are routinely used, with good results, at lower fields.

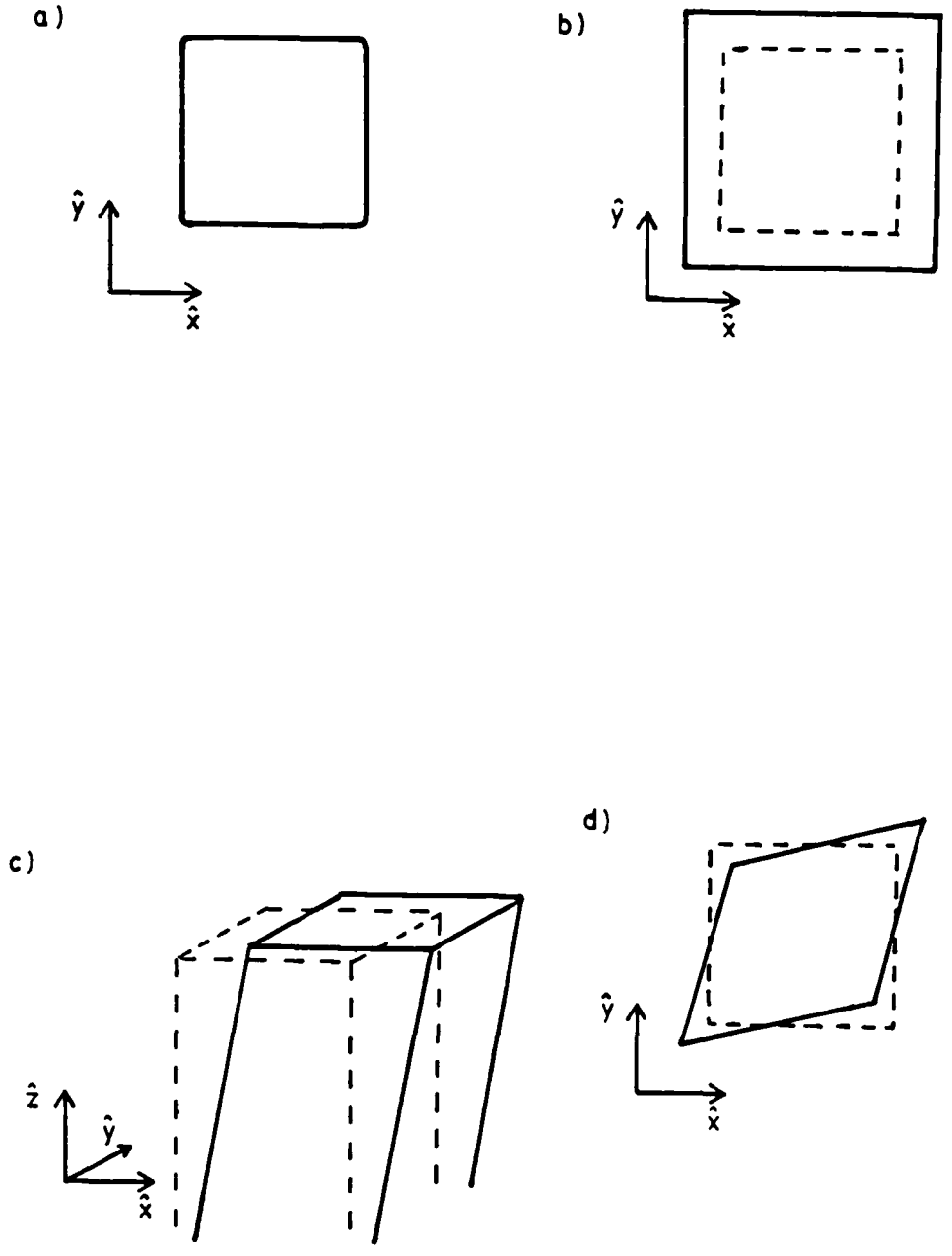

Figure 4) Schematic model of the elastic moduli showing a) a cross-sectional area of the FLL at rest, b) c_L, c) c_{44}, and d) c_{66}.

C) Flux Pinning

1) The Lorentz Force and the Critical Current

An electrical current density, J, passing through a superconductor which is in a magnetic field, creates a Lorentz force density,

$$\vec{F}_L = \frac{1}{c} \vec{J} \times \vec{B} \quad , \tag{2.49}$$

that acts on the fluxoids (see Figure 5). This force can be derived thermodynamically from the Helmholtz free energy density f [9]. An area A, perpendicular to a magnetic induction B, can be compressed in such a way that $B\delta A + A\delta B = 0$. The pressure, in terms of the free energy density is

$$P = - \left(\frac{\partial \text{Force}}{\partial A} \right)_T = - \frac{\partial (Af)}{\partial A} = -f - \frac{A \partial f}{\partial A} \quad . \tag{2.50}$$

Due to our initial conditions, this can be expressed as

$$P = -f + \frac{B \partial f}{\partial B} \quad . \tag{2.51}$$

The force per unit volume, F_v, is

$$F_v = \frac{dP}{dy} = - \frac{df}{dy} + \frac{d}{dy} \left(\frac{B df}{dB} \right)$$

$$= - \frac{df}{dB} \frac{dB}{dy} + \frac{dB}{dy} \frac{df}{dB} + B \frac{d}{dy} \left(\frac{df}{dB} \right) \tag{2.52}$$

Campbell and Evetts [9] assume that the condition for thermal equilibrium is

$$\frac{\partial f}{\partial B} = \frac{H}{4\pi} \quad , \tag{2.53}$$

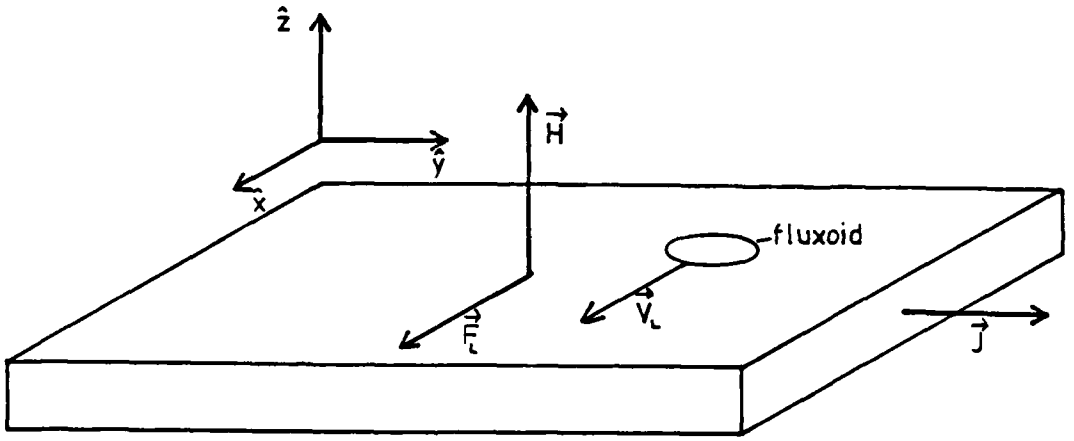

Figure 5) Schematic representation of the Lorentz force $\vec{F}_L = \frac{1}{c} \vec{J}_c \times \vec{H}$, and of a fluxoid moving with velocity $\vec{V}_L$.

therefore,

$$F_v = \frac{B}{4\Pi} \frac{dH}{dy} \quad . \tag{2.54}$$

The Maxwell relation $\vec{\nabla} \times \vec{H} = \frac{4\Pi}{c} \vec{J}$ can be used to obtain

$$\vec{F}_v = \frac{1}{c} \vec{J} \times \vec{B} = \vec{F}_L \tag{2.55}$$

When the Lorentz force causes the fluxoids to move, they create an electrical field [24] due to the Maxwell relation

$$\nabla \times \vec{E} = - \frac{1}{c} \frac{\partial \vec{B}}{\partial t} \quad . \tag{2.56}$$

In the case where the fluxoid velocity V_L is a constant, the above expression yields [25]

$$\vec{E} = \frac{1}{c} \vec{V}_L \times \vec{B} \quad . \tag{2.57}$$

where $\vec{E}$ is parallel and opposite to the current. Such is the case for a superconductor without microstructural defects, where the flux flow is limited by viscous forces. Work is done against the viscous forces when the fluxoids are moved. Therefore, although the material remains in the superconducting state, it no longer carries a lossless current. The current at which the fluxoid-induced voltage is first observed is defined as the critical current.

The critical current can be increased by preventing the movement of the fluxoids. A force equal and opposite to the Lorentz Force must be provided to "pin" the fluxoids. Anderson [26] proposed that this "pinning" could be accomplished by inhomogeneities in the material. Fluxoids can be attracted or repelled by impurities and

crystal lattice defects, effectively being pinned by them. The maximum "pinning force" density exerted by these defects, F_p, can be calculated from the Lorentz Force at the critical current J_c

$$\vec{F}_p = - \vec{F}_L(J_c) = - \frac{1}{c} \vec{J}_c \times \vec{B} \quad . \tag{2.58}$$

Power is still dissipated at currents above J_c. However, now V_L is not a constant; it depends on the depinning mechanism. The dissipated power can be calculated from the work done to depin the fluxoids from the pinning centers.

2) Pinning-Producing Material Defects

Material defects interact in a variety of ways with the fluxoid lattice. Crystal lattice dislocations and grain boundaries produce in their vicinity changes in the superconducting parameters. The coherence length, the critical field, and other parameters are affected by the electron scattering caused by the crystal defects. The change in these parameters, in turn, changes the local value of the fluxoid lattice energy. This energy gradient can attract the fluxoids to the defect or repel them away, acting, in both cases, as a barrier to the movement of the fluxoids.

The elastic energy of the crystal lattice dislocations can also produce pinning [27]. The vortex core is stiffer than the surrounding superconducting material. Therefore, the elastic energy of a crystal lattice dislocation increases as a fluxoid core approaches it, creating a repulsive force. Furthermore, the specific volume of the core is lower than that of the surrounding bulk, creating local stresses. These stresses interact with the strains created by the crystal defects.

Defects that are large compared with the penetration depth, λ, produce pinning due to "magnetic interactions." The magnetic field inside these defects can differ from the average magnetic field in the bulk. The fluxoid lattice is pinned by the resulting gradient in magnetic energy.

A void or a normal impurity with a small size compared to the penetration depth, λ, can pin a fluxoid due to the change in condensation energy if the fluxoid threads the impurity. Normal electrons must be created if the fluxoid core moves out of the impurity. Cooper pairs in the surrounding bulk must be broken up to provide these normal electrons. Energy is spent in breaking the pairs, therefore, the fluxoids prefer to stay pinned to the impurities. This interaction between the fluxoid core and an impurity is called a "core interaction."

3) Core Interactions

Many of the specimens in this research have a high density of small precipitates ($d<\lambda$). If this density is higher than the density of other types of crystalline defects, the biggest contribution to the pinning force density is due to "core interactions" between the vanadium-carbide precipitates and the fluxoids. Due to the small size of the precipitates of these specimens, the "magnetic interactions" are negligible. The density of non-precipitate defects in the specimens used is low, therefore, the pinning force density due to these defects is neglected.

The core interaction force, f_p, is usually obtained from the Ginzburg-Landau free energy density. We can obtain the interaction force following the method used by Campbell and Evetts [9]. Consider moving a normal precipitate of diameter $<2\xi$ and volume V from inside a fluxoid core to a position half way between two fluxoids, $x = \ell/2a_o$. According to Campbell and Evetts, the change in the G.L. free energy ΔE, can be expressed as

$$\Delta E = \frac{VH_c^2}{4\pi} \xi^2 \nabla^2 \psi^2 |_{max}, \tag{2.59}$$

where, again, $\psi^2 = |\Psi|^2/|\Psi_o|^2$. Saint-James, et al. [7] obtain an expression for ψ^2. Campbell and Evetts simplify this expression obtaining for materials with high κ, the relation

$$\psi^2 \approx (1-h)\left(1 - \left[\frac{1}{3}\cos\left(x - \frac{y}{\sqrt{3}}\right)\frac{2\pi}{a_o} + \cos\frac{2y}{\sqrt{3}}\frac{2\pi}{a_o} + \cos\left(x + \frac{y}{\sqrt{3}}\right)\frac{2\pi}{a_o}\right]\right), \tag{2.60}$$

where x and y are the distances from the core of a fluxoid. It is more illustrative to consider a one-dimensional approximation of the square lattice at high fields, given by

$$\psi^2(x) \approx \frac{1}{2}(1-h)\left(1 - \cos\frac{2\pi x}{a_o}\right) \quad . \tag{2.61}$$

Using this approximation, the change in free energy becomes

$$\Delta E = \frac{VH_c^2}{4\pi}\left(\frac{2\pi\xi}{a_o}\right)^2 \psi^2 |_{max} \quad . \tag{2.62}$$

The interaction force, f_p, is then equal to

$$f_p = \frac{\partial E}{\partial x} = \frac{V}{4\Pi}\left(\frac{2\Pi}{a_o}\right)^3 \xi^2 H_c^2 \psi^2|_{max} \quad . \tag{2.63}$$

The maximum value of ψ^2 is (1-h), therefore,

$$f_p = \frac{V}{4\Pi}\left(\frac{2\Pi}{a_o}\right)^3 \xi^2 H_c^2 (1-h) \quad . \tag{2.64}$$

This result is the same as that obtained by Campbell and Evetts [9]. Using Equations (2.35), (2.44), and (2.45) one obtains from Equation (2.64)

$$f_p = c_p \frac{V H_{c_2}^{5/2} h^{3/2}}{\kappa_1^2 \Phi_o^{1/2}} (1-h) \tag{2.65}$$

where $c_p = 1.27$.

Kramer [28], and Fähnle [29] also obtain an interaction force from the G.L. free energy density. They use approaches which are more sophisticated than the one discussed above. Their results are of the same form as Equation (2.65), with c_p equal to 0.866 and 0.274 in their respective calculations.

Kramer's result [28], given by

$$f_p = \frac{0.866\ V H_{c_2}^{5/2} h^{3/2} (1-h)}{\kappa_1^2 \Phi_o^{1/2}} \tag{2.66}$$

will be used in future calculations. We will use it because of the frequent use of this result in the literature, and because its value of c_p falls near the middle of those found by Campbell and Evetts (c_p = 1.27) [9] and Fähnle (c_p = 0.274) [29].

For precipitates with one or more dimensions larger than twice the coherence length, part of the precipitate volume lies outside of the normal core of a fluxoid that threads it. Therefore, the change in the G.L. free energy, given by Equation (2.59), is not proportional to V. This energy change is now proportional to that part of the precipitate volume that lies inside the normal core.

The precipitates in our research are thin disks, the planes of which are usually oriented at 90°, 71.6° and 18.4° to the specimen surface [30]. In the geometry of our experimental set-up, these precipitates lie at 0°, 18.4° and 71.6° to the magnetic field. For precipitates with diameter, d, larger than twice the coherence length, the precipitate volume within a fluxoid normal core, shown in Figure 6, can be approximated by

i) for the 0° orientation

$$V_1 \approx 2t\xi(T)\left[\frac{d}{2}^2 - \xi^2(T)\right]^{1/2} + t\frac{d^2}{2}\arctan\left[\frac{2\xi(T)}{d}\right] , \tag{2.67}$$

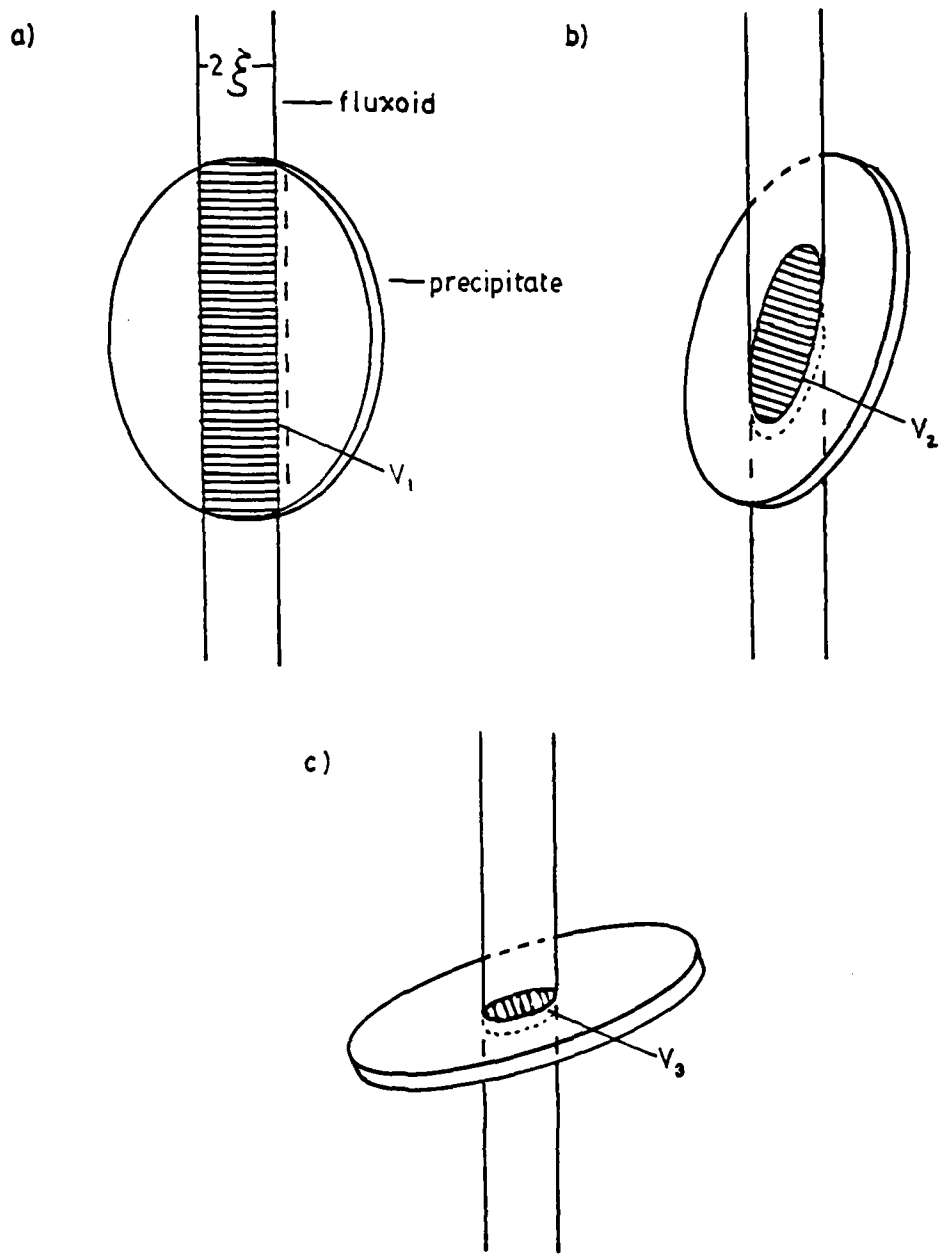

Figure 6) Schematic representation of a fluxoid threading a disk-shaped precipitate at an angle, between the fluxoid axis and precipitate plane, of a) 0°, b) 18.4°, and c) 71.6°.

ii) for the 18.4° orientation, and $\xi(T)<\frac{d}{6}$

$$V_2 \approx 4t^2\xi^2(T) \sec (18.4°) \quad , \tag{2.68}$$

and, for $\frac{d}{2}>\xi(T)>\frac{d}{6}$,

$$V_2 \approx V_1 \quad , \tag{2.69}$$

iii) for the 71.4° orientation

$$V_3 \approx \Pi\, \xi^2 t \sec (71.4°) \quad , \tag{2.70}$$

where t is the precipitate thickness. The average volume, $\overline{V}$, is given by

$$\overline{V} = \frac{1}{3} (V_1 + V_2 + V_3) \quad . \tag{2.71}$$

For $\frac{d}{2}>\xi(T)$, this equation can be approximated by

$$\overline{V} \approx \frac{1}{3} V_1 \approx \frac{2}{3} \xi t d \quad . \tag{2.72}$$

A normal metal in good electrical contact with a superconductor will acquire superconducting properties near the contact area [31]. The Cooper pairs in the superconductor penetrate a distance ξ into the normal metal, creating a superconducting layer of thickness ξ. The thickness, t, of most of the precipitates is less than ξ. Therefore, the precipitates might become superconductors with H_c lower than that of the bulk. This can reduce the change in free energy used to calculate f_p, Equation (2.59), by a factor [28]

$$\frac{\delta H_c}{H_c} = \frac{H_{c_{bulk}} - H_{c_{ppt}}}{H_{c_{ppt}}} \quad , \tag{2.73}$$

where $H_{c_{ppt}}$ is the local value of the critical field inside the precipitate. Kramer [28] calculates the change in f_p due to the proximity effect on precipitates like ours and obtains a resulting interaction force f_p' equal to

$$f_p' = \frac{2^7}{\Pi} N(o) \left(\frac{\Delta k_1 t \lambda_o}{H_{c_2} \xi_o \lambda} \right)^2 f_p \quad , \tag{2.74}$$

where f_p is given by Equation (2.66), $N(o)$ is the density of states at the Fermi surface, Δ is the superconducting energy gap, t is the precipitate thickness, and $\lambda_o = \lambda(T = 0)$. This factor adds to f_p a further dependence on the microstructure, given by t^2, and a further dependence on temperature, which is approximately given by (1-t). For our specimens, the thickness t is proportional to the square root of the precipitate diameter, d. Therefore, when the proximity effect is considered, the resulting interaction force, f_p', is proportional to

$$f_p' \propto d(1-t)\, f_p \quad . \tag{2.75}$$

4) Summation of the Macroscopic Pinning Force

The summation of the elementary pinning force, f_p, exerted by the pinning centers, into a macroscopic pinning force density, F_p, is a major problem. First, several of the potential sources of pinning mentioned in the previous sections can act at the same time. Second, the strong coupling between the flux lines in the fluxoid lattice prevents a simple summation of forces; stresses

induced on the fluxoid lattice by a pinning center may reach neighboring pinning centers. Furthermore, the fluxoid lattice is not rigid, it bends and plastically deforms to minimize its energy.

a) Dew-Hughes' Theory

Dew-Hughes [32] ignores the elastic behavior of the lattice. He assumes a direct summation of the elementary interaction forces,

$$F_p = \Sigma f_p \qquad \text{over all pinning centers in a unit volume,} \tag{2.76}$$

so that

$$F_p = \rho \bar{f}_p \quad , \tag{2.77}$$

where ρ is the density of pinning centers. This is the maximum F_p that could conceivably be calculated. Using Equation (2.66) one obtains

$$F_p = 0.866 \frac{\rho V H_{c_2}^{5/2} h^{3/2} (1-h)}{\kappa_1^2 \Phi_o^{1/2}} \quad . \tag{2.78}$$

b) Labush's Theory

Labush [33] computes F_p using a statistical method to take into account the interaction between fluxoids. He obtains for small plate-like precipitates

$$F_{p_i} = \frac{\rho d f_p^2}{8\sqrt{\Pi}} \left(\frac{B}{\Phi_o}\right)^{1/2} \left[\frac{1}{\sqrt{c_{11}c_{44}}} \left(-\sqrt{1 + \frac{\alpha_i}{4\Pi c_{11}}} - \sqrt{\frac{\alpha_i}{4\Pi c_{11}}} \right) - \frac{1}{\sqrt{c_{66}c_{44}}} \left(-\sqrt{1 + \frac{\alpha_i}{4\Pi c_{66}}} - \sqrt{\frac{\alpha_i}{4\Pi c_{66}}} \right) \right], \tag{2.79}$$

where i stands for the coordinates x and y, the parameter c_{11} equals $(c_L + c_{66})$, and d is the diameter of the precipitates. The tensor α is the mean value of F(U) over all line elements of the fluxoid lattice. The tensor F(U) is given by

$$F(U) = \frac{\partial^2 U}{\partial x^2}\ \hat{x} + \frac{\partial^2 U}{\partial y^2}\ \hat{y} \quad , \tag{2.80}$$

where U is the potential of the interaction between a fluxoid and a pinning center, given in energy per unit length. Weak interactions, or high reduced magnetic field, yield $(\alpha/4\pi c_{66})<<1$. In this case, the elastic response of the lattice is independent of α and Equation (2.78) becomes

$$F_p \simeq \frac{\rho d f_p^2}{8\sqrt{\pi}} \left(\frac{B}{\Phi_o}\right)^{1/2} \left(\frac{1}{\sqrt{c_{11}c_{44}}} + \frac{1}{\sqrt{c_{66}c_{44}}} \right) . \tag{2.81}$$

Assuming that $H \approx B$, the use of Equations (2.46), (2.47), (2.48), and (2.66) yields

$$F_p \simeq 0.38 \frac{\rho d V^2 H_{c_2}^{3.5} h^{2.5}}{\kappa_1^4\ \Phi_o^{1/2}} (1-h)^2 \left(\left[h^2 + \frac{0.18(1-h)^2}{(2\kappa^2-1)} \right]^{-1/2} + \frac{2.36(2\kappa^2-1)^{1/2}}{(1-h)} \right) . \tag{2.82}$$

c) Kramer's Theory

Kramer [1] considers the power loss due to the motion of the FLL at the moment it becomes depinned. This power loss is equal to the

elastic energy E_s that the moving FLL elements had prior to depinning. This energy is given by

$$E_s = \frac{1}{2} \frac{f_p^{*2}}{C} \quad , \tag{2.83}$$

where f_p^* is an effective interaction force, and C is the appropriate combination of elastic coefficients of the FLL. The depinning force density, F_d, needed to move the FLL a distance a_o, the lattice parameter, can be expressed as

$$F_d = -2\rho \frac{E_s}{a_o} = -F_p \quad , \tag{2.84}$$

where ρ is the density of pinning centers.

Kramer's theory predicts two different depinning mechanisms. At low fields, the FLL remains elastic and depins by breaking individual bonds with the pinning centers, as shown in Figure 7. At high fields, the shear strength of the lattice decreases and the lattice deforms plastically around the pinned fluxoids. At these fields, strongly pinned fluxoids remain pinned; the lattice plastically deforms only in the areas where the fluxoids are not individually pinned or are weakly pinned. The resulting pinning force for a given reduced field is dictated by that mechanism, elastic or plastic, which yields the lowest magnitude depinning force for that reduced field. An example of a pinning force resulting from the elastic and plastic mechanisms is shown in Figure 8.

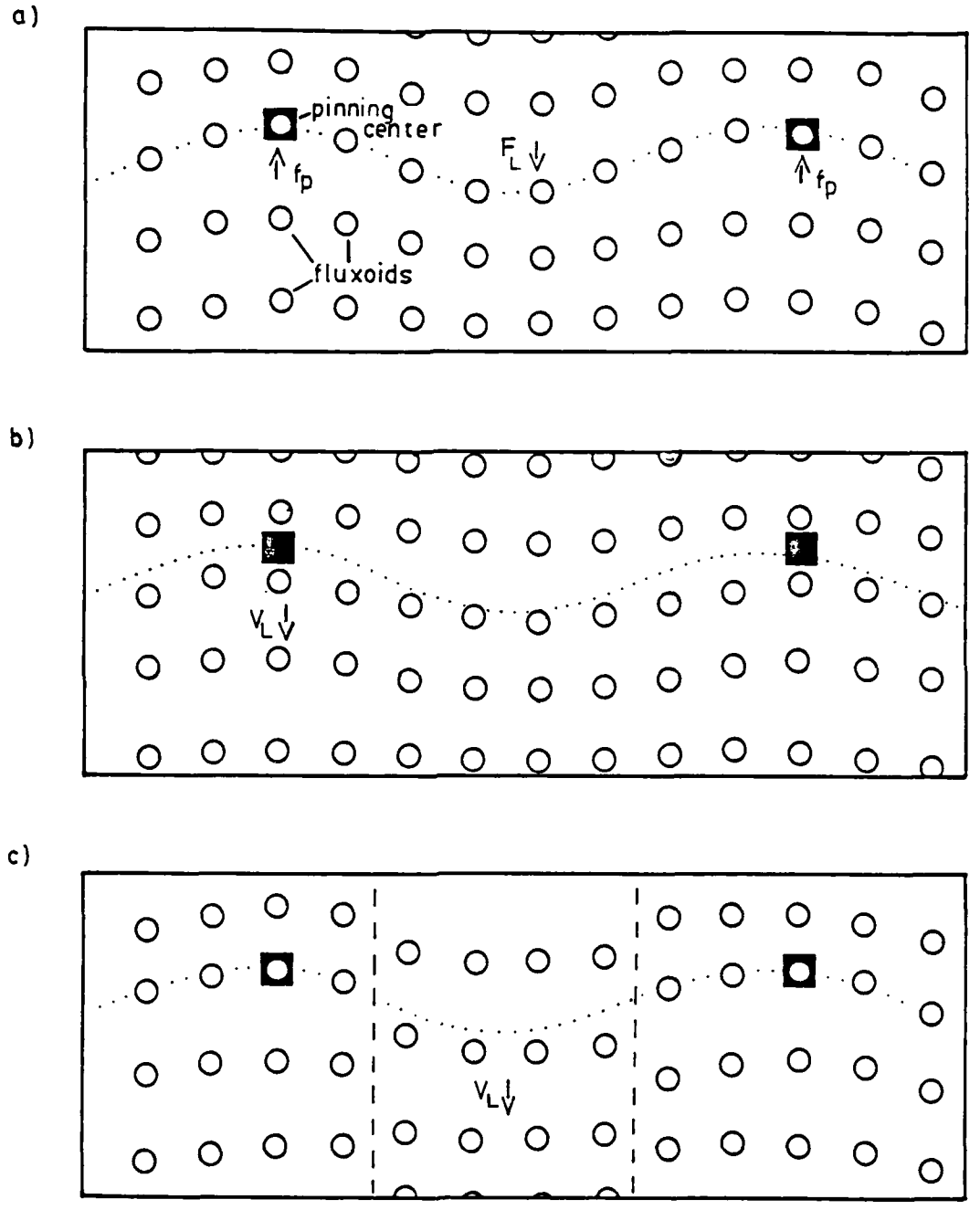

Figure 7) Schematic representation of a pinned FLL under the influence of the Lorentz force where: a) the FLL lattice bends elastically, b) the FLL dislodges from the pinning centers, and c) individual fluxoids remain pinned but the lattice deforms plastically between the pinned fluxoid.

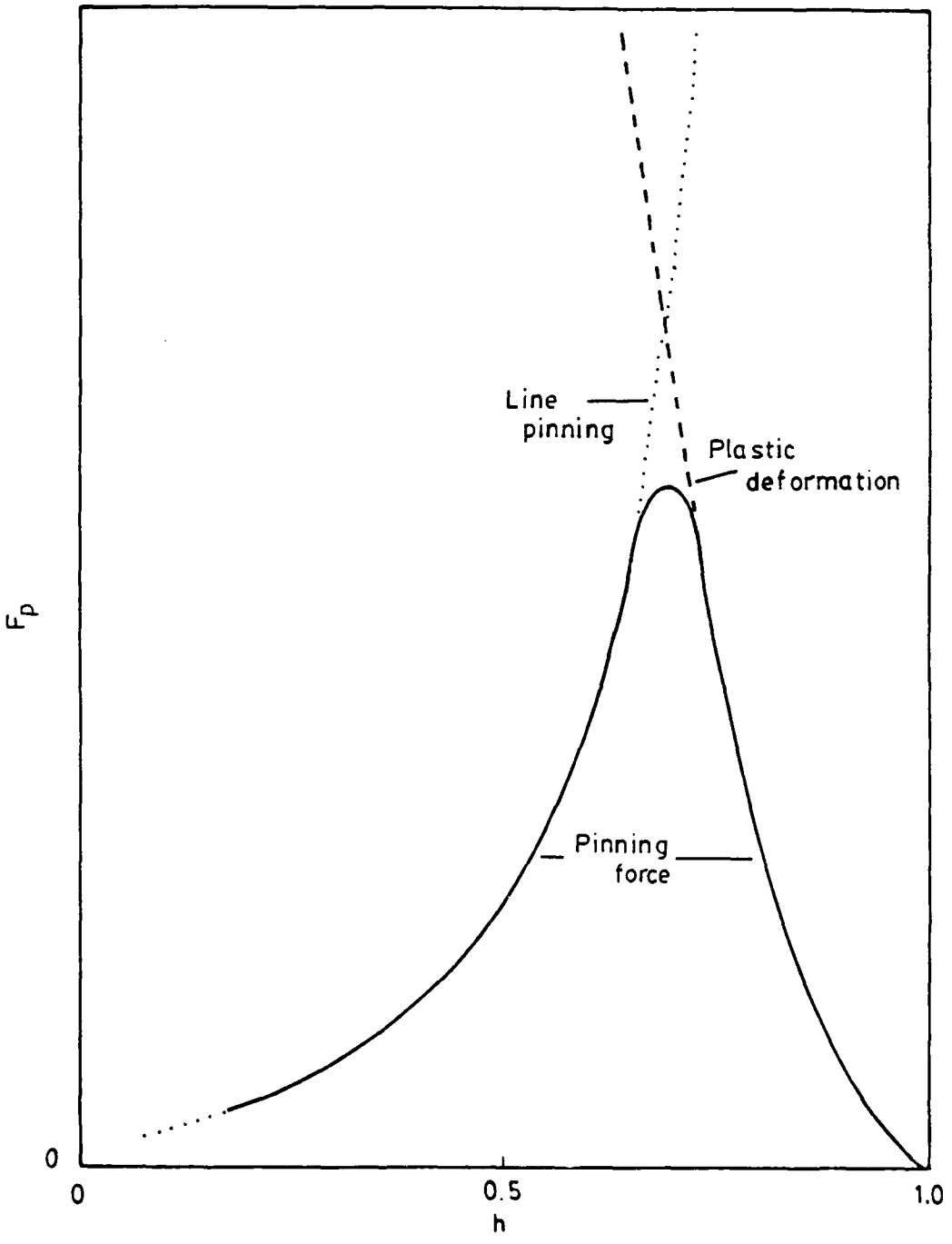

Figure 8) Reduced field dependence of the pinning force density due to the line-pinning mechanism and to the plastic deformation mechanism.

The elastic response of the lattice is further subdivided in two reduced-field regions. At very low fields, the fluxoids are very flexible; pinned fluxoids bend easily under the influence of the Lorentz force. Furthermore, the FLL can also shear elastically about a pinned fluxoid. Therefore, in this limit, the elastic moduli c_{44} and c_{66} are needed to describe the elastic reaction of the FLL to a pinning center. On the other hand, at higher fields a fluxoid becomes stiffer, and if the distance between the pinning centers along its length is small, the fluxoid will barely be able to bend. The fluxoid now has the appearance of being pinned along its length by a line pinning center. Elastically, the FLL can only shear, therefore, only c_{66} is needed to describe the elastic response of the FLL. The low field region, where a fluxoid can bend about a pinning center, is called the point-pinning region. The reduced field region, where the fluxoid appears to be pinned by a line pinning center, is called the line pinning region. The reduced field h_L at which there is the transition from point-pinning to line-pinning is dictated by the relative stiffness of a fluxoid as compared to the shear strength of the flux lattice, and by the distance between pinning centers. This reduced field, h_L, can be obtained from

$$h_L^{2/3} = \frac{c_{66}}{c_{44}} \frac{B}{h_o} \quad . \tag{2.85}$$

The point-pinning region is of little interest because as the magnetic field is increased, the critical current drops

rapidly to very low values. On the other hand, in the line-pinning region, there is a rapid increase in critical current as the reduced field increases. Therefore, more emphasis is given to the line-pinning region.

The elastic energy per flux line, E_s, can be calculated from the interaction force f_p. In the line pinning region, the interaction force per unit length of fluxoid is

$$f_{p_l} = n_l f_p \quad , \tag{2.86}$$

where n_l is the number of pinning centers per unit length of a flux line. The flux line lattice can shear in order to thread through more pinning centers. Therefore, the effective interaction force f_p^* is proportional to the displacement of the lattice f_{p_l}/c_{66}, thus,

$$f_p^* \propto \frac{f_{p_l}^2}{c_{66}} \quad . \tag{2.87}$$

The elastic energy density per unit length of pinned fluxoid E_{s_l}, obtained from Equation (2.82), is proportional to

$$E_{s_l} \propto \frac{n_l^2 f_p^{*2}}{c_{66}} \quad . \tag{2.88}$$

The use of Equations (2.86) and (2.87) in Equation (2.88) yields

$$E_{s_l} \propto \frac{n_l^6 f_p^4}{c_{66}^3} \quad . \tag{2.89}$$

One now obtains from Equation (2.84) the relation

$$F_p \propto \rho_1 \frac{n_i^6 f_p^4}{a_o c_{66}^3} \quad , \tag{2.90}$$

where ρ_1 is the density of pinned fluxoids per cross-sectional area. The use of Equations (2.45), (2.48), and (2.66) yields the pinning force density for the line-pinning region

$$F_p \propto \rho_1 \eta_1^4 V^4 H_{c_2}^{4.5} \frac{(2\kappa_1^2-1)^3 \, h^{6.5}}{\kappa_1^8 \quad (1-h)^2} \quad . \tag{2.91}$$

The shear strength of the FLL decreases as the magnetic field is increased. At a reduced field h_p, the Lorentz Force exceeds the maximum shear strength of the FLL. Thus, the elastic response of the FLL is supplanted with plastic deformation of the lattice.

To calculate the pinning force limit due to plastic deformation, Kramer considers a simple system consisting of pinning planes, separated by a distance y. The surface of the plane lies parallel to the Lorentz force. For such a system, the shear stress τ_{xy} of the FLL can be approximated by [34]

$$\tau_{xy} = \left(\frac{1}{2} y - x \right) F_L \quad , \tag{2.92}$$

where x is the distance from the surface of a pinning plane. Setting x at the position of maximum stress, namely at $x = \frac{1}{2} a_o$, the above equation can be expressed as

$$F_L = \frac{2\tau_{max}}{y\left(1 - \frac{a_o}{y}\right)} \quad , \tag{2.93}$$

where τ_{max} can be approximated by

$$\tau_{max} = \frac{c_{66}}{2\pi} \quad . \tag{2.94}$$

Kramer calculates the stored energy density, ρE_s, to be

$$\rho E_s = \frac{F_L^2 y^2}{24 c_{66}} \quad . \tag{2.95}$$

Substituting in this equation the value of F_L given in Equation (2.93), Equation (2.84) becomes

$$F_p = \frac{c_{66}}{12\pi^2 \left(1 - \frac{a_o}{y}\right)^2 a_o} \quad . \tag{2.96}$$

Substituting Equations (2.45) and (2.48) into (2.96), one obtains

$$F_p = \frac{0.14}{\left(1 - \frac{a_o}{y}\right)^2} \frac{H_{c_2}^{5/2}}{\kappa_1^2} h^{1/2} (1-h)^2 \quad . \tag{2.97}$$

For a more realistic model (parallel pinning planes are not very realistic) the biggest change in this equation is in the dependence on the microstructure. Furthermore, Kramer's theory is based on a simplistic version of the plastic deformation phenomena because he does not take into account the fluxoid-lattice defects. Plastic deformations usually start and/or propagate along lattice defects. This will have an unknown effect on the form of the pinning force density. Regardless of the model used, the depinning force density due to the plastic-deformation mechanism is probably weakly dependent on the precipitate density, and it is probably independent of the interaction force f_p.

d) Other Theories

Schmucker [35] calculates the pinning force in the plastic deformation region by means of a Green's function which describes the elastic behavior of the FLL. Schmucker states that the pinning force density can be expressed as

$$F_p = 4\Pi\rho f_p^* d_{||} d_{\perp} \quad , \tag{2.98}$$

where f_p^* is an effective interaction force that depends on the elasticity of the lattice, and $d_{||}$, $d_{\perp}$ are the dimensions of the pinning centers parallel and perpendicular, respectively, to the flux lines. The shear stress τ_s, derived from the FLL Green's function equals

$$\tau_s = f_p d_{\perp} G \quad , \tag{2.99}$$

where G can be approximated by

$$G \approx \frac{5.47 \times 10^{-2}}{0.93 + \left(\frac{c_{44}}{c_{66}} \frac{d_{||}}{d_{\perp}} \right)^{1/2}} \quad . \tag{2.100}$$

At the threshold of plastic deformation, when the shear stress is at a maximum, one can define an effective interaction force f_p^* by means of Equation (2.98) as being equal to

$$f_p^* = \frac{\tau_{max}}{d_{\perp} G} \quad , \tag{2.101}$$

Schmucker uses a maximum shear stress of the form

$$\tau_{max} \approx \frac{c_{66}}{50} \quad , \tag{2.102}$$

therefore, using Equation (2.100) and (2.101), f_p^* becomes

$$f_p^* = 0.36 \frac{c_{66}}{d_\perp} \left[0.93 + \left(\frac{c_{44}}{c_{66}} \frac{d_{||}}{d_\perp} \right)^{1/2} \right] \quad . \tag{2.103}$$

Using this equation and Equations (2.47) and (2.48), Equation (2.98) can be rewritten as

$$F_p = 0.065 \, \rho d_{||} d_\perp H_{c_2}^2 \cdot \frac{(1-h)^2}{(2\kappa^2-1)}$$

$$x \left[0.93 + \frac{d_{||}}{d_\perp} (2.367) \sqrt{2\kappa^2-1} \, \frac{h}{(1-h)} \right] \quad . \tag{2.104}$$

For high values of κ and when $d_{||} \approx d_\perp$, this equation can be approximated by

$$F_p \approx \frac{0.11 \; d^2 H_{c_2}^{\;2} \, h(1-h)}{\kappa_1} \quad . \tag{2.105}$$

Campbell and Evetts [9] have proposed, without a rigorous treatment, a different mechanism to explain the increase in critical currents at certain fields. They state that at low fields there is such a low density of fluxoids that most pinning centers are not near fluxoids, so these unused pinning centers do not contribute to the pinning force density. As the field is increased, the fluxoid density increases. The fluxoids thread more pinning centers, in other words, they synchronize better with the pinning-center density. However, at a certain field h_s, there are no more unused

pinning centers to synchronize with, so there cannot be any further increases in the pinning force density. As the field is increased from h_s, the pinning force density decreases because the elementary interaction force of the pinning centers decreases.

CHAPTER III

SPECIMENS AND APPARATUS

This investigation consisted of two stages. The specimens were prepared and analyzed by K. Moll, under the supervision of Dr. W.R. Bitler of the Department of Material Sciences of The Pennsylvania State University. The author performed the second stage, namely, the final preparation, and the measurement of superconducting and electrical properties of the specimens. To acquire this data, the specimens were mounted in a sample holder and cooled, using liquid helium as a refrigerant. The resistance ratio, transition temperature, and critical currents of the specimens were measured with a four-probe method.

A) Specimens

1) Starting Materials

The superconductors studied in this investigation are high-purity vanadium, and vanadium alloyed with niobium or gallium. Vanadium and niobium are the only intrinsic Type II superconductors. Marker [2] used vanadium because of its availability in high purity, and its controllable microstructure. We chose gallium as an alloying agent because carbon has more affinity to vanadium than to gallium, therefore, the formation of gallium carbides in the V-Ga specimens is unlikely. Also, the literature shows that the transition temperature of vanadium does not drop too much with the addition of small

concentrations of gallium [34,34,39,40]. Finally, superconducting V-Ga alloys are technologically important. Niobium was selected for its electronic and superconducting similarities with vanadium.

The starting materials were obtained from Materials Research Corporation. The vanadium arrived in 0.0254-cm x 2.54-cm x 61.0-cm foils of 99.95% nominal purity. The alloys, which arrived in 1.27-cm-diameter ingots, were made with vanadium of 99.9% nominal purity, and 99.999%-pure gallium or 99.99%-pure niobium. The alloy concentrations, given in atomic percents, were V-3.96a/o Ga, V-1.05a/o Ga, V-0.20a/o Ga, and V-4.10a/o Nb.

2) Annealing and Carburization

The specimens are annealed to reduce the lattice defects that can cause fluxoid pinning. This process creates crystal grains approximately 2-mm in diameter with surfaces near the {001} planes. Carbon is added to the vanadium or vanadium alloy in order to obtain normal precipitates that act as pinning centers. The vanadium-carbide precipitates in the form of disks along the {310} habit planes. Therefore, the disks align with their surface at 90°, 71.6°, and 18° to the specimen surface. Aging, which means heating for a definite period of time, coarsens the precipitates; that is, it increases their volume at the expense of neighboring precipitates. The precipitate thickness is roughly proportional to the square root of the precipitate diameter. The precipitates stress the lattice, therefore, the larger precipitates tend to become incoherent with the lattice.

The Material Science group supervised by W.R. Bitler annealed and carburized the specimens. The specimens are annealed at a pressure of 10^{-6} torrs and at a magnesium-gettered oxygen partial pressure of less than 10^{-17} torrs. Ohmic self-heating, produced by passing a large current through the specimen, is used to anneal the specimens at 1,500°C. Carburization is also done at this temperature. A measured volume of a 2.08 vol. % methane in a hydrogen carrier is introduced into the vacuum chamber. The methane decomposes, with the carbon going into solid solution in the hot specimen. Specimens to be aged are sealed at a pressure of 10^{-6} torrs in Pyrex capsules. They are then heated in a muffle furnace at 350°C. Aging times vary from 30 minutes to 36 hours. (For more information on the annealing, carburization and aging of vanadium, consult Schuyler [30]).

3) Analysis of Specimen Microstructure

The microstructure of the specimens was analyzed with a Phillips EM 200 transmission electron microscope. Results of this analysis are shown in Table 1. Apparently, the addition of gallium slows down the coarsening of the precipitates. For example, specimen #68, which is pure vanadium with 0.20a/o C and was aged for one hour, has a mean precipitate volume 10^3 larger than that of specimen #71, which is a V-1.05a/o Ga alloy with the same carburization treatment as #68.

Roughly half of the specimens were carburized on an apparatus that permitted a slow cooling from the carburizing temperatures.

Table 1. Composition, Aging Time, and Microstructural Analysis of the Specimens

Specimen #	a/o C	Aging at 350°C hrs	ρ x 10^{12} pp/cm^3	Diameter Å	V_p x 10^6(Å)^3	ρV_p x 10^{-3}
			Pure vanadium specimens			
8	0.0	-	-	-	-	-
50	0.0	-	-	-	-	-
54	0.0	-	-	-	-	-
41	0.0	-	annealed, then cold rolled to 75% reduction			
76	0.07	0.0	almost solid solution			
77	0.07	0.5	1,943	244	0.991	
78	0.07	3.0	699	397	2.41	1.69
82	0.07	10.0	396	524	4.84	1.92
83	0.13	0.0	24.7	1,968	179	4.42
94	0.13	0.5	16.5	2,726	305	5.04
96	0.13	1.0	141	976	28.4	3.99
70	0.20	0.0	8.69	3,648	665	5.78
56	0.20	0.0	8.74	3,839	688	6.01
49*	0.20	0.0	N.A.	N.A.	-	-
68	0.20	1.0	5.61	4,143	999	5.61
58	0.20	1.0	5.57	4,011	1,053	5.87
65	0.20	3.0	13.4	2,860	374	5.04

*Inadvertly aged in situ after carburization, due to slow cooling

-Distinct second distribution of precipitates of smaller size

N.A. Not Available

Table 1. Composition, Aging Time, and Microstructural Analysis of the Specimens (Continued)

Specimen #	a/o C	Aging at 350°C hrs	ρ x 10^{12} pp/cm^3	Diameter Å	V_p x 10^6(Å)^3	ρV_p x 10^{-3}
35*	0.40	0.0	4.23	6,404	2,610	11.0
24*	0.60	0.0	1.64	8,494	5,804	9.53
24-			84.7	1,393	86.9	7.63
23*	0.60	0.5	1.05	11,708	13,736	14.5
23-			542	523	5.11	2.77
22*	0.60	0.5	N.A.	N.A.	-	-
19*	0.60	1.0	0.932	6,207	5,771	5.38
19-			458	957	22.6	10.4
			V - 0.20a/o Ga			
86	0.13	0.0	-	solid solution		-
90	0.13	1.0	N.A.	N.A.	-	-
93	0.13	1.0	4,339	248	0.734	3.19
91	0.13	3.0	2,929	314	1.36	3.99
92	0.13	5.0	2,261	337	1.69	3.82
			V - 1.05a/o Ga			
30	0.0	-	-	-	-	-
61	0.20	0.0	-	solid solution		-
42*	0.20	0.0	1,874	425	2.96	5.54
43*	0.20	0.5	1.256	476	3.83	4.81
71	0.20	1.0	4,415	302	1.11	4.89
32*	0.20	1.0	2.453	382	1.94	4.75

Table 1. Composition, Aging Time, and Microstructural Analysis of the Specimens (Continued)

Specimen #	a/o C	Aging at 350°C hrs	ρ x 10^{12} pp/cm^3	Diameter Å	V_p x 10^6(Å)^3	ρV x 10^{-3}
60	0.20	3.0	13,058	192	0.364	4.76
69	0.20	10.0	4,524	295	1.02	4.64
81	0.20	36.0	3,670	309	1.28	4.68
84	0.20	2.hrs at 500°C	50.3	1,759	95.2	4.79
		V - 2.96a/o Ga				
7	0.0	-	-	-	-	-
5	0.0	-	cold rolled from starting material; not annealed			
63	0.20	0.0	17,310	170	0.270	4.67
33*	0.20	0.0	4,669	311	1.10	5.12
17*	0.20	0.5	N.A.	N.A.	-	-
44*	0.20	1.0	7,520	246	0.640	4.81
62	0.20	5.0	5,579	269	0.854	4.77
67	0.20	10.0	8,223	237	0.613	5.04
9*	0.40	0.0	2.15	7,568	4,582	9.87
10*	0.40	0.5	2.54	6,518	4,017	10.14
		V - 4.01a/o NB				
27*	0.0	-	-	-	-	-
28*	0.20	0.05	1,153	528	4.30	4.96
29*	0.20	1.0	1,197	537	4.52	5.41
45*	0.20	1.0	6,945	265	0.805	5.59
51*	0.20	2.0	8.630	238	0.610	5.26
52*	0.40	1.0	1,003	675	10.4	10.43

Unfortunately, this slow cooling was responsible for some aging in situ, roughly equivalent to a couple of hours of aging at 350°C. The apparatus was modified for subsequent specimens, allowing a faster quench from the carburizing temperature and minimizing the aging in situ.

4) Cutting and Polishing Procedures

The specimens are electrochemically cut and polished using a solution of 20% sulfuric acid, 80% methanol, and a few drops of water. The solution is kept cool by running tap water through a submersed glass coil. Eleven volts are applied between the specimen and two stainless-steel cathodes immersed in the etchant. Mechanical stirring minimizes the anodic layer that forms on the specimen surface. A proper combination of electrode position and stirrer speed is critical for obtaining specimens with uniform thickness.

The 0.254-mm thick specimens are first electrochemically thinned to a thickness of 0.15 mm. They are then coated with "Microstop Stop Off Lacquer," which is manufactured by the Michigan Chrome and Chemical Co. Then strips of lacquer are cut using a brass template and peeled off. The specimens are reimmersed in the etchant, exposing to the acid the outline of the desired shape. After the cutting operation, the remaining lacquer is peeled off and the specimens are cleaned with acetone. A final etch thins the specimens to 0.10 mm.

The final shape of a sample is shown in Figure 9. The wide end-tabs, ultrasonically tinned with indium, improve the electrical contact to the current leads and the thermal contact to the sample

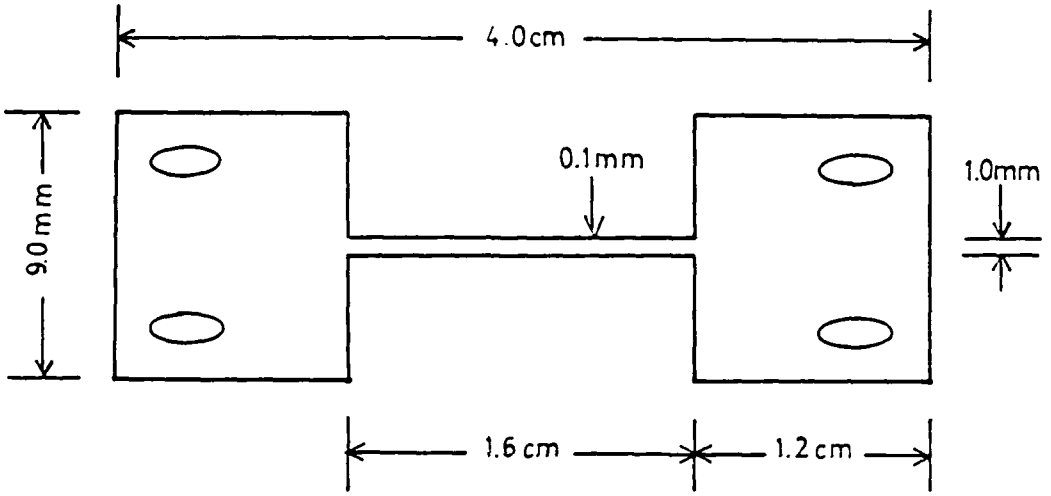

Figure 9) Specimen shape.

block. Indium-solder flows through the holes etched at each end, improving the mechanical bond between the tabs and the current leads. The thin center strip is designed for voltage measurements along its length with the four-probe method. The cross-sectional area of the center strip is kept at a minimum in order to achieve high current-densities with the available current sources. Furthermore, decreasing the total current decreases the ohmic heating at the current-lead/specimen contact.

B) Hardware

The specimens are mounted on a copper block which contains all the pertinent sensors. The specimen block is designed to fit inside a vacuum-tight brass can. The can is positioned inside a liquid helium filled finger dewar so that the specimen is located at the center of a superconducting magnet. Figure 10 shows the specimen holder and dewar system.

1) Specimen Block

The specimen block, shown in Figure 11, is made of copper half-cylinders, separated by a 0.127-mm thick teflon insulator. The halves are held together by four stainless steel bolts. A cloth-phenolic insulator around the top half of each bolt prevents the bolts from electrically shorting the two copper halves. The sample block contains a recording thermometer, which is a germanium resistance thermometer; a heater, which is a 50Ω nicrome wire epoxied around the copper block; a regulating thermometer, which is

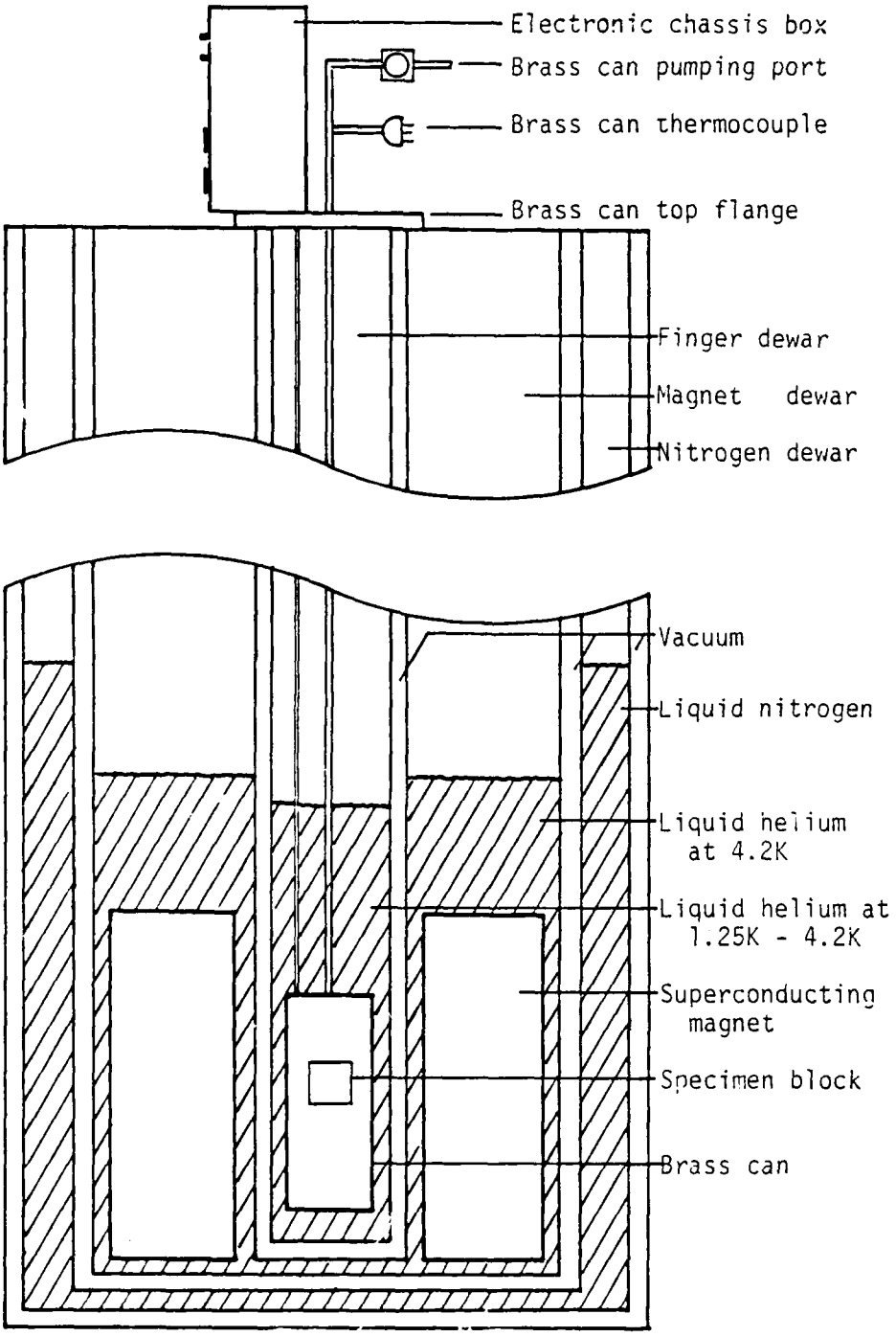

Figure 10) Schematic representation of the specimen holder and cryostat.

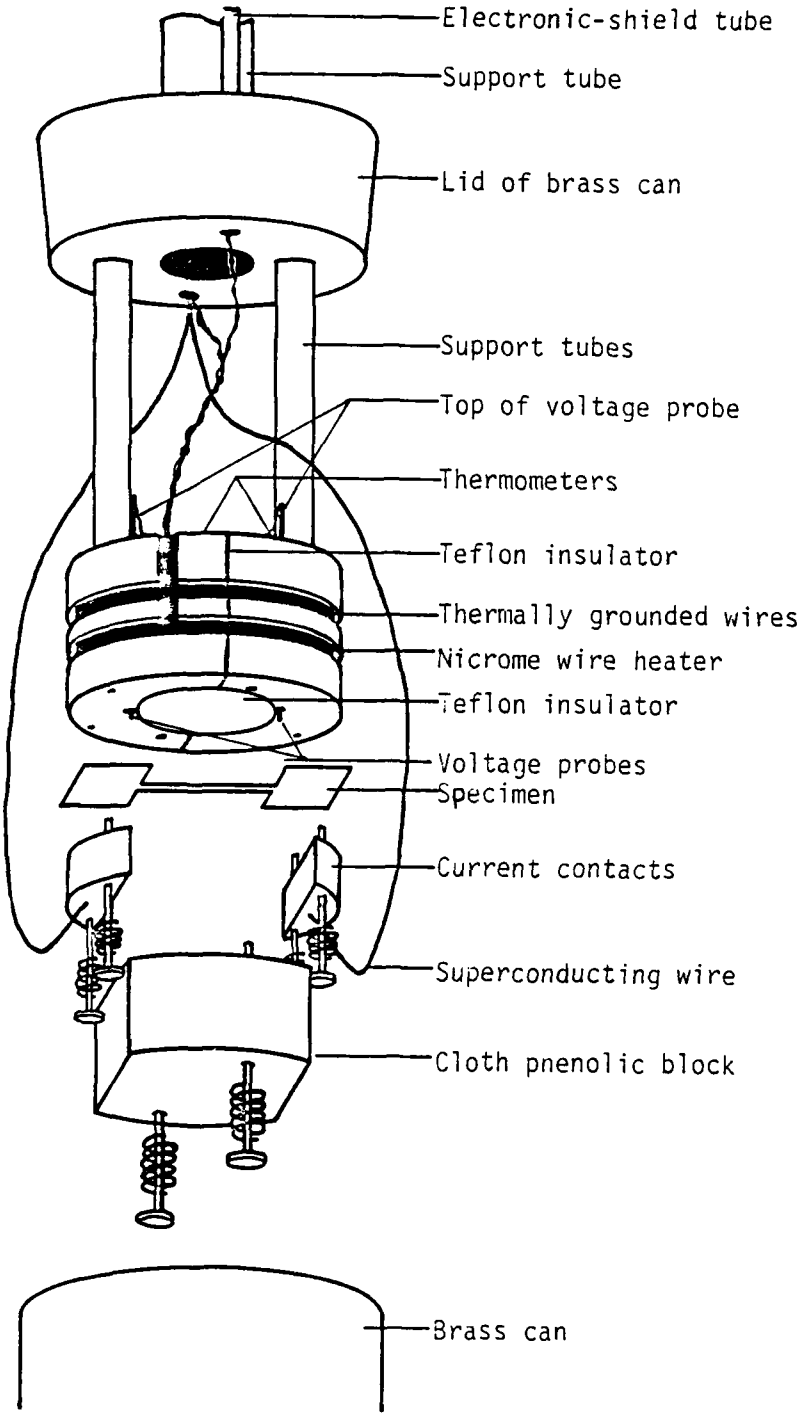

Figure 11) Specimen block.

a 100Ω carbon resistor; and two vertical, spring-loaded voltage probes. All the wires coming to these devices are passed through the liquid helium bath, thereby eliminating heat leaks into the sample through the wires. They are then wound several times around the blocks and epoxied in place, thermally grounding them to the block.

The specimens are mounted on the bottom of the block, perpendicular to the insulated division between the halves. A 0.127-mm thick teflon foil electrically insulates the center part of the specimen from the copper block. The end tabs of the specimen come in direct thermal contact with the copper block; a dab of Dow Corning 200 fluid of 60,000-centistopes viscosity enhances this thermal contact. Superconducting, multifilimentary Nb_3Sn (in a copper matrix) wires, which carry the transport current for the four probe method, are ultrasonically soldered to thick copper-contacts. These contacts are designed to be soldered to the tinned specimen-tabs.

2) Block Support

The specimen block fits inside a 5.1-cm diameter, 20.3-cm long, vacuum-tight brass can. It is supported by two thin wall, stainless-steel tubes. Thus, the block does not come in direct contact with the liquid helium bath, enabling its temperature to be regulated at a value above the bath temperature. Helium gas is introduced in the can to a pressure of 60 to 100 militorrs. The gas provides thermal contact between the bath and the copper block.

The can is suspended from a brass flange by a 0.95-cm diameter, 96.5-cm long, thin-wall stainless steel tube. The voltage and thermometer leads are enclosed inside a 0.64-cm diameter stainless steel tube parallel to the support tube, to minimize electronic-noise pick-up. The support tube is connected at the top flange to a pumping port used to evacuate the brass can to the desired pressure level. The top flange also supports an aluminum electronic-chasis, which contains all the electrical connections to the copper block. Low-thermal input connectors are used in the chassis for the voltage leads of the four-probe method in order to minimize thermal emfs.

3) Cryostat and Superconducting Magnet

The brass can enclosing the sample block is designed to fit inside a finger dewar filled with liquid helium. The temperature of the liquid helium is regulated by controlling the pressure inside the finger dewar with a manostat.

The sample block is located at the center of a superconducting magnet which surrounds the lower part of the finger dewar. American Magnetics, Inc. fabricated the solenoid from multifilamentary NbTi wire. The field homogeneity is one part in 10^5 over a 2.5 cm diameter volume around the specimen location. A Didcot Instrument Co., Ltd. Model DPSA/100/4.5/1 power supply provides the magnet current. A resistor of 10mΩ, which is in series with the solenoid, is used for measuring the current for fields above 5K Oe. An external resistor of 0.2649Ω in series with the solenoid

is used for lower fields in order to increase the current readout-voltage sensitivity at these fields. The voltage across these resistors is read, nominally to four significant digits, with a Keithley Model 190 digital multimeter. The magnetic field is calibrated versus the magnet current by proton nuclear magnetic resonance to an absolute accuracy of $\pm$0.2 Oe.

C) Electronics

1) Four-Probe Method

The four-probe voltage versus current method used to measure the critical current is shown schematically in Figure 12. Two power FET's powered by a D-8D truck battery provide up to 20 amps. The controlling ramp-circuit is optically isolated from the power FET's in order to prevent noise-producing ground-loops. Ramp speeds are monitored in order to have a slow approach to J_c. The total ramping time from J = 0 to J_c is usually more than one minute. The current is determined by measuring the voltage developed across a series 0.025Ω resistor.

The voltage along the center part of the specimen is amplified 10^6 times by a Keithley 148 nanovoltmeter. The 8 Hz noise from the nanovoltmeter's chopper is eliminated with a low pass filter on the output of the nanovoltmeter.

A Hewlett-Packard 7001A-M x-y recorder is used to plot specimen voltage versus current. Coupled with the nanovoltmeter it shows a resolution of 100 nv/cm and noise level generally below 10 nv.

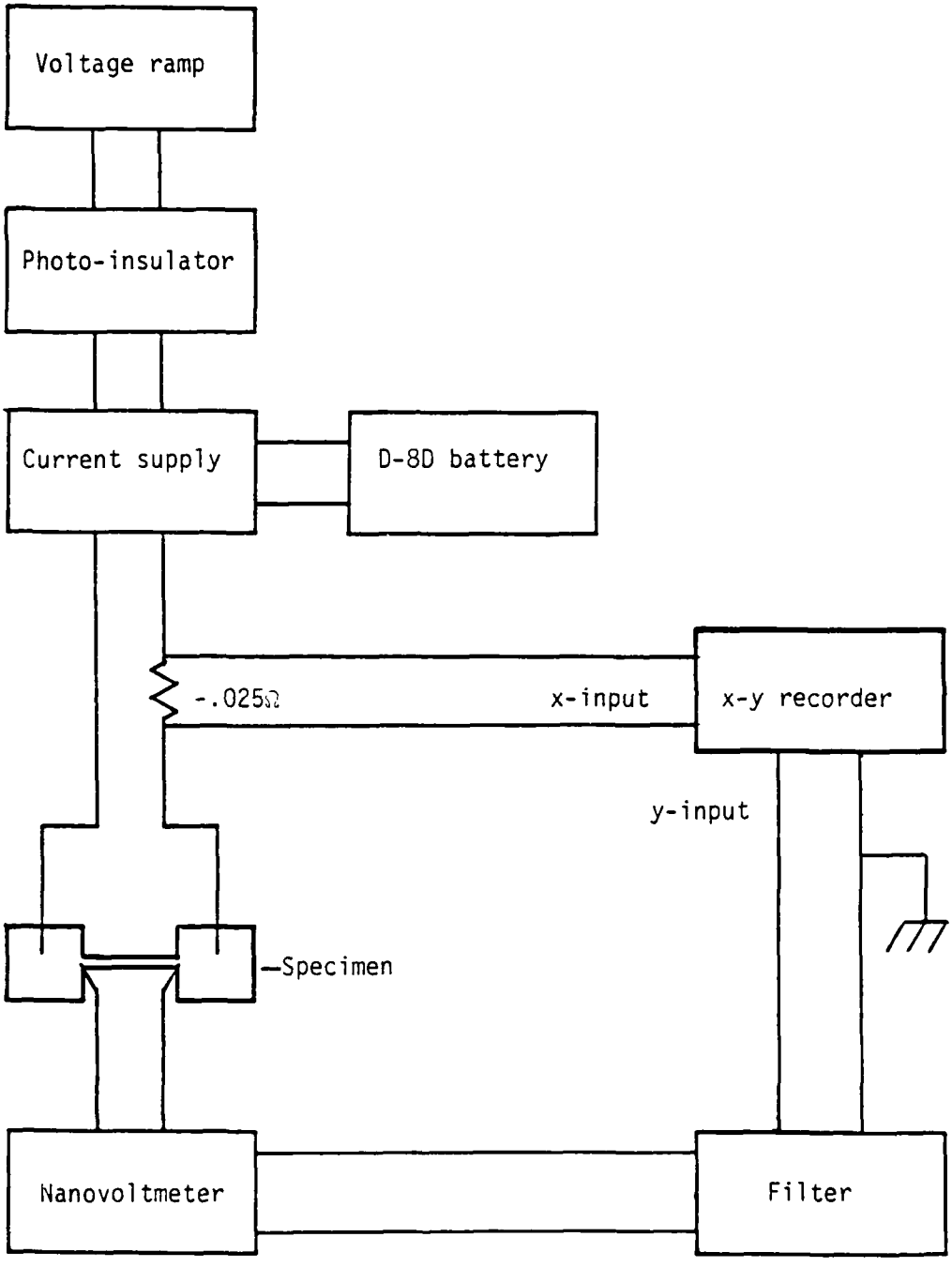

Figure 12) Schematic diagram of the equipment used to measure the critical current, showing the location of the electronic ground.

2) Temperature Control

The temperature of the specimen was controlled using the two systems shown in Figure 13. The first system measures the temperature, the second regulates it. The temperature is obtained from a Cryo Cal, Inc. germanium Cryo Resistor using a four probe method. The thermometer resistance varies from 3861Ω at 1.5K, to 95.59 Ω at 10.0K. A constant-current source provides a current of 1.191 μA or 13.31 μA through the thermometer. The higher current is only used for temperatures above 3.5K. The voltage across the Cryo Resistor is amplified by a Hewlett-Packard 740B Standard/Differential Voltmeter. The voltage is then displayed on a Digitec digital millivoltmeter, which has a four-digit display.

The Cryo Resistor was factory calibrated only down to 1.5K. We calibrated it from 4.2K to 1.125K with a carefully calibrated germanium-resistance thermometer and with the 1958 Liquid-Helium Pressure Scales [41]. There is good agreement between the three calibrations, with a maximum deviation of 1.6% at 1.5K. To obtain a smooth scale from 1.125K to 10.0K, the following scheme is used:

i) $1.125<T<1.5$ - standard resistor's calibration is used,

ii) $1.5\leq T<2.0$ - logarithmic average of standard resistor's calibration and factory calibration is used,

iii) $2.0\leq T\leq 10.0$ - factory calibration is used.

Temperature regulation consists of three parts; the liquid-helium thermal-bath, the specimen-block heater, and a temperature-feedback system. To maintain a constant temperature, the heat supplied to

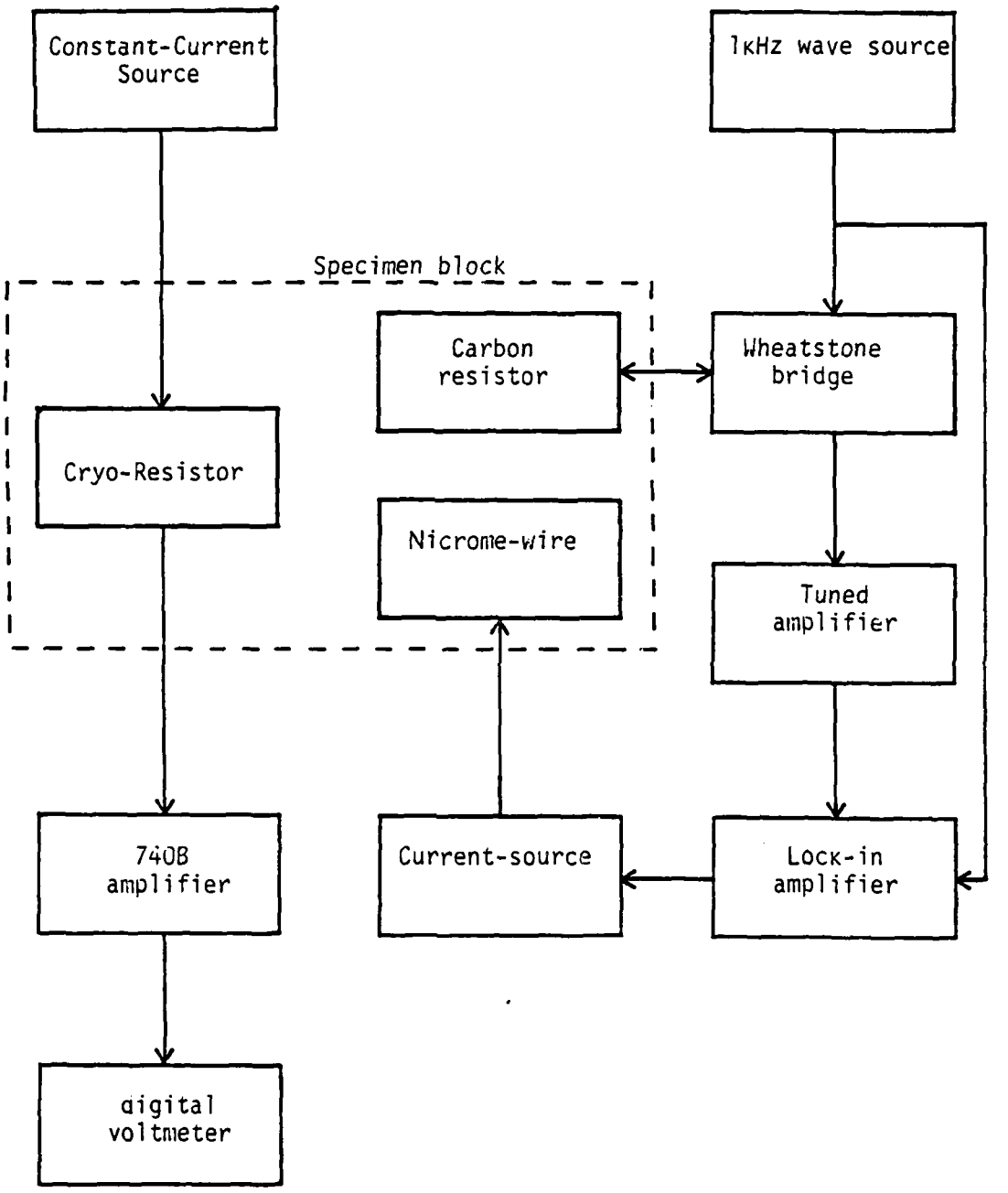

Figure 13) Block diagram of the equipment used to monitor and control the specimen-block temperature.

the sample block has to balance the heat conducted to the helium bath. The bath is maintained at 0.25K below the desired block temperature. The stainless steel tubes supporting the sample block (see Figure 10), the copper wires, and the helium gas inside the brass can, provide the thermal contact between the block and the helium bath. The block is heated to the desired temperature by a 50Ω nicrome wire heater (see Figure 11) controlled by a feedback system.

The core of the feedback system is a 100Ω carbon resistor, which is the fourth leg of a Wheatstone bridge. The resistor is coated with Dow Corning 200 fluid of 60,000 centistokes to assure thermal contact with the copper block where it is imbedded. A carbon resistor is used because, in contrast to the germanium thermometer, it has a resistance which is independent of magnetic fields. A low-amplitude 1 kHz current is sent through the bridge. The voltage across the bridge is measured by a Keithley 840 lock-in amplifier. The output of this amplifier controls the nicrome-wire-heater power supply. The temperature dependence of the carbon resistor is used to regulate the block temperature. The bridge is balanced when the resistance of the carbon resistor equals that of an external control resistor. A change on the resistance of the carbon resistor, induced by a change in temperature, creates a signal across the bridge. The phase and amplitude of this signal directs the lock-in amplifier to command an increase or decrease, as needed, of the heater current. Heater currents between 6 and 15 ma are needed to maintain a given temperature. A change in the

value of the control resistor in the Wheatstone bridge changes the temperature at which the system balances. Temperatures from 1.5K to above 6K can be maintained within $\pm$0.5%. (For more details on the electronics involved, see Marker [2].)

CHAPTER IV

DATA AQUISITION AND RESULTS

A) Fundamental Properties

1) Basic Thermodynamic and Electronic Properties

The electronic mean free path, ℓ, and the electronic specific heat, γ, are frequently used to calculate various superconducting parameters. For small concentrations of impurities, the electronic specific heat is almost a constant. Therefore, the value of 1.179×10^4 erg cm^{-3} deg^{-2}, given by Radebaugh and Keesom [10] for pure vanadium, is used for all our specimens.

The effect of impurities on the electronic mean free path, however, is appreciable. Hence, the electronic mean free path is calculated for all the specimens from the low temperature resistivity, ρ_o. By far, the biggest source of error in measuring the resistivity is the measurement of the physical dimensions of the specimens. To circumvent this problem, the resistance ratio is used to calculate the low temperature resistivity.

The resistance at room temperature, R_{295}, and the low temperature resistance, R_o, were obtained for each specimen from voltage versus current plots. These plots were made with the four probe method illustrated in Figure 12. The nanovoltmeter was not used for these measurements; the voltage was recorded directly by the x-y recorder. For vanadium specimens with values for the low temperature resistivity as high as those for our specimens, the

value of the resistance of the normal specimen obtained at any temperature below 6K is within 2% of that obtained at zero temperature [41]. Therefore, to simplify procedures, R_o was obtained at a temperature just above the critical temperature of the specimen. This temperature never was above 6K.

The physical dimensions of the specimens were measured in order to calculate their resistivity. This was done after the superconducting data had been acquired because mechanical damage, incurred during the measurement of the specimen dimensions, could affect the superconducting properties. The specimen thickness was measured with a micrometer in several places along the center strip. The width and length were measured with an optical comparator.

The resistivity of a metal results from the addition of the resistivity due to the thermal motion of lattice ions, ρ_l, and that due to scattering from impurities ρ_e [42], so that

$$\rho = \rho_l + \rho_e \quad . \tag{4.1}$$

At the temperature at which R_o was measured, ρ_l for vanadium is almost zero [41], thus

$$\rho \approx \rho_e \quad . \tag{4.2}$$

For small concentrations of impurities, ρ_i is fairly impurity independent, thus, one can say that at room temperature ρ_i is almost a constant for all our specimens. From Equations (4.1) and (4.2) one can approximate $\rho_{i_{295}}$ with

$$\rho_{i_{295}} \approx \rho_{295} - \rho_o \quad , \tag{4.3}$$

which leads to

$$\rho_{295} - \rho_o \approx \text{constant} \quad . \tag{4.4}$$

Table 2 shows the value of this difference for our specimens. Excluding specimens #32, 33 and 49, whose value of $\rho_{295} - \rho_o$ deviate from the mean by more than two standard deviations, the average value of $\rho_{295} - \rho_o$ for the specimens is given by

$$\overline{\rho_{295} - \rho_o} = 2.50 \times 10^{-5} \Omega\text{-cm} \quad , \tag{4.5}$$

with a standard deviation of $3.4 \times 10^{-6} \Omega$-cm. The value given in Equation (4.5) is about 20% higher than that found by other authors [10, 43, 44]. This discrepancy is probably due to a systematic overestimation of the cross-sectional area of our specimens. The V - 4.01a/o Nb specimens were not included in the average given by Equation (4.5). These specimens show a consistently higher value for this equation. There is no evident reason for this behavior.

Table 2. Resistivity and Related Parameters.

Specimen #	ρ_{295} x $10^{-5}\Omega$-cm	$\rho_{295} - \rho_o$ x $10^{-5}\Omega$-cm	r_1	ρ_o' x $10^{-6}\Omega$-cm	ℓ Å
		pure vanadium specimens			
8	-		20.87		
50	2.632	2.500	18.85	1.327	264
54	2.858	2.721	19.77	1.266	276
41	2.449	2.301	15.62	1.602	218
76	2.405	2.246	14.16	1.767	198
77	2.480	2.351	18.21	1.374	255
78	2.424	2.313	20.86	1.199	292
82	2.622	2.474	16.79	1.490	235
83	2.658	2.464	12.96	1.931	181
94	2.353	2.116	8.95	2.795	125
96	2.543	2.403	17.14	1.460	240
70	2.449	2.303	15.80	1.584	221
56	2.880	2.696	14.66	1.707	205
49	1.338	1.122	5.20	4.814	73
68	2.437	2.316	19.07	1.312	267
58	3.202	3.040	18.73	1.336	262
65	2.712	2.578	19.27	1.298	270
35	2.121	2.008	17.90	1.398	250
24	3.553	3.376	19.01	1.316	266
23	N.A.	-	N.A.	-	-

N.A. Not Available

Table 2. Resistivity and Related Parameters (Continued).

Specimen #	ρ_{295} x $10^{-5}\Omega$-cm	$\rho_{295} - \rho_o$ x $10^{-5}\Omega$-cm	r_1	ρ'_o x $10^{-6}\Omega$-cm	ℓ Å
22	N.A.	-	4.48	5.58	63
19	2.958	2.801	17.81	1.405	249
		V - 0.20a/o Ga			
86	2.792	2.250	4.149	6.030	58.0
90	N.A.	-	4.529	5.524	63.4
93	3.071	2.422	3.731	6.705	52.2
91	3.246	2.623	4.205	5.950	58.8
92	N.A.	-	4.026	6.215	56.3
		V - 1.05a/o Ga			
30	5.372	3.280	1.568	15.96	21.9
61	4.084	2.629	1.806	13.85	25.3
42	3.846	2.392	1.645	15.21	23.0
43	3.747	2.318	1.622	15.42	22.7
71	3.347	2.144	1.782	14.04	24.9
32	6.612	4.126	1.660	15.07	23.2
60	4.349	2.826	1.855	13.49	25.9
69	3.996	2.539	1.743	14.35	24.4
81	3.182	2.025	1.751	14.29	24.5
84	3.549	2.251	1.735	14.42	24.3
		V - 2.96a/o Ga			
7	N.A.	-	1.20	20.85	16.8
5	N.A.	-	0.54	46.33	7.55
63	6.938	3.267	0.890	28.12	12.4

Table 2. Resistivity and Related Parameters (Continued).

Specimen #	ρ_{295} x $10^{-5}\Omega$-cm	$\rho_{295} - \rho_o$ x $10^{-5}\Omega$-cm	r_1	ρ_o x $10^{-6}\Omega$-cm	ℓ Å
33	6.703	3.746	1.267	19.75	17.7
17	5.117	2.652	1.076	23.25	15.1
44	4.673	2.517	1.168	21.42	16.3
62	4.851	2.276	0.884	28.30	12.4
67	4.299	2.017	0.884	28.30	12.4
9	N.A.	-	1.08	23.17	15.1
10	5.289	2.644	1.000	25.02	14.0
		V - 4.01a/o Nb			
27	4.242	3.357	3.795	8.329	42.0
29	4.875	3.838	3.70	8.543	41.0
45	3.301	2.616	3.821	8.273	42.3
51	3.859	2.977	3.377	9.360	37.4
52	3.877	3.017	3.507	9.013	38.8

In order to minimize the random error in measuring the physical dimensions of the specimen, a low temperature resistivity ρ_o' was calculated from the resistance ratio r_1, which is given by

$$r_1 = \frac{R_{295} - R_o}{R_o} \quad . \tag{4.6}$$

Using r_1 and Equation (4.5), one obtains

$$\rho_o' = \frac{R_o}{(R_{295} - R_o)} \overline{(\rho_{295} - \rho_o)} = \frac{1}{r_1} \; 2.50 \times 10^{-5} \Omega/\text{cm} \quad . \tag{4.7}$$

The value of $\overline{\rho_{295} - \rho_o} = 3.16 \times 10^{-5} \Omega$-cm is used for the V-Nb specimens. The values for ρ_{295}, $\rho_{295} - \rho_o$, r_1 and ρ_o' are listed in Table 2.

The resistance ratio r_2, which is sometimes used in the literature and is defined by

$$r_2 = \frac{R_{295}}{R_o} \quad , \tag{4.8}$$

is easily obtained from r_1 by using the relation

$$r_2 = r_1 + 1.0 \quad . \tag{4.9}$$

Figure 14 shows the resistance ratio as a function of the concentration of gallium. Niobium, with its electronic configuration similar to that of vanadium, produces less of an effect on the resistance ratio than gallium does. However, as noted before, niobium seems to affect the lattice resistivity.

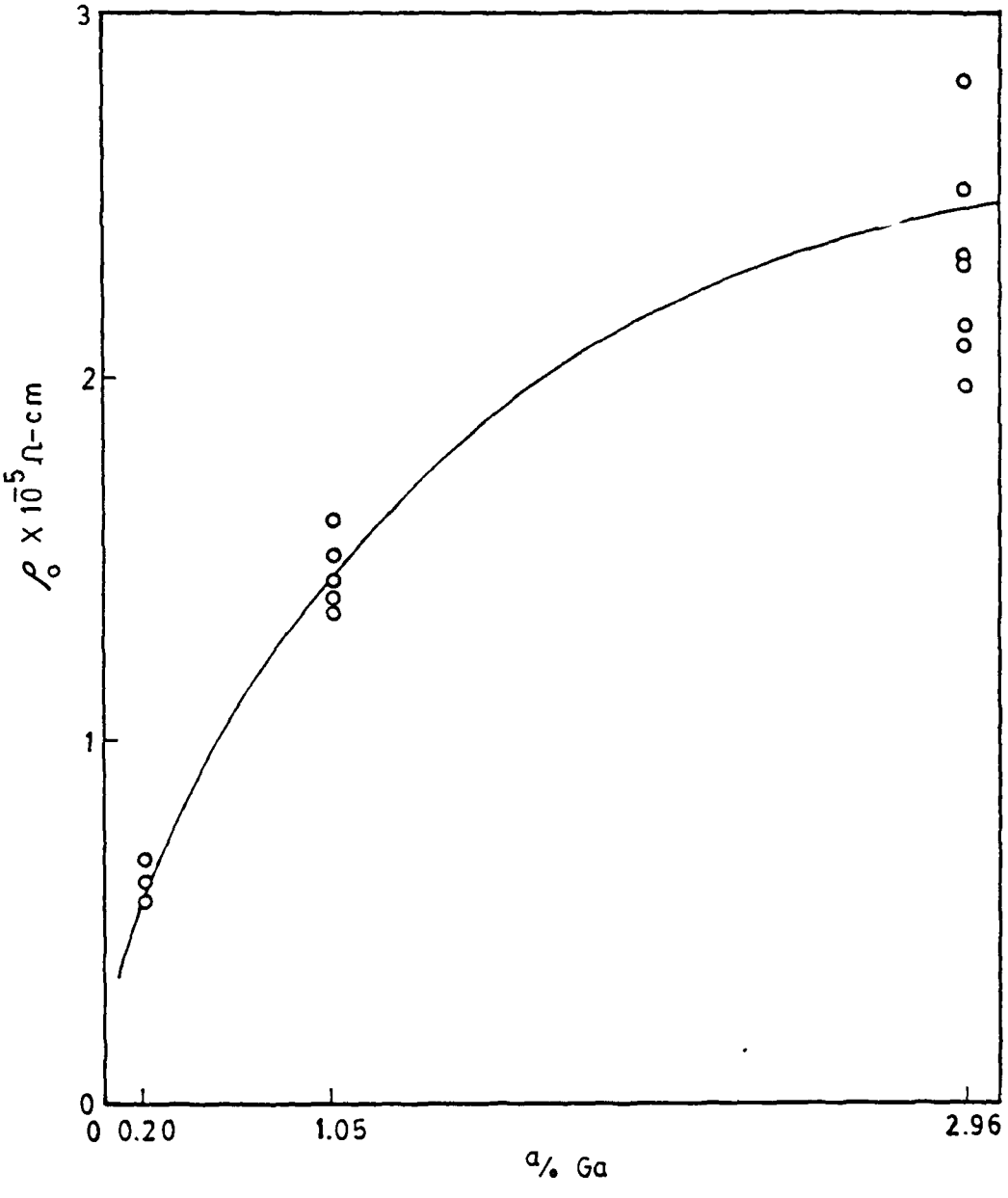

Figure 14) Resistivity versus concentration of gallium.

The electronic mean free path, ℓ, is computed from the equation [10]

$$\ell = \frac{6\pi^2}{he^2\rho_o S} \quad , \tag{4.10}$$

where h is Plank's constant and S is the area of the Fermi surface in K-space. Using the values given by Radebaug and Keesom [10], one obtains

$$\ell = \frac{3.50 \times 10^{-4}\text{Å}}{\rho_o} \quad , \tag{4.11}$$

where ρ_o is given in Ω-cm. Values for the mean free path using the resistivity ρ_o' given by Equation (4.7) are listed in Table 2.

2) Critical Temperature

The critical temperature is obtained from a plot of temperature versus sample resistance. First, the helium-bath temperature is lowered below the expected transition temperature. The germanium-thermometer output, amplified by the H.P. 740 B voltmeter, is connected to the horizontal axis of the x-y recorder (see Figure 15). The voltage across the specimen, amplified by the nanovoltmeter, is connected to the vertical axis of the x-y recorder. The specimen is heated momentarily to above its transition temperature. This is done in order to be able to set a small current (0.2 to 6.0 Amp/cm^2) producing 0.8 to 0.7 μV along the thin center section of the normal specimen. These current levels decrease the value of T_c for pure vanadium by less than 0.15% [41].

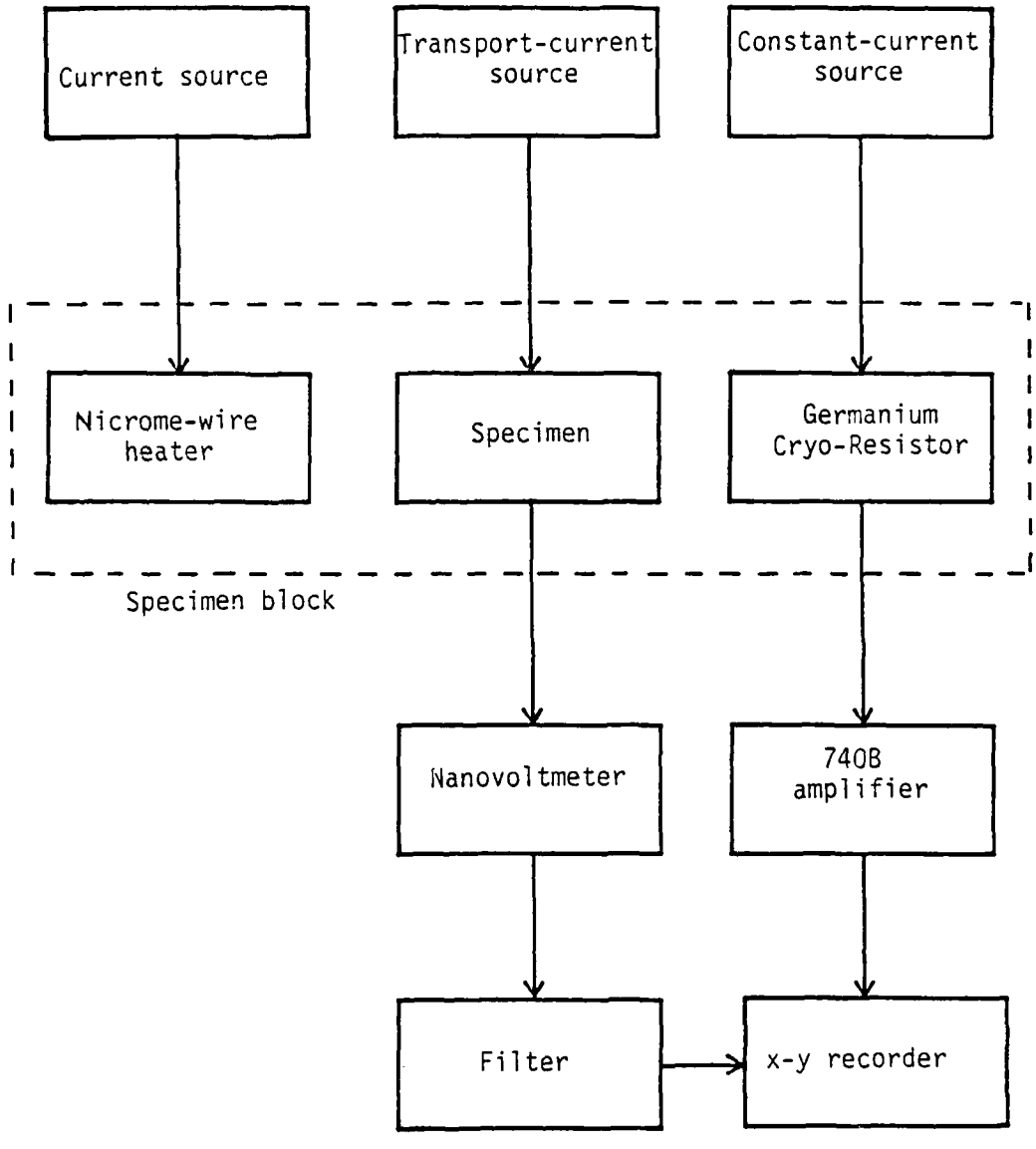

Figure 15) Block diagram of the equipment used to obtain the critical temperature.

The current level is set and the specimen is allowed to cool. While the temperature and voltage are recorded on the x-y recorder, the sample is heated until it becomes completely normal and then allowed to cool until it becomes superconducting again. The critical temperature is defined as that temperature which gives a resistance value midway between the fully normal value and zero, the superconducting value (see Figure 16). The average result of two increasing and two decreasing temperature cycles is recorded as being the critical temperature of the specimen.

The critical temperature, as defined above, is tabulated for all specimens in Table 3. This definition is somewhat arbitrary since other points in the transition curve can be chosen as T_c. The transition width, ΔT, is probably the result of lack of homogeneity in the material. Metals with a high degree of uniformity, such as pure single crystals, exhibit very sharp transitions with very small ΔT. Hence, the value of T_c for these metals is rather clearly defined. Inhomogeneous superconductors generally have variations in the value of T_c within the bulk. The width ΔT for these materials can be rather wide. Therefore, for inhomogeneous superconductors, an arbitrary definition of the critical temperature of the bulk is needed. For example, T_c can also be defined as that temperature at which the specimen starts to show resistance or as that temperature at which it becomes completely normal. Because of this ambiguity, the width ΔT is considered as a source of error

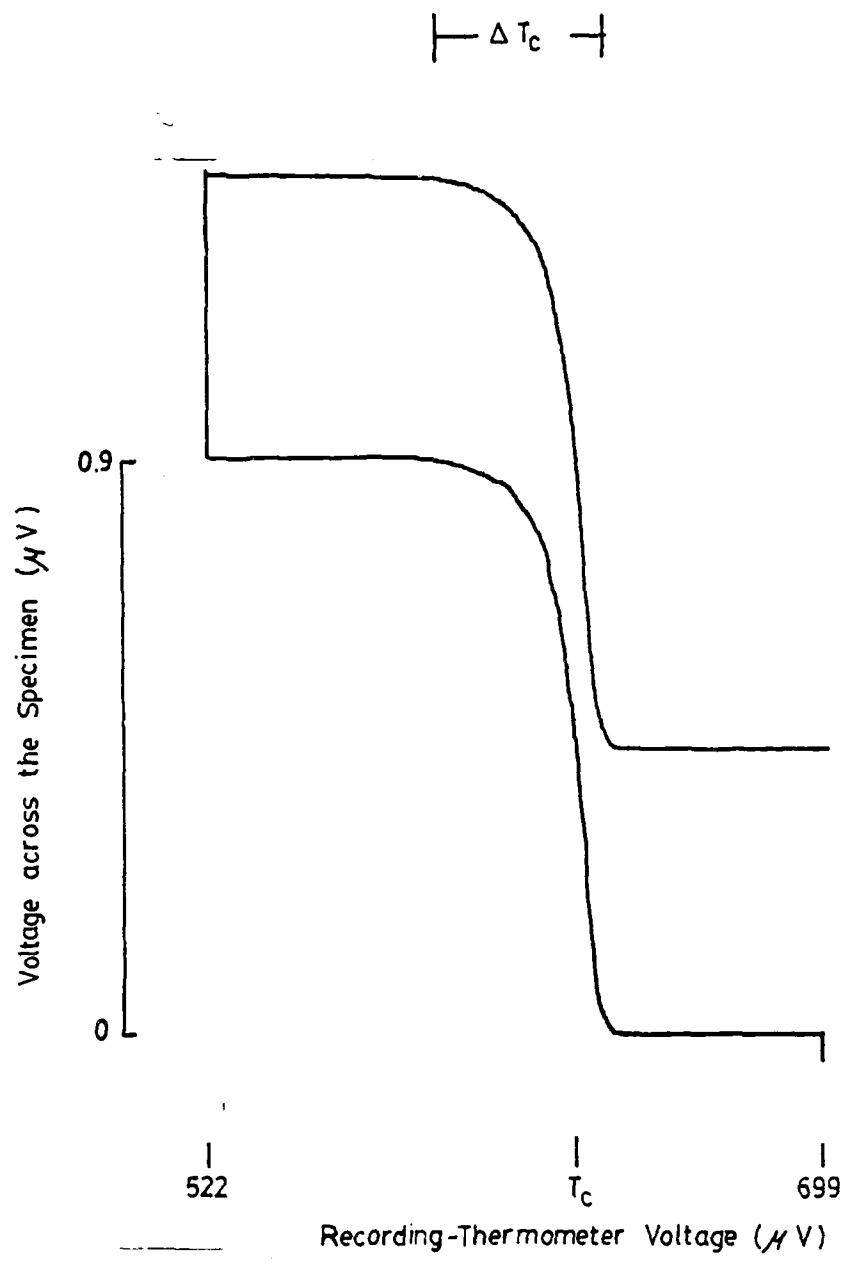

Figure 16) Voltage drop across specimen #96 as a function of the recording-thermometer voltage.

Table 3. Superconducting Parameters.

Specimen #	T_c K	ΔT_c %	η	$H_{c_2}(o)$ η=0.5 kOe	ΔH_{c_2} η=0.5 %
		pure vanadium specimens			
8	5.330	4.2	0.737	4.342	1.5
50	5.233	N.A.	N.A.	N.A.	-
54	5.242	2.3	0.551	4.571	0.9
41	5.290	2.0	0.601	4.896	0.9
76	5.173	1.7	0.498	5.365	1.5
77	5.219	2.0	0.459	4.597	1.6
78	5.241	0.5	0.337	4.275	2.8
82	5.221	1.8	0.483	4.683	1.6
83	5.193	1.6	N.A.	4.706	0.6
94	5.047	1.9	N.A.	6.142	2.0
96	5.223	1.9	N.A.	4.490	2.1
70	5.207	1.2	0.494	4.861	1.5
56	5.232	2.4	N.A.	N.A.	-
49	5.129	3.4	N.A.	N.A.	-
68	5.244	1.7	0.499	4.693	0.7
58	5.236	1.9	N.A.	N.A.	-
65	5.245	1.3	0.584	4.77	0.7
35	5.242	1.6	N.A.	N.A.	-
24	5.282	1.4	0.598	4.671	1.0
23	5.221	3.6	0.701	5.521	1.4

N.A. Not Available

Table 3. Superconducting Parameters (Continued).

Specimen #	T_c K	ΔT_c %	n	$H_{c_2}(o)$ n=0.5 kOe	ΔH_{c_2} n=0.5 %
22	4.740	5.2	0.654	8.531	1.7
19	5.245	2.5	0.647	4.719	1.8
		V - 0.20a/o Ga			
86	4.693	2.6	N.A.	10.120	1.1
90	4.770	3.1	N.A.	N.A.	-
93	4.640	2.7	N.A.	10.837	1.5
91	4.715	2.9	N.A.	10.173	1.9
92	4.734	2.0	N.A.	10.528	2.6
		V - 1.05a/o Ga			
30	3.825	4.5	0.410	16.497	0.13
61	4.054	4.8	0.546	16.108	0.43
42	3.866	3.5	0.558	16.710	0.36
43	3.840	3.0	0.520	16.755	0.64
71	4.007	2.4	N.A.	16.247	1.36
32	3.886	2.4	0.542	16.515	0.74
60	4.073	5.0	0.426	15.432	1.43
69	3.971	1.8	0.293	16.389	1.08
81	3.994	2.0	0.759	16.270	0.71
84	3.967	2.0	N.A.	16.584	0.90

Table 3. Superconducting Parameters (Continued).

Specimen #	T_c K	ΔT_c %	η	$H_{c_2}(o)$ η=0.5 kOe	ΔH_{c_2} η=0.5 %
		V - 2.96a/o Ga			
7	3.750	4.0	N.A.	N.A.	-
5	3.770	10.0	N.A.	N.A.	-
63	3.272	7.0	0.524	20.881	1.37
33	3.567	4.1	0.486	19.145	0.73
17	3.470	3.5	0.698	19.082	0.58
44	3.583	3.5	0.568	19.214	1.26
62	3.304	3.8	0.573	21.450	0.44
67	3.228	2.0	0.344	21.437	1.26
9	3.610	4.8	0.670	18.770	1.39
10	3.425	4.9	0.588	18.974	1.47
		V - 4.01a/o Nb			
27	4.755	2.7	0.612	12.712	0.89
28	4.513	3.3	N.A.	N.A.	
29	4.880	7.3	N.A.	N.A.	-
45	4.790	0.9	0.352	12.430	2.33
51	4.698	2.7	0.321	12.513	1.73
52	4.759	2.4	N.A.	N.A.	-

in defining T_c from our data. The width Δt is related to the homogeneity of the specimen as mentioned above. It is therefore useful when comparing the quality of the specimens.

The critical temperatures for our V-Ga and V-nB specimens are similar to those found by other authors for these alloys [36, 37,38,39,45,46].

The critical temperature is a function of the resistivity, ρ_o, because scattering by impurities decreases the value of the superconducting energy gap. Radebaugh and Keesom [10] suggest that this relationship might be linear. Figure 17 shows a plot of T_c versus ρ_o. The relationship is linear only at low values of ρ_o. Figure 18 shows a plot of the critical temperature versus r_2^{-1}. The linearity extends to higher alloy concentration than on the previous graph. By extrapolation this plot predicts a critical temperature for infinite mean free path, T_{c_o}, equal to 5.47K. This result was obtained from a least mean square fit to the straight line, excluding the V - 4.01 Nb specimens and specimen #49. This value of T_{c_o} is near the value of 5.41 $\pm$ 0.01K obtained by Radebaugh and Keesom [10]. However, Azhazha, et al. [41] report a value of 5.58 $\pm$ 0.03K for a specimen with a resistance ratio of 1370. Golovashkin, et al. [37] show a strong dependence of T_c on the conduction electron concentration. Niobium affects the conduction electron concentration of vanadium much less than gallium does, which might be the reason why the V - 4.01a/o Nb specimens do not fall on the same T_c versus r_2^{-1} curve for the gallium alloys.

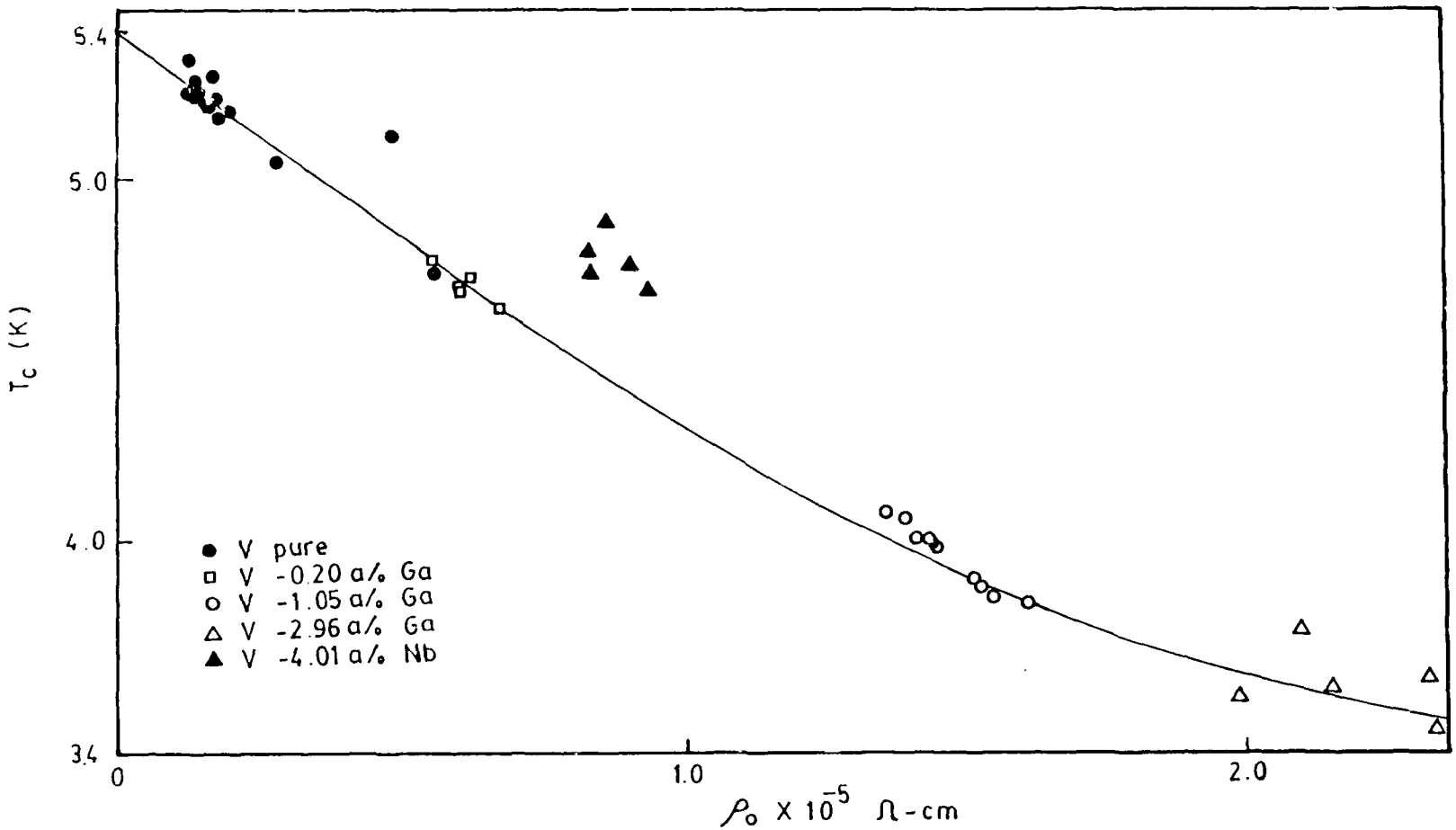

Figure 17) Variation of the critical temperature, T_c, versus the resistivity ρ_o. In this figure and in Figures 18, 21, and 22 each data point represents one specimen. However, in these figures, the heavy crowding of the pure vanadium specimens in a small area prevents a distinct showing of every one of these specimens.

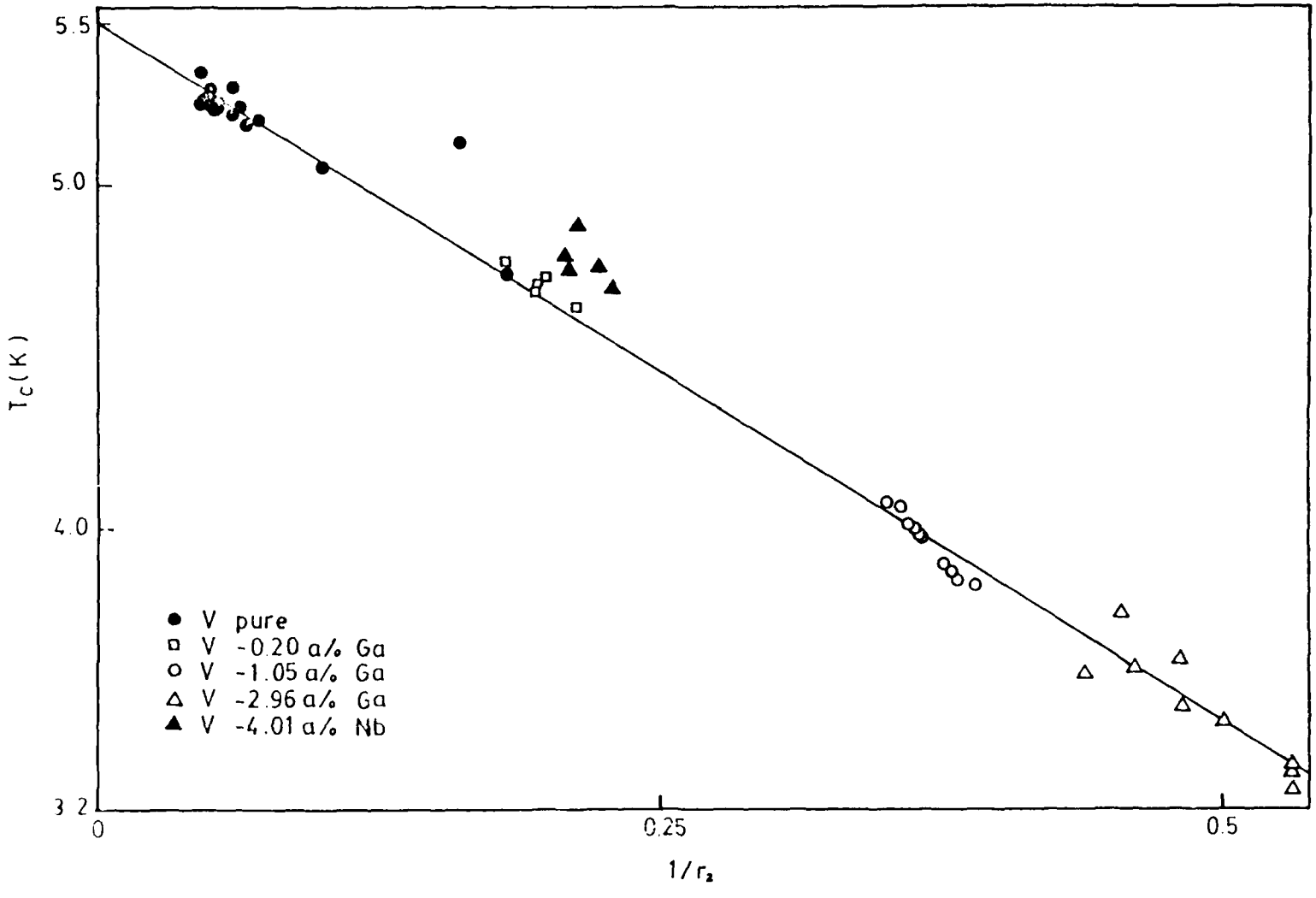

.riation of the critical temperature, T_c, versus the inverse of the resistance ratio, r_2.

AD-A118 288 PENNSYLVANIA STATE UNIV UNIVERSITY PARK APPLIED RESE--ETC F/G 20/11
VARIATION OF THE PINNING FORCE WITH MICROSTRUCTURE AND WITH THE--ETC(U)
SEP 81 P J JAVIER N00024-79-C-6043
UNCLASSIFIED ARL/PSU/TM-81-182 NL

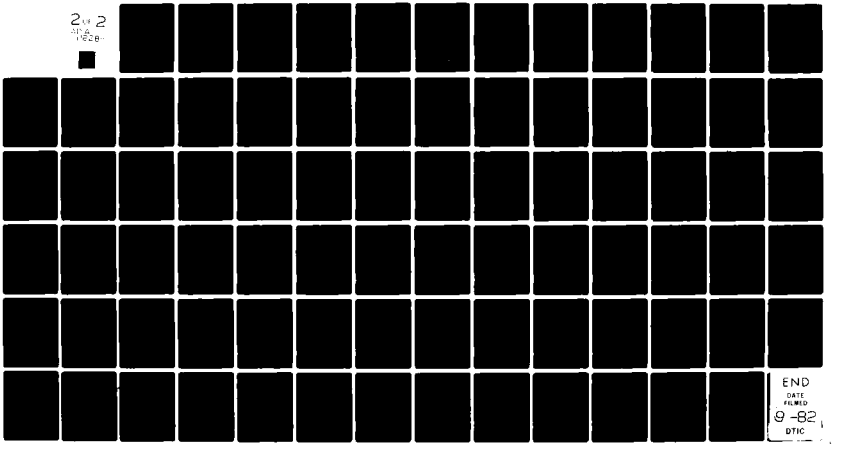

END
DATE FILMED
9-82
DTIC

3) Upper Critical Magnetic Field

The Upper Critical Magnetic Field, $H_{c_2}(t)$, is defined as that field at which the critical current extrapolates to zero. (Critical currents are discussed in section B-1 of this chapter.) This value depends on the equation used for the extrapolation. As noted in Chapter II, it is believed that at fields near $H_{c_2}(t)$, the fluxoid lattice depins by deforming plastically around the pinning centers. Thus, an equation describing the critical current under the influence of plastic deformation of the FLL is needed for the extrapolation. Traditionally, one of the following equations is used

$$J \propto (1-h) \quad , \tag{4.12}$$

or

$$J \propto h^{1/2}(1-h)^2 \quad . \tag{4.13}$$

Equation (4.12) is an empirical equation, later supported by Schmucker's theory (Equation 2.105). Equation (4.13) is derived from Kramer's theory (Equation 2.97). Figure 19 shows a sample fit of our data to each equation. Initially, the linear equation (Equation 4.12) was used, but it was found that, as seen in Figure 19, Equation (4.13) gives a better fit to our data.

The critical fields $H_{c_2}(t)$ calculated for several temperatures are fitted to an empirical equation in order to find the upper

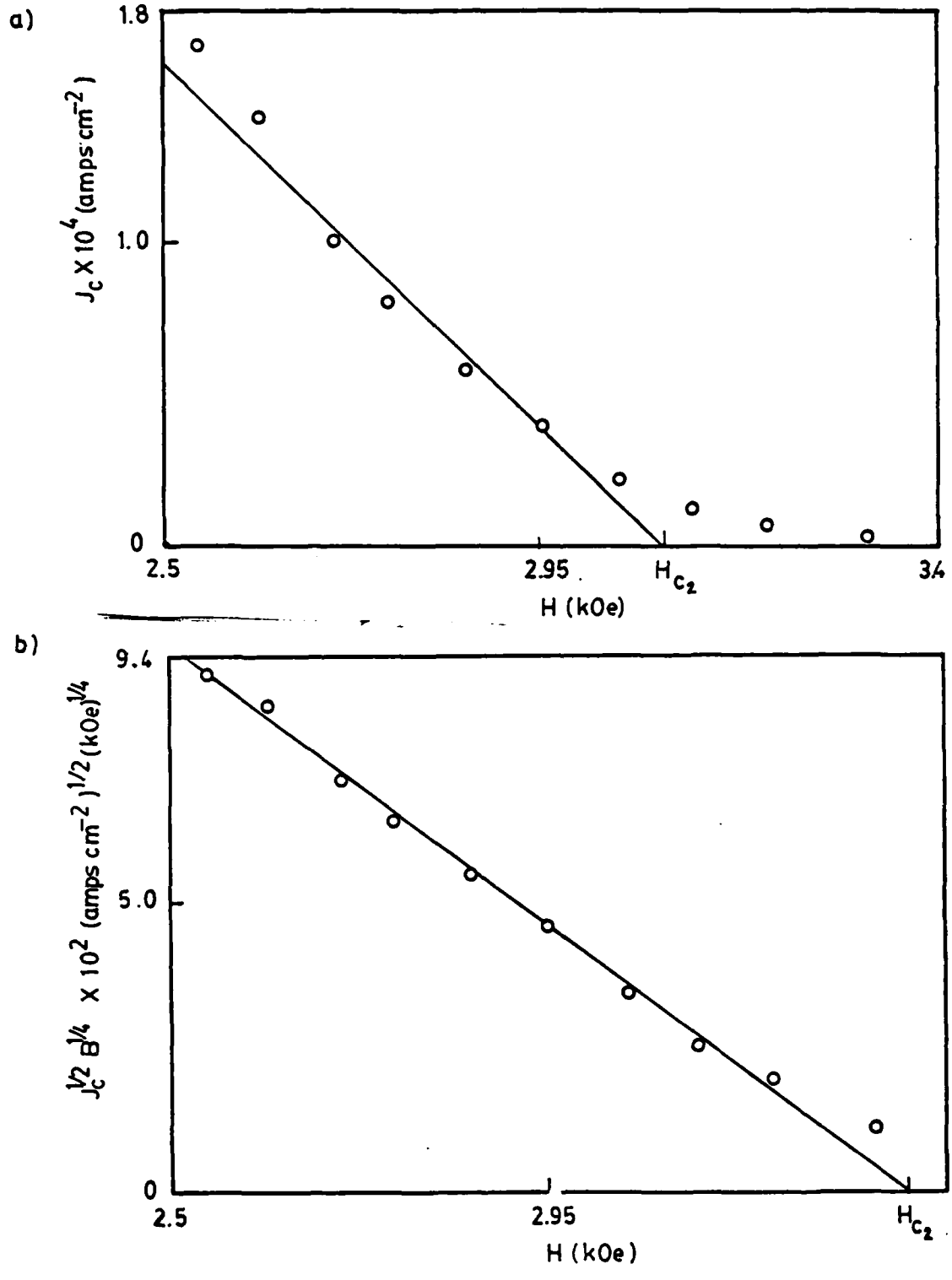

Figure 19) Extrapolation for $H_{c_2}(t)$, of specimen #65 at t = 2.5K, using a) $J \propto (1-h)$, and b) $J \propto h^{1/2}(1-h)^2$.

critical field at zero temperature $H_{c_2}(o)$. The empirical relation [47]

$$H_{c_2}(t) = H_{c_2}(o) \frac{(1-t^2)}{(1+\eta t^2)} \quad , \tag{4.14}$$

where η is a free parameter, is used since it gives a good fit to our data. The parameter η varies randomly for our specimens from 0.29 to 0.74, with the average being about 0.5.

The value η determines the shape of the curve given by Equation (4.14). When η and $H_{c_2}(o)$ are calculated simultaneously, the shape of this curve is adjusted in order to obtain the best least mean square fit of Equation (4.14) to the data. Small deviations in the empirical values of η change the shape of the curve. However, the value of $H_{c_2}(o)$ is dependent of this shape. Changes in the shape of the curve due to errors in $H_{c_2}(t)$ change the value of $H_{c_2}(o)$. Therefore, some errors in the data are amplified in the calculation for $H_{c_2}(o)$ if the value of η calculated for each specimen is used. For this reason, the value $\eta = 0.5$, which is the average for all specimens, is used in the calculation for $H_{c_2}(o)$ using Equation (4.14). A sample fit to this equation is shown in Figure 20. The values of η, and of $H_{c_2}(o)$ using $\eta = 0.5$ are shown in Table 3.

Once $H_{c_2}(o)$ is found, an uncertainty in $H_{c_2}(o)$, $\Delta H_{c_2}(o)$, is measured by predicting values of $H_{c_2}(t)$, using Equation (4.14) for the temperatures studied, and comparing these values to the experimental values for those temperatures. The difference between the values is

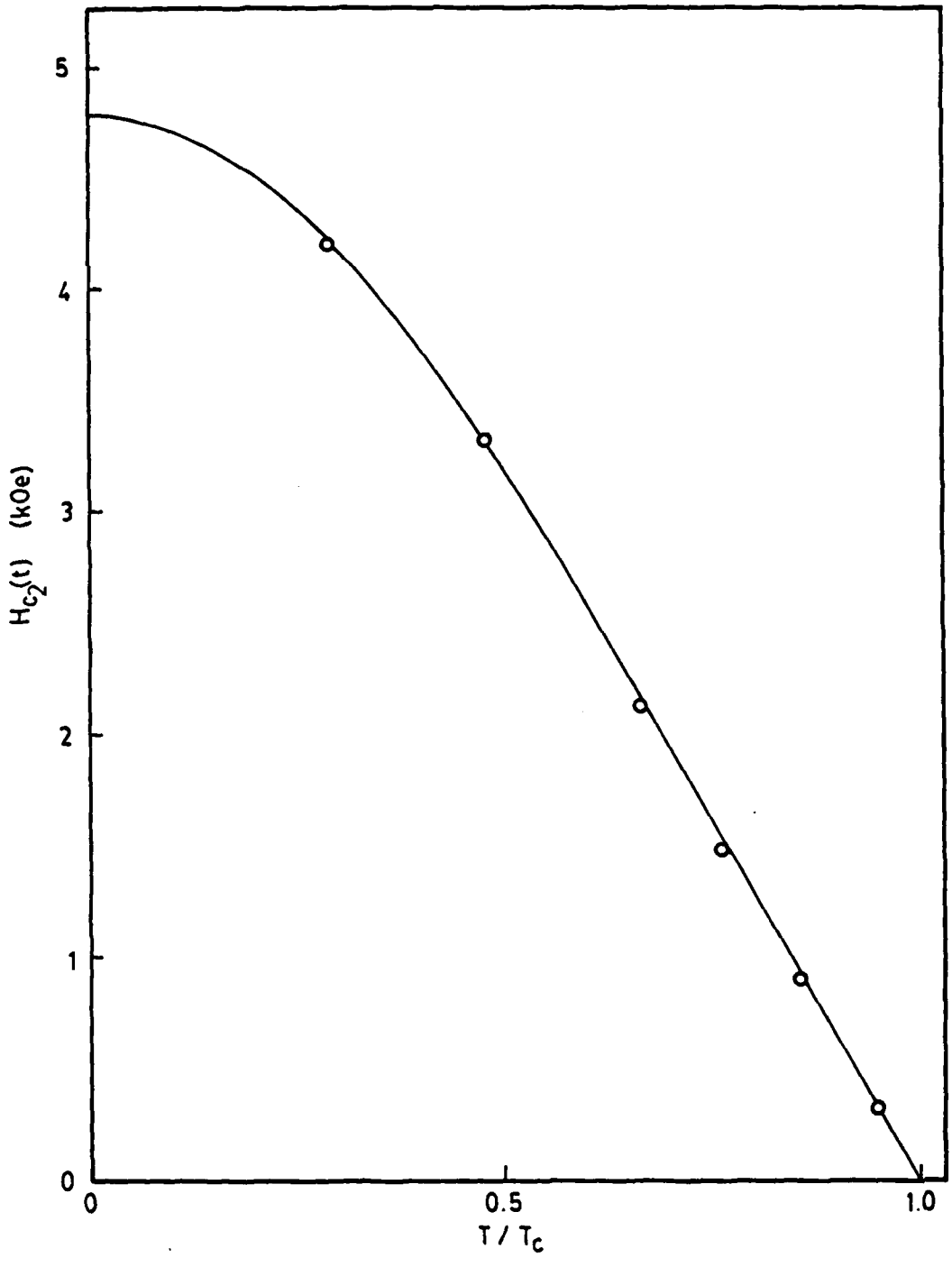

Figure 20) Variation of the critical field H_{c_2} with reduced temperature for specimen #65. The solid line represents Equation (4.14) with $\eta = 0.5$.

averaged for each specimen and expressed as a percentage. The value of ΔH_{c_2}, is lower when Equation (4.13) is used to calculate $H_{c_2}(t)$ than when Equation (4.12) is used, with 3.2% being the average result for the latter and 1.2% for the former.

The values of H_{c_2} for our V - 4.01a/o Nb specimens are higher than the values for pure vanadium and those found by Sirota and Ovseichank [46] for higher concentrations of Nb. This indicates a peak in H_{c_2} for low concentrations of Nb.

From Equations (2.29) and 2.44), a linear relationship can be obtained between the upper critical field, $H_{c_2}(o)$, and the inverse of the electronic mean free path. For infinite mean free path, Equation (2.27) substitutes for Equation (2.29), leading to the intrinsic upper critical field $H_{c_2}(o)$. Equation (4.11) shows that the low temperature resistivity is proportional to the mean free path. A plot of $H_{c_2}(o)$ versus ρ_o should therefore be linear. Figure 21 shows such a plot for our specimens. The relation seems to be linear only for small concentrations of impurities. This leads to an $H_{c_2}(o)$ of 2.70 kOe. Figure 22 shows a plot of $H_{c_2}(o)$ versus $(r_2)^{-1}$. The reason for the increase in the range over which the plot is linear is unclear. This graph intersects the axis at $H_{c_2}(o)$ = 3.12 kOe. Using the computed value of η for each specimen, as opposed to fixing it at η = 0.5, increases the scattering of the data from the straight line in this graph, justifying our decision to fix η.

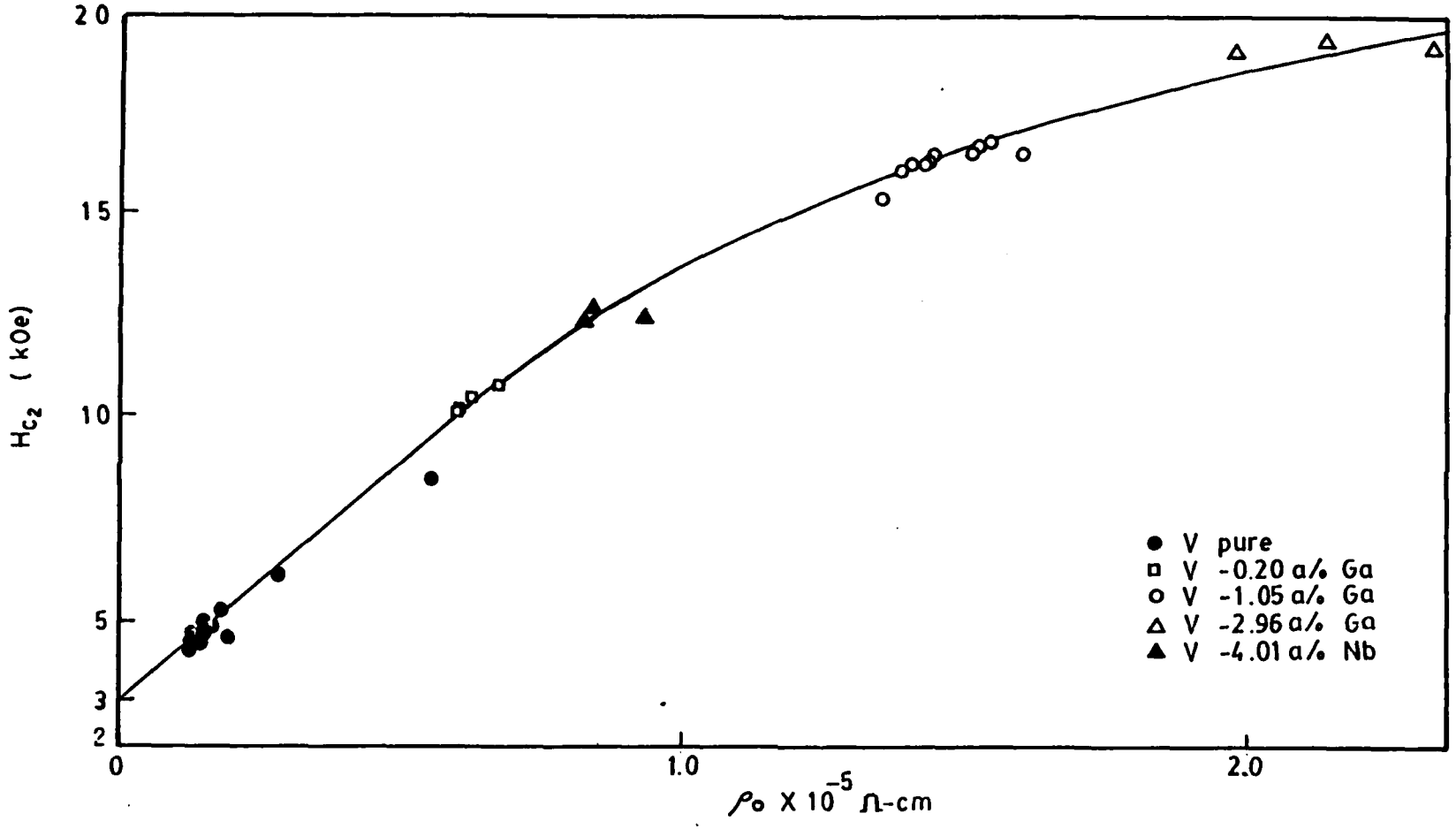

Figure 21) Variation of the critical field, $H_{c_2}(o)$, versus the resistivity ρ_o.

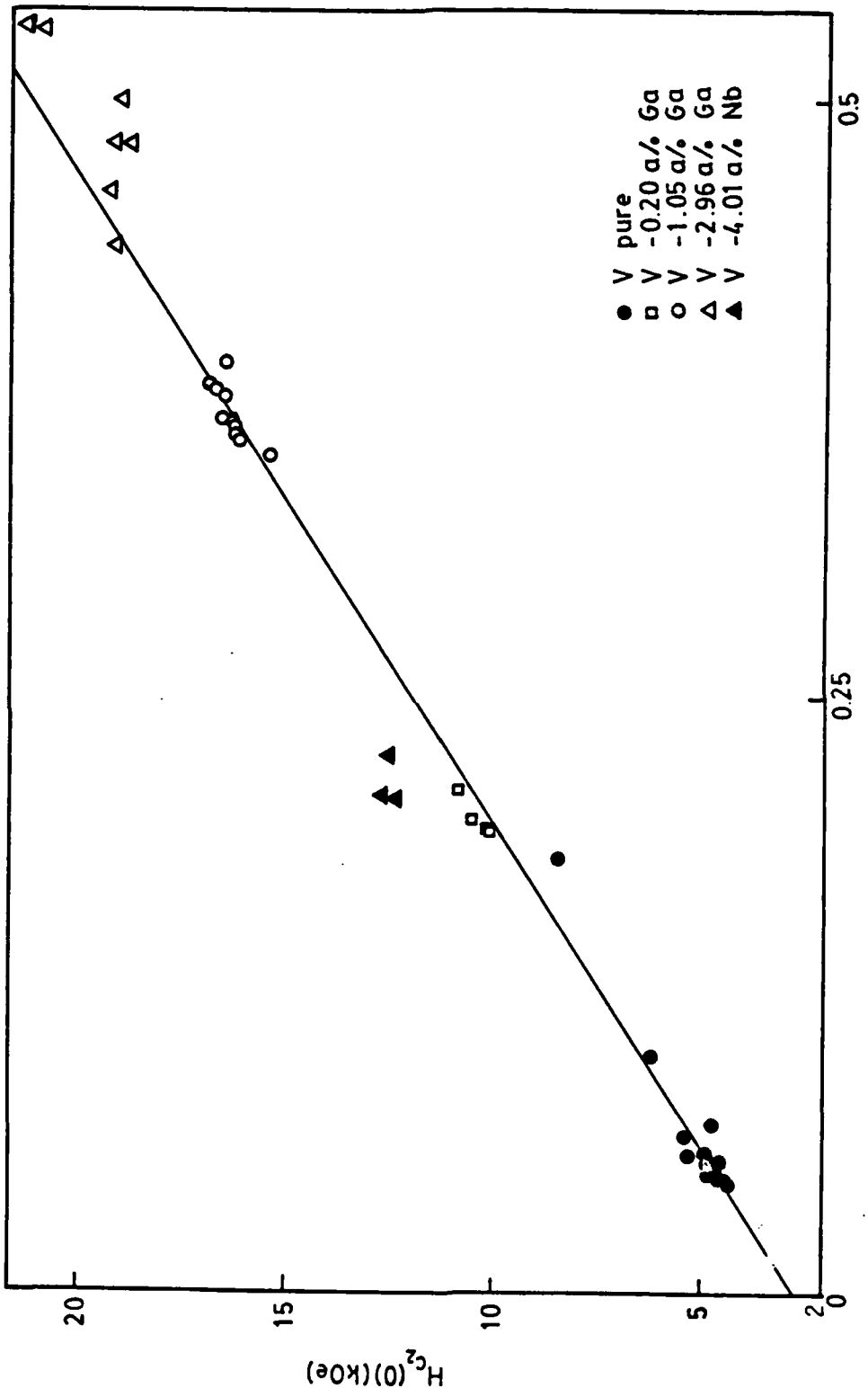

Figure 22) Variation of the critical field $H_{c_2}(o)$ with the inverse of the resistance ratio r_2.

4) Other Superconducting Parameters

The Ginzburg-Landau parameter, κ, is calculated for the specimens in this study by means of Equation (2.34). The London penetration depth at zero temperature, $\lambda_L(o)$, and the Pippard coherence length, ξ_o, are obtained by Radebaugh and Keesom [10] for a pure vanadium specimen with a resistance ratio of 140. They use the equations

$$\lambda_L(o) = \frac{3h\gamma^{1/2}\Pi^{1/2}C}{ek_BS} \tag{4.15}$$

and

$$\xi_o = 1015 \frac{k_BS}{T_{c_o}\alpha} \quad , \tag{4.16}$$

obtaining

$$\lambda_L(o) = 398 \text{ Å} \tag{4.17}$$

and

$$\xi_o = 450 \text{ Å} \quad . \tag{4.18}$$

Here S is the area of the Fermi surface in k-space, h is Planck's constant, and k_B is Boltzmann's constant.

Substituting the values (4.17), (4.18), and Equation (4.11) into the Equations (2.32) and (2.33), κ_o and κ_ℓ become

$$\kappa_o = 0.849 \tag{4.19}$$

and

$$\kappa_\ell = 8.13 \times 10^5 \rho_o \quad . \tag{4.20}$$

Equation (2.34) becomes

$$\kappa = 0.849 + 8.13 \times 10^5 \rho_o \quad , \tag{4.21}$$

where ρ_o is given in ohms-cm. Using the value $\eta = 0.5$ given in the previous section, Equation (2.36) can be expressed as

$$\kappa_1(t) \approx \frac{1.5\kappa}{(1+0.5t^2)} \quad , \tag{4.22}$$

The parameter $\kappa_1(o)$ has a range for the specimens in this study of about 3.0 for pure vanadium, to more than 30.0 for the V - 2.96a/o Ga specimens. The ratio $\kappa_1(o)/\kappa$ obtained from Equation (4.22), namely,

$$\frac{\kappa_1(o)}{\kappa} = 1.5 \tag{4.23}$$

agrees with that obtained by Radebaugh and Keesom [10].

The temperature dependent coherence length, $\xi(t)$, can be calculated from Equation (2.44) as being

$$\xi(t) = \frac{\Phi_o}{2\pi H_{c_2}(t)}^{1/2} \quad . \tag{4.24}$$

The penetration depth $\lambda(t)$ can be calculated, near T_c, from Equation (2.31) as being

$$\lambda(t) = \kappa\xi(t) \quad . \tag{4.25}$$

Values obtained for κ and $\xi(o)$ are listed in Table (4).

Table 4. The Ginzburg-Landau Parameter and the Coherence Length.

Specimen #	K(o)	$\xi(o)$ Å
	pure vanadium specimens	
8		275
50	1.93	N.A.
54	188	268
41	2.15	259
76	2.29	248
77	1.97	268
78	1.82	278
82	2.06	265
83	2.42	265
94	3.12	232
96	2.04	271
70	2.14	260
56	2.24	N.A.
49	4.76	N.A.
68	1.92	265
58	1.94	N.A.
65	1.90	261
35	1.99	N.A.
24	1.92	266
23	$\sim$2.36	244

N.A. Not Available

Table 4. The Ginzburg-Landau Parameter and the Coherence Length (Continued).

Specimen #	K(o)	$\xi(o)$ Å
22		197
19	1.99	264
	V - 0.20a/o Ga	
86	5.75	180
90	5.34	N.A.
93	6.30	174
91	5.69	180
92	5.90	177
	V - 1.05a/o Ga	
30	13.8	141
61	12.1	143
42	13.2	140
43	13.4	140
71	12.3	142
32	13.1	141
60	11.8	146
69	12.5	142
81	12.5	142
84	12.6	141

Table 4. The Ginzburg-Landau Parameter and the Coherence Length (Continued).

Specimen #	K(o)	ξ(o) Å
	V - 2.96a/o Ga	
7	17.8	N.A.
5	38.5	N.A.
63	23.7	126
33	16.9	131
17	19.8	131
44	18.3	131
62	23.9	124
67	23.9	124
9	19.7	132
10	21.2	132
	V - 4.01a/o Nb	
27	7.62	161
28	N.A.	N.A.
29	7.79	N.A.
45	7.57	163
51	8.46	162
52	8.18	N.A.

B) Fluxoid Pinning

1) Critical Currents

The critical currents for each specimen were measured at four to eight temperatures, down to 1.5K. At each temperature, the critical currents were obtained for thirty to fifty successively increased magnetic fields. The fields were increased from zero up to a value just above $H_{c_2}(t)$. For each magnetic field, the transport current was swept up from zero until flux flow was clearly observed. The four-probe method shown in Figure 11 was used to observe the voltage across the specimen. The critical current was taken to be that current at which flux-induced voltage was first observed (see Figure 23).

Fluxoids are strained in the process of changing magnetic fields or of changing transport currents, therefore, critical currents are dependent on the recent magneto-electric history of the specimen [48,49,50,51]. For example, if the desired magnetic field is obtained by increasing it from a lower magnetic field, the critical current can be different from that if the desired field is arrived at from above. The following procedure was used to erase the magneto-electric history from the specimen. The magnetic field was established before each critical-current data point was taken. The specimen was then heated above its critical temperature and allowed to cool. This process created a relaxed flux lattice [49].

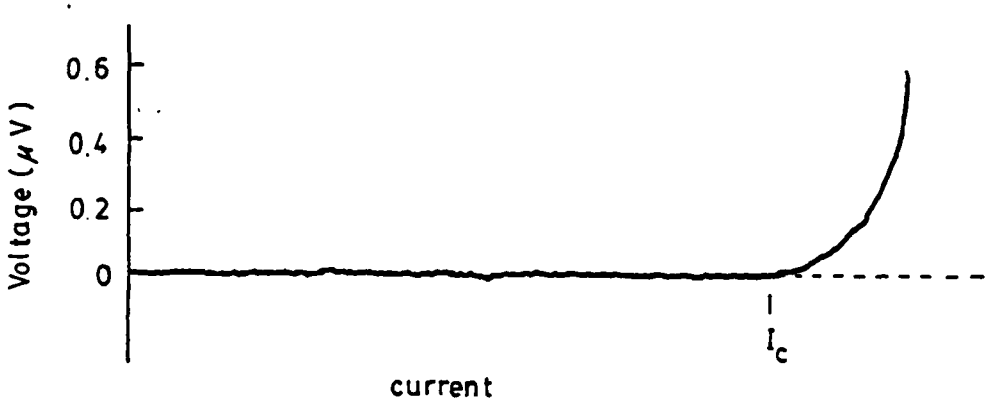

Figure 23) Determination of the critical current, I_c, from the current versus voltage plot.

Several steps were taken to minimize the effect of Joule heating in the specimen/current-lead contact areas. As noted in the previous chapter, the specimen shape was designed with this in mind. The wide end tabs of the specimens provide a large contact surface. The end tabs are ultrasonically tinned with indium and then soldered to the copper current-contacts. This method usually provides a satisfactory current contact [52]. The indium solder flows around both sides of each end tab. The indium solder superconducts at low temperatures and near-zero magnetic fields. Hence, even if there is a vanadium-oxide layer between the vanadium and the solder, the contact surface probably superconducts due to the proximity effect. The normal indium solder provides a different benefit. Normal indium serves as a good heat carrier from the superconducting vanadium, which has very poor thermal conductivity, to the copper block halves (see Figure 11). The copper block halves come in direct contact with the tinned end tabs. Dow-Corning-200 fluid of 60,000 centistokes is used to enhance the thermal contact. Other precautions taken were: superconducting Nb_3Sn current lead-in wires with a thick copper cladding to dissipate excess heat; a small cross-sectional area in the center of the specimen to minimize the current needed for a given current density; and massive copper current-contacts to enhance thermal conduction and dissipation.

The effect of the current-contact Joule heating was monitored in several ways. Direct checks were routinely made by observing

the specimen-block temperature rise due to this heating. For this check, the specimen-block heater (Figure 11) was turned off, and the specimen-block was allowed to cool to the helium-bath temperature. The transport current was then slowly increased to a value above I_c, while recording from the germanium thermometer the increase, if any, in temperature. At low temperatures and near-zero magnetic fields, the indium solder superconducted. In this case, usually there was no sign of heating at currents below the critical current of the specimen. In the case where the indium solder was normal, there was a rise in the specimen-block temperature usually of less than 0.04K at 20A, the maximum transport current available. This temperature rise was easily handled by the copper-block temperature-control system under normal working conditions.

The copper-block temperature control system itself provided another check. A decrease in heater current at the higher transport-current levels was an indication that the balance of the heat needed to maintain the specimen-block temperature was being supplied by the Joule heating of the current contacts.

Finally, the critical current provided another check. Joule heating in the contact area can sometimes precipitate a quench in the superconductivity of that area. This quench propagates through the superconductor appearing as an abrupt and irreversible increase in voltage in the V-I plot, accompanied, and often preceded by, a sudden increase in block temperature. Although

some of our specimens showed sudden increases in voltage in the V-I curves, there are several indications that these were not caused by quenches in the contact area. First, the sharp increase in voltage could usually be stopped once it started. This was easily done by freezing the magnitude of the transport current at a value just above I_c. A decrease in the magnitude of the transport current would then cause the voltage across the specimen to decrease smoothly to zero. Second, the sharp increase in voltage was not preceded by a sudden increase in the specimen-block temperature. Finally, these sharp increases in voltage appeared at specific reduced-magnetic-field regions, where the critical current was increasing with increased magnetic field. At higher reduced fields, critical currents of larger magnitude were usually observed without the abrupt voltage increase. This phenomena will be discussed in later sections.

Figures 24-27 show the critical current density versus the reduced field for many of the specimens, grouped by alloy and carbon concentration. A temperature near $0.6T_c$ is used for each figure. Several general observations can be made from these figures. The specimens with no precipitates exhibit very low critical current densities as expected. Crystal dislocations, caused by cold rolling the material, increase the magnitude of J_c. This increase is not as high as the one brought about by the vanadium-carbide precipitates. Specimens with large precipitates

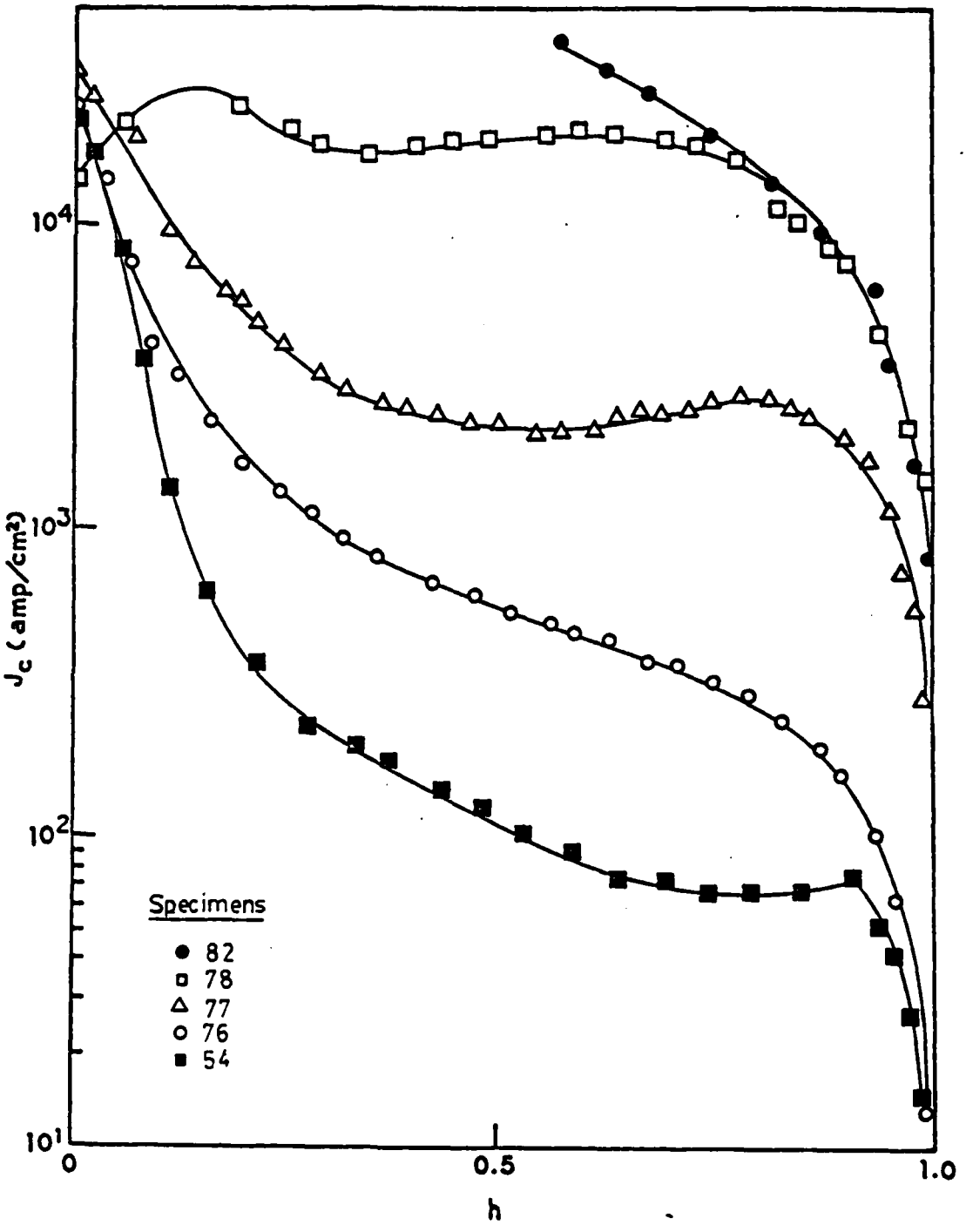

Figure 24) Semi-log plot of the critical current density versus reduced field, at T = 3.5K, for the vanadium specimens with 0.07%C.

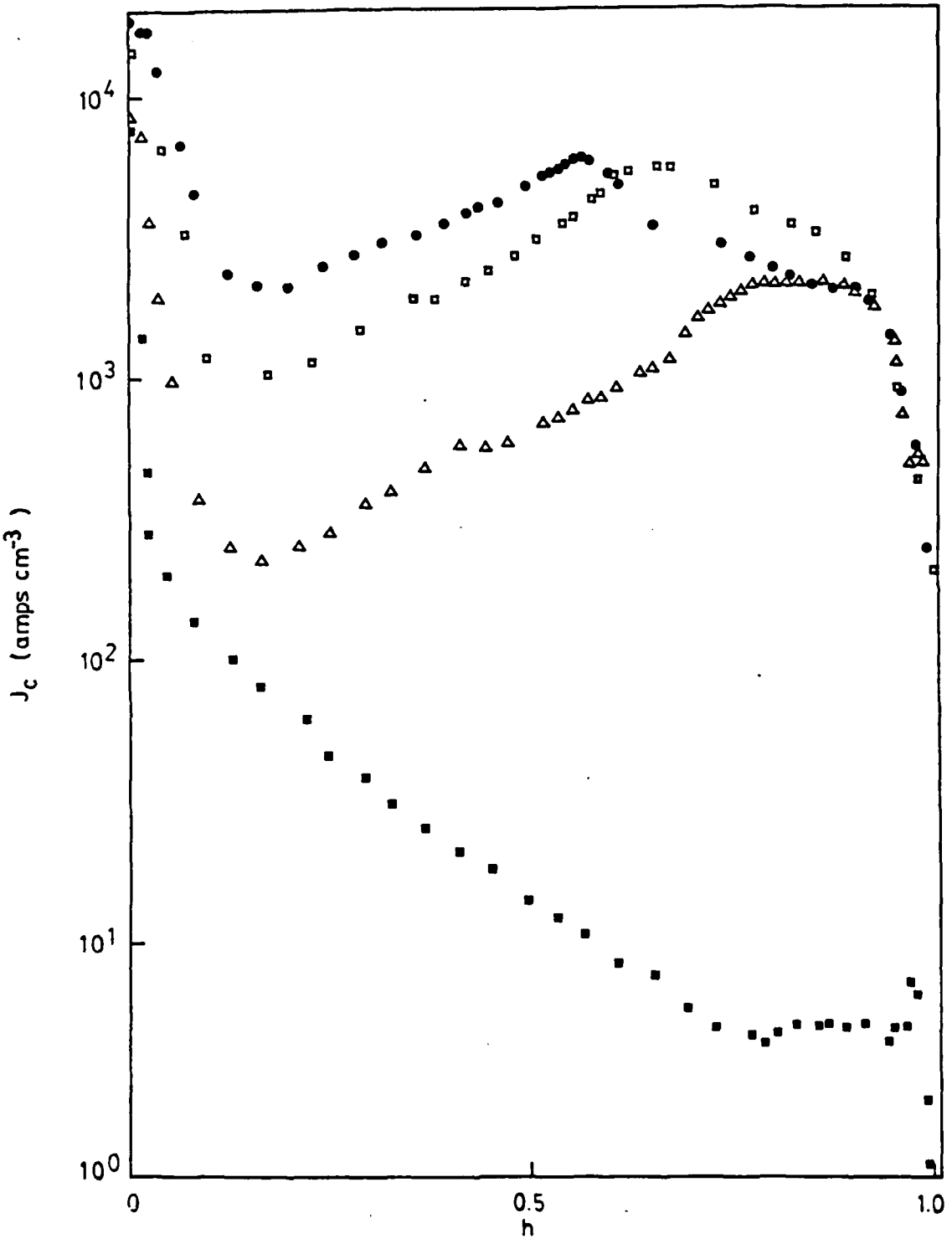

Figure 25) Semi-log plot of the critical current density versus reduced field, at T - 3.0K, for the V - 0.20a/o Ga specimens.

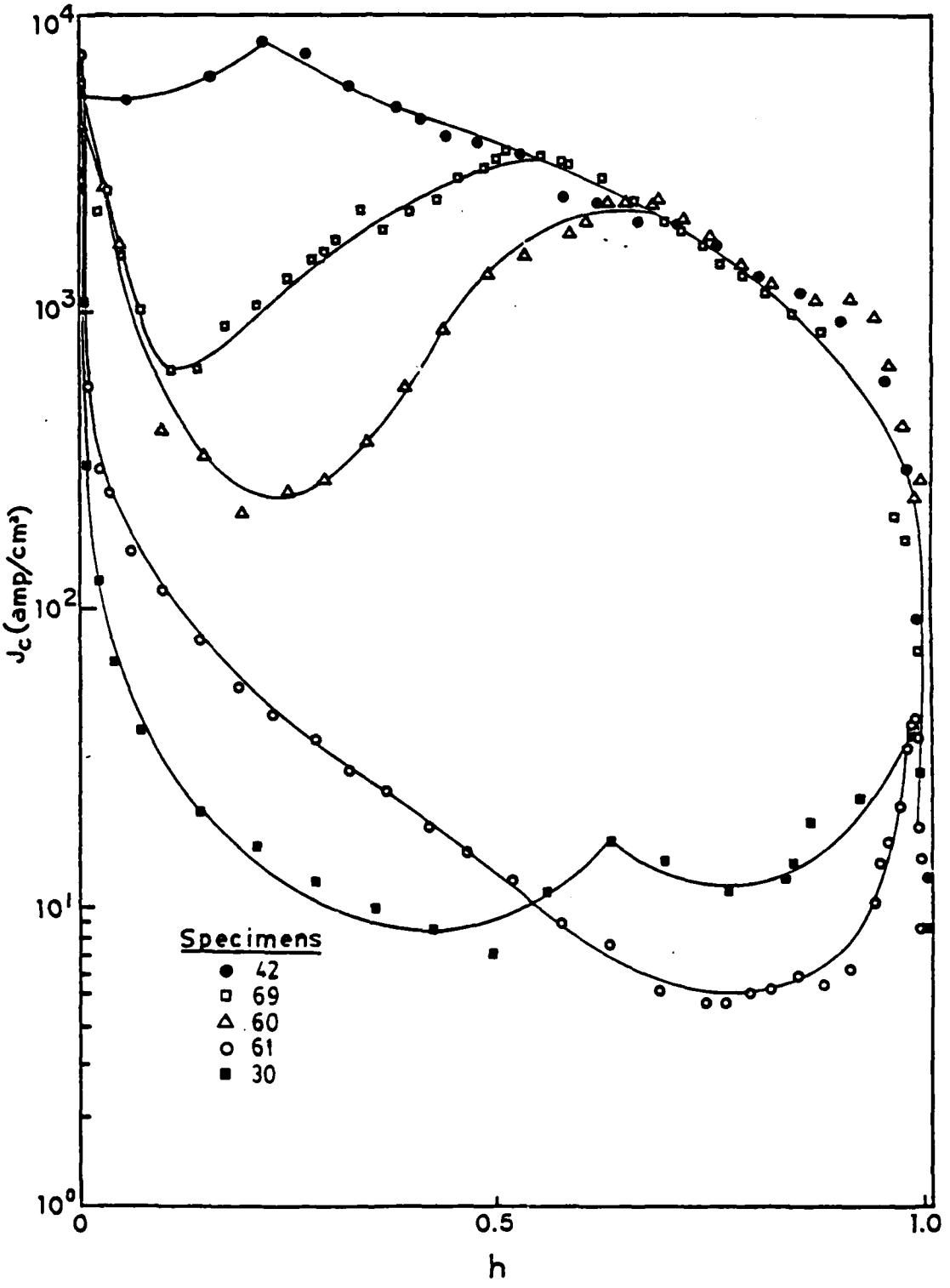

Figure 26) Semi-log plot of the critical current density versus reduced field, at T = 2.5K, for the V - 1.05a/o Ga with small precipitates.

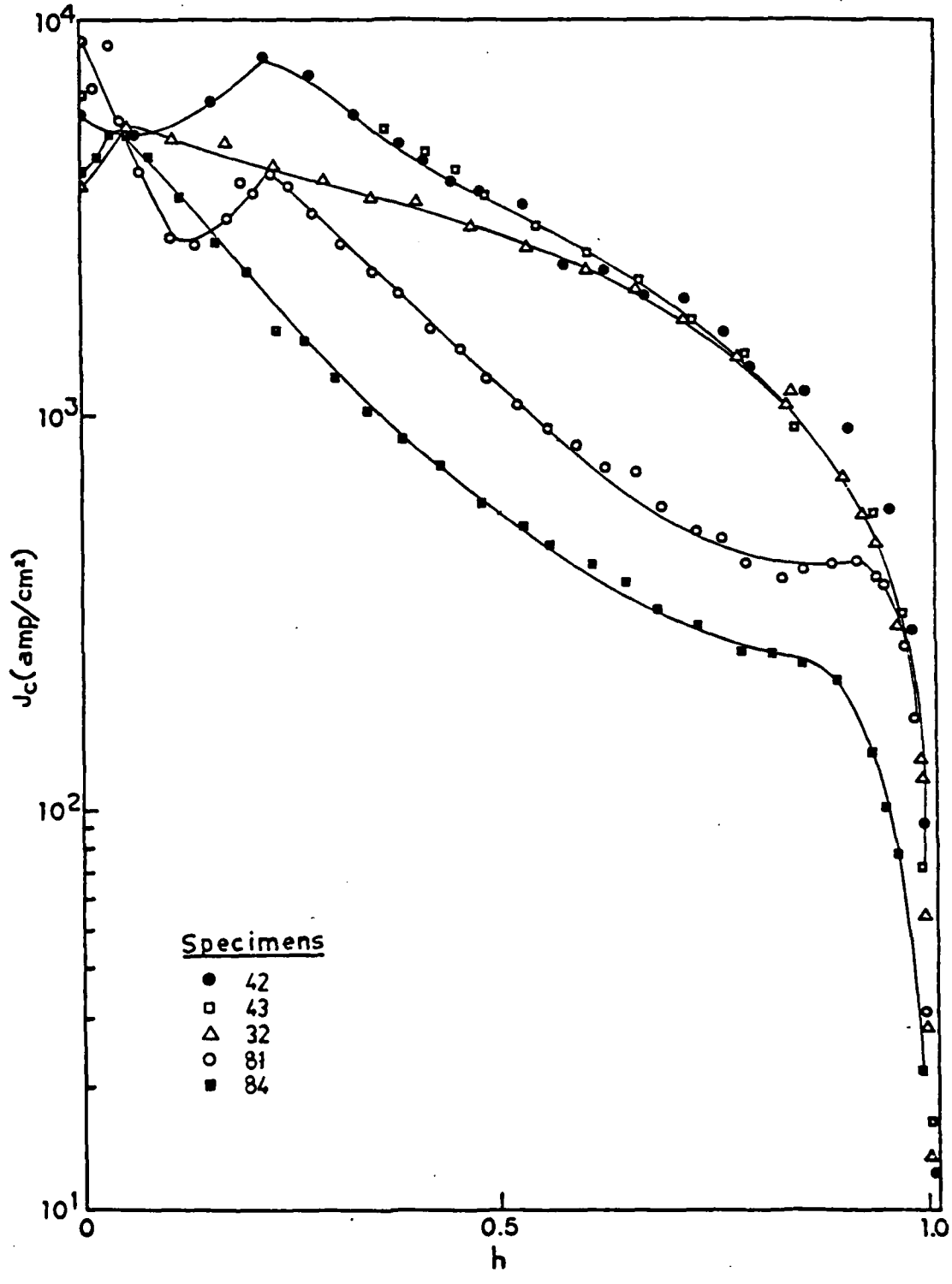

Figure 27) Semi-log plot of the critical current density versus reduced field, at T = 2.5K, for the V - 1.05a/o Ga with large precipitates.

exhibit higher values of J_c than those with smaller precipitates. However, several specimens with very large precipitates actually exhibit lower values of J_c than the values for specimens with comparatively smaller precipitates. The peak effect near H_{c_2} is evident in specimens with no carbon or very small sized precipitates.

2) Carburized Specimens

a) General Observations on the Form of the Pinning Force

Our specimens exhibit four distinct forms for the pinning force density. Each form appears at a definite reduced-magnetic-field region. An individual specimen may show two, three, or all of these regions. The appearance of a given reduced-field region in an individual specimen depends on the microstructure of the specimen. There is a strong similarity between some of these regions and Kramer's line-pinning and plastic regions [1]. For convenience, we will name these regions following Kramer.

Several specimens show a sharp decrease in J_c as the reduced field is increased from zero, leveling off at higher fields. This effect is more evident in the specimens with small-sized or no precipitates. This reduced-field region can be called the point-pinning region. This region usually exhibits very low critical currents. Hence, no attempt was made to thoroughly analyze this region. At a certain reduced field, the critical current starts to increase with increasing field. This is the line-pinning region. At fields near H_{c_2}, the current decreases as $(1-h)^2$. This reduced-field region, called the plastic-deformation region, is the one

region shared by all specimens. Between this high-reduced-field region and the line-pinning region, many specimens show a fourth region. In some specimens, this region occupies most of the reduced-field range. There is no equivalent for this region in Kramer's theory. For lack of a better name, we will call this region the transition region.

The boundary between each region is usually clearly defined, as shown in Figure 28. A sharp discontinuity in the reduced-field dependence of the pinning force is often observed in the boundary between any two regions. There is usually an abrupt change in the magnitude of the pinning force in the point-pinning/line-pinning boundary.

The character of the fluxoid-induced voltage at J_c varies from one region to another. In the line pinning region, the alloyed specimens often exhibit an abrupt increase in voltage at J_c, as seen in Figure 29. This effect was mentioned in the previous section. The point-pinning, transition, and plastic-deformation regions show a slow increase in voltage at J_c.

The pinning force density in the line-pinning region of the alloyed specimens is also dependent on the magneto-electric history of the specimen. Several runs were made where the critical current was obtained in the usual way, that is, the specimen was heated in the magnetic field up to a temperature above its T_c and allowed to cool before measuring I_c. Then, the transport current was decreased to zero and, without reheating the specimen to above T_c, the current was increased to obtain a new I_c for that field.

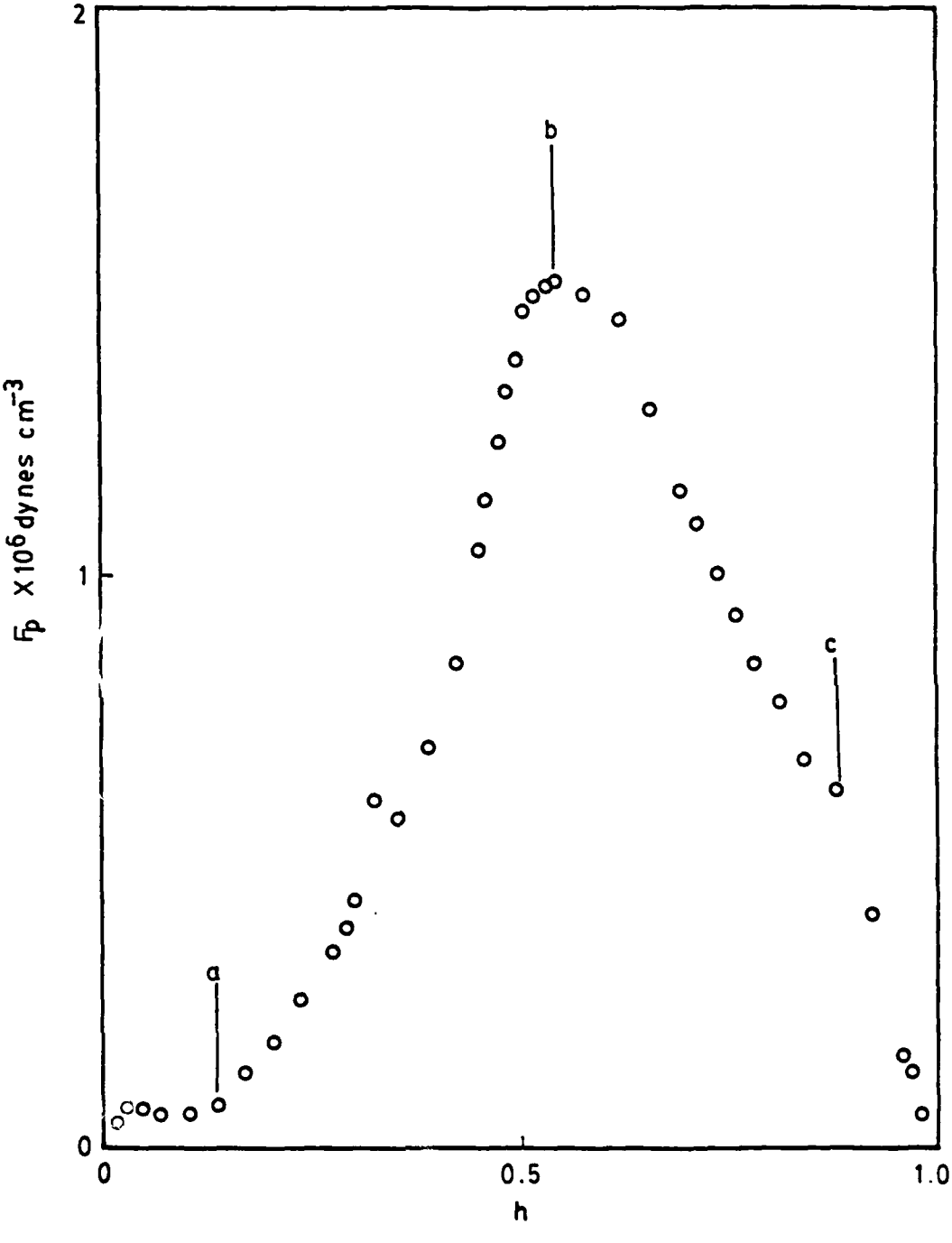

Figure 28) Pinning force density, F_p, of specimen #69 at T = 2.5K, versus the reduced field, h. The vertical lines indicate the start of a) the line-pinning region, b) the transition region, and c) the plastic-deformation region.

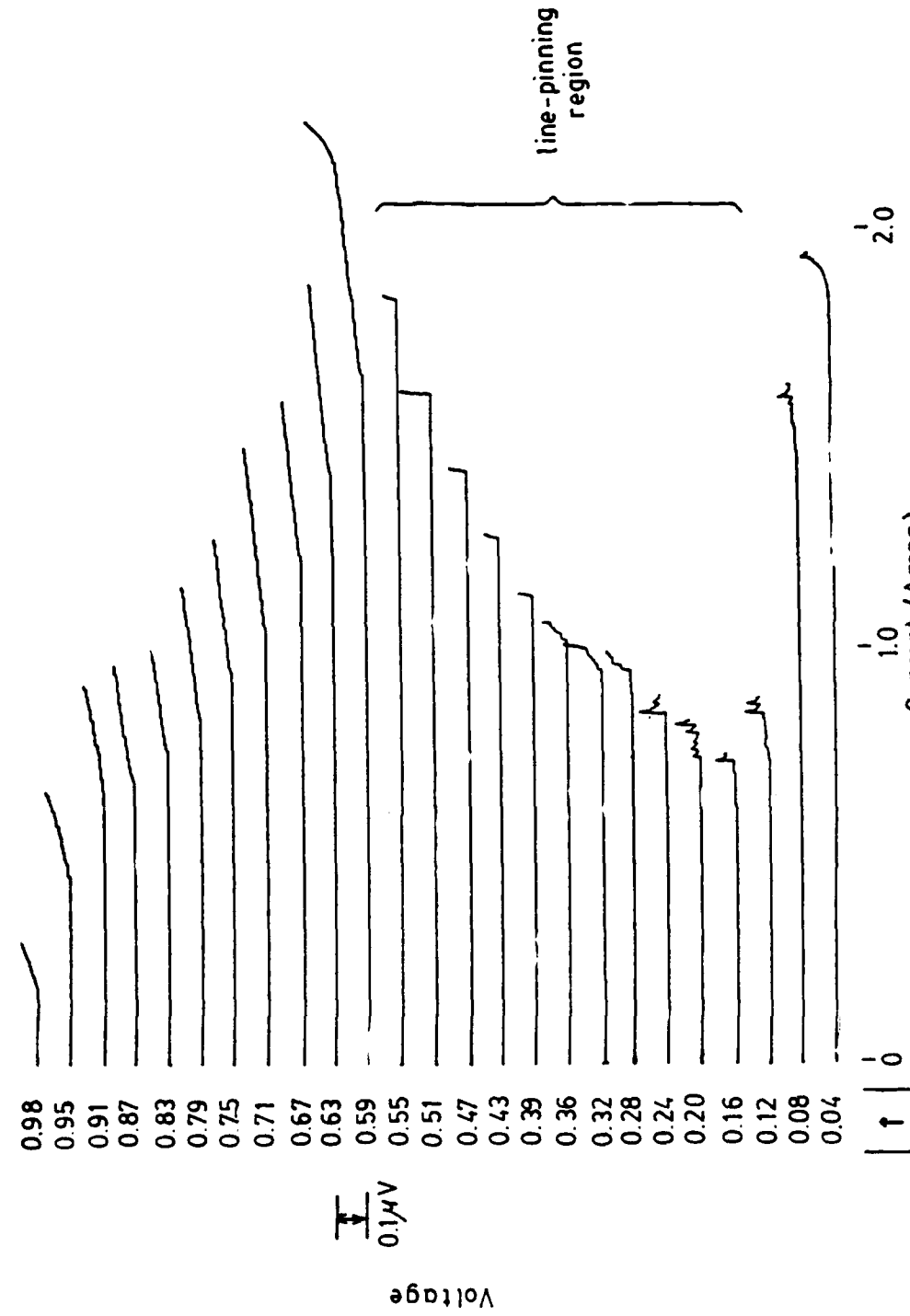

Figure 29) Voltage versus current plots of specimen #92 at 3.5K for different magnetic fields. The brace indicates the range of the line-pinning region.

This procedure of repeatedly raising the current up to I_c is called training. In the line pinning region, the value of the trained critical current was usually lower than that of the original I_c. This training effect was not observed in the other reduced-field regions. In these regions, the same critical current was always observed independently of the magneto-electric history.

Finally, as it is shown in the next sections, the dependence on temperature and microstructure differs from region to region.

Several assumptions are made in order to obtain a dependence of the pinning force density on temperature, reduced magnetic field, and microstructure. These assumptions are based on the generally accepted idea of a scaling law [4] and on several traits common to most theoretical forms of the pinning force density. We assume that the temperature dependence can be described by $H_{c_2}^n(T)$, where n is rounded off to the nearest half-integer. We also assume that the dependence on the Ginzburg-Landau parameter, κ_1, is given by κ_1^m. Again, for simplicity the parameter m is rounded off to the nearest half-integer. Therefore, the pinning force density, F_p, can be described by

$$F_p = q \frac{H_{c_2}^n(T)}{\kappa_1^m(o)} f(h)g(\text{microstructure}) \quad , \tag{4.26}$$

where f(h) is a form factor describing the reduced-field dependence, and g(microstructure) describes the dependence on the microstructure

of each specimen. The parameter q is a constant for all specimens. The form of this equation changes for each of the reduced field regions.

b) Line Pinning Region

Only the specimens with the smaller sized precipitates show a line pinning region. This region is characterized by an increase in the critical current density as the reduced field is increased. Kramer used a simple approximation of the interaction force where $f_p \propto (1-h)$ [1], obtaining for the pinning force density a form factor given by

$$f(h) = \frac{h^{1/2}}{(1-h)^2} \quad . \tag{4.27}$$

This form factor basically agrees with our data. Our specimens show a form factor given by

$$f(h) = \frac{h^{1/2}}{(1-h)^2} + b \quad , \tag{4.28}$$

as seen in Figure 30. This form factor has been observed elsewhere [53]. The constant b is usually negligible.

The reduced field h_L, at which the line pinning first appears, is usually easy to recognize from the abrupt change in the character of the pinning force curve. The boundary between the line pinning region and the transition region is sometimes smooth. With a smooth boundary, the upper bound of the line pinning region is a somewhat subjective choice. For the specimens without a transition region, the boundary between the line pinning region and the plastic

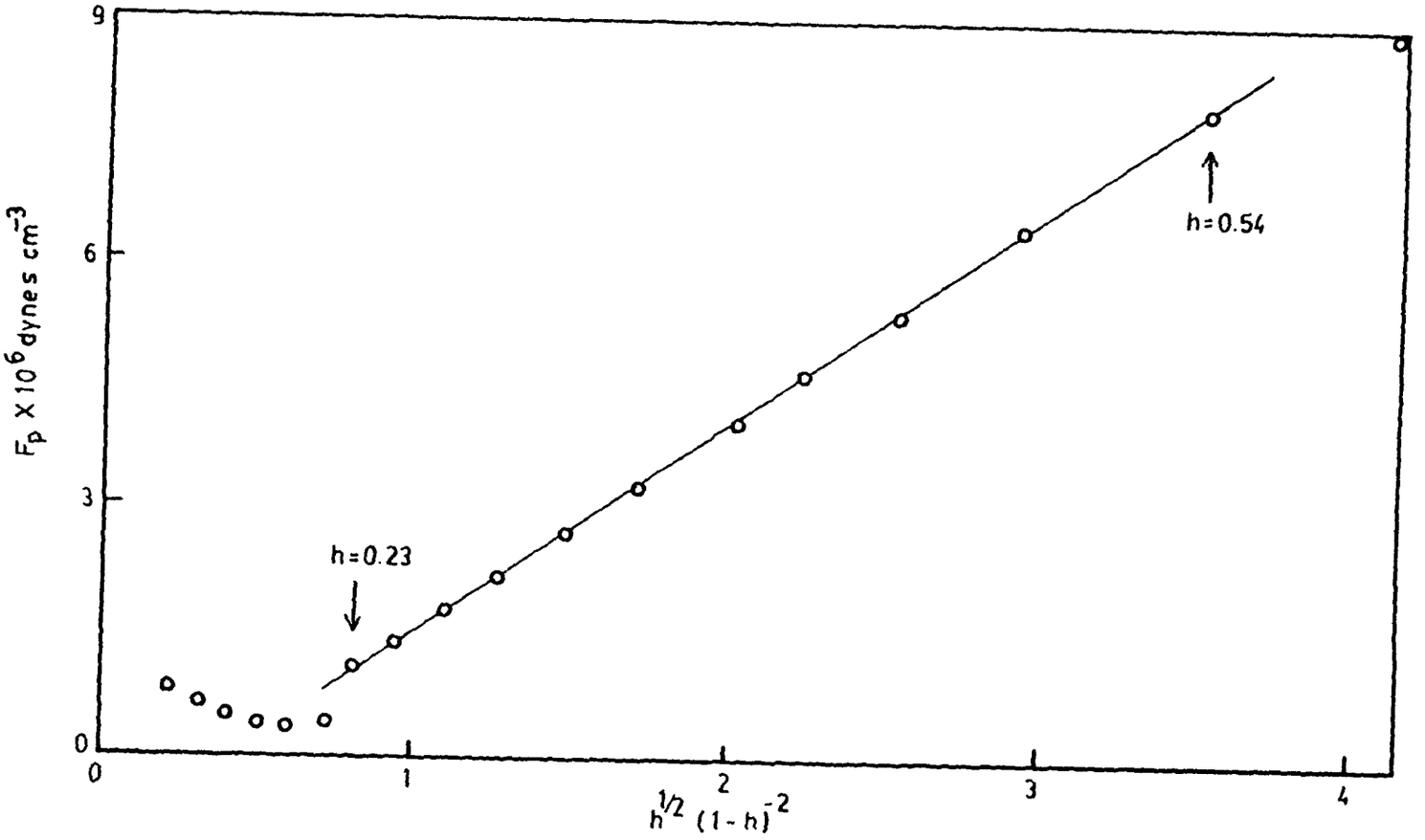

Figure 30) Pinning force density versus $h^{1/2}(1-h)^{-2}$ of specimen #93 at 1.5K. The arrows indicate the limits of the line-pinning region.

deformation region is very sharp. In either case, the range of the line pinning region is usually aboue one third of the total reduced field range from zero to $H_{c_2}(T)$.

The parameter C_1 is defined by the equation

$$F_p = C_1 \frac{h^{1/2}}{(1-h)^2} \quad . \tag{4.29}$$

This parameter contains the temperature, microstructure, and κ dependence of the pinning force density of a specimen. The value of this parameter is obtained for each temperature from a least mean square fit of the data to Equation (4.29).

The temperature dependence of C_1, given by $H^n_{c_2}(t)$, is obtained from a least-mean square fit of the data to the equation

$$\ln[C_1(t)] = n \ln[H_{c_2}(t)] + K_1 \quad , \tag{4.30}$$

where K_1 is dependent on the microstructure and on the G.L. parameter, κ_1. The average value of n is 4.2, with a standard deviation of 0.9. (see Table 5). The pinning force density can now be expressed as

$$F_p = K_1 H^4_{c_2}(t) h^{1/2} (1-h)^{-2} \quad . \tag{4.31}$$

Small variations of n create large variations in K_1. Therefore to minimize errors, K_1' is calculated for each specimen using the average n rounded up to the nearest half-integer $n = 4.0$. The parameter K_1' is calculated for each temperature from

$$K_1' = \frac{C_1(T)}{H^4_{c_2}(T)} \quad , \tag{4.32}$$

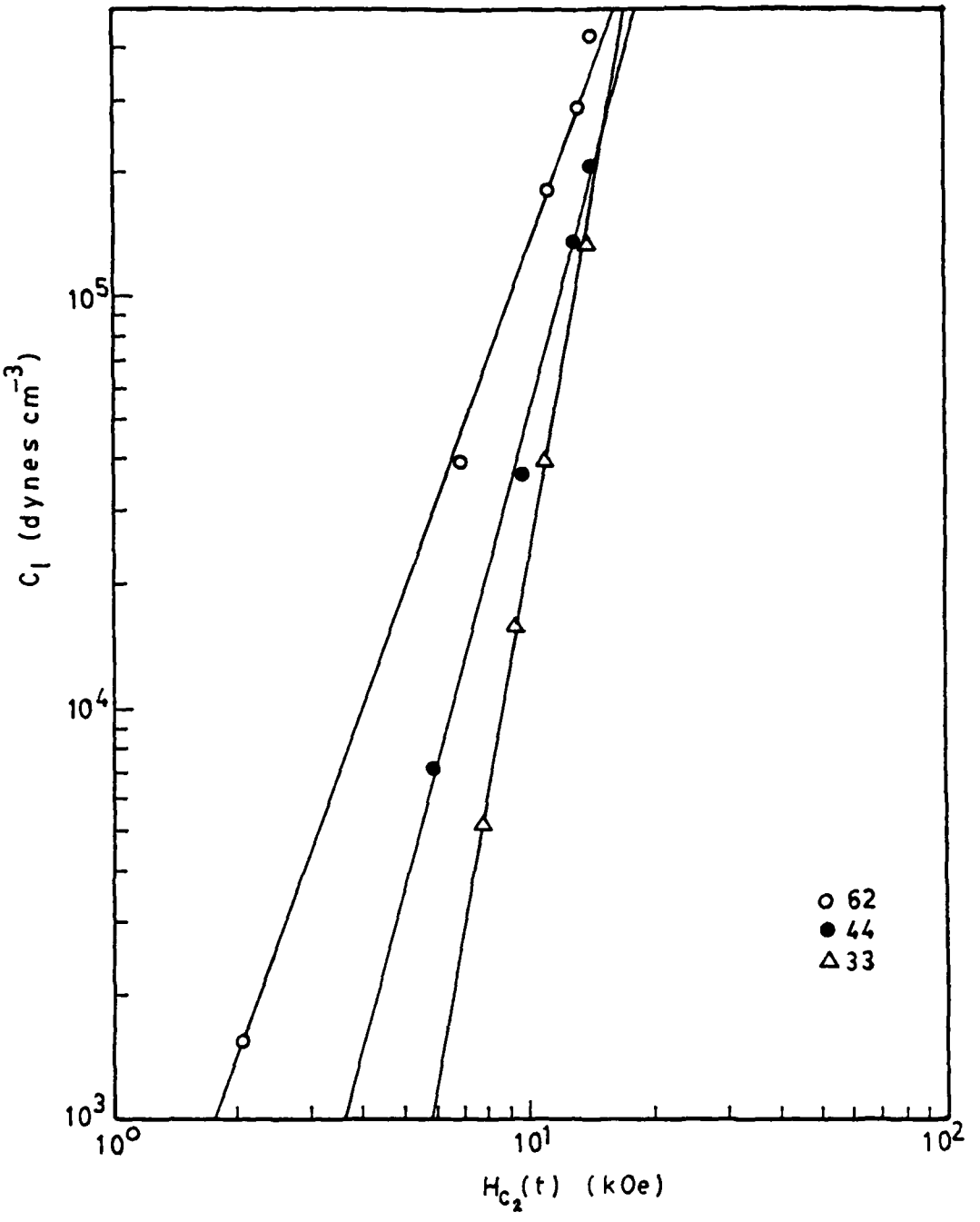

Figure 31) Log-log plot of the parameter C_1 versus the critical field $H_{c_2}(t)$ for the specimens #62, #44, and #33.

Table 5. Pinning Force Density Parameters (Continued).

Specimen #	Line-Pinning Region		Transition Region		Plastic Deformation Region	
	n	$k_1'\kappa_1^{2.5}$ X 10^{-8}	n	$K_a\kappa_1^2$	n	$k_p k^2$
			V - 0.2a/o Ga			
93	4.9	9.4	-	N.E.	1.8	7.0
91	4.2	31		N.A.	2.4	5.4
92	3.7	44	2.0	0.170	2.1	14
			V - 1.05a/o Ga			
42	3.8	236	2.5	0.140	2.8	27
43	-	N.E.	2.7	0.131	3.2	12
71	3.5	42	3.0	0.177	2.0	9.0
32	-	N.E.	2.7	0.134	2.0	12-
60	4.6	6.5	2.4	0.122	2.2	5.6
69	4.2	19	2.9	0.132	2.9	3.6
81	3.7	102	2.0	0.034	1.9	20
84			2.6	0.016	2.9	1.0
			V - 2.96a/o Ga			
33	5.9	0.70	-	N.E.	1.4	13
17		N.A.	3.0	0.276	5.0	18-
44	3.9	20	2.7	0.206	2.5	9.0
62	3.2	9.3	2.6	0.133	3.0	3.8
67	3.6	1.2	3.1	0.173	1.8	3.6
			V - 4.01a/o Ga			
45	5.4	11	-	N.A.	2.9	4.7
51	5.0	18	3.0	0.206	2.8	5.2

Table 5. Pinning Force Density Parameters.

Specimen #	line-Pinning Region		Transition Region		Plastic Deformation Region	
	n	$k_1'\kappa_1^{2.5}$ x 10^{-8}	n	K_v	n	$k_p k^2$
			pure vanadium			
77	5.4	4.0		N.E.	3.2	2.0
78	5.0	34		N.A.	1.6	2.7
82	3.2	245	1.9	3.1	1.1	4.1
83	2.6	846	2.8	1.3	2.4	2.3
94	4.2	257	1.7	2.9	1.4	3.4
96	-	N.E.	2.2	3.1	2.4	2.7
70	-	N.E.	2.0	2.1	1.6	1.8
56	-	N.E.	N.A.	0.48	-	N.A.
68	-	N.E.	2.3	0.57	1.8	.93
65	-	N.E.	2.2	2.7	1.9	1.5
19	-	N.E.	2.0	1.95	1.7	5.4

N.A. Not Available

N.E. Does not show this region

Since K_1' is temperature independent, it is then averaged for all temperatures. Temperatures within 9% of T_c are not used because the value of K_1' obtained from them is usually more than two standard deviations away from the mean K_1' for the specimen. This large deviation probably results from the several approximations used to get to this stage, namely, $n = 0.5$, $F_p \propto H_{c_2}^n(T)$, and from the uncertainty in defining T_c within the observed ΔT_c.

The dependence of the pinning force density on the microstructure, of each specimen is contained in the parameter K_1'. The line-pinning-force density predicted by Kramer (Equation 2.91) contains a dependence on the average volume of a precipitate to the fourth power, V^4. The parameter K_1' was plotted for each alloy concentration against the product of V^4 times the density of precipitates raised to various powers. Of these combinations, the product $V^4\rho^2$ given the best fit to a straight line. The V - 2.96a/o Ga and the V - 4.01% Nb specimens give a very poor fit to this relation.

Most of the other pinning theories predict a dependence of F_p on the density of precipitates times a function of the precipitate dimensions. Hence, the parameter K_1' was also plotted for each alloy concentration against the product of ρ times the volume raised to various powers. Of these plots, the combination

$$K_1' \propto V^3\rho \tag{4.33}$$

gives the best fit to a straight line. This fit is slightly better than the one obtained using $V^4\rho^2$. The plot of K_1' versus $V^3\rho$ is shown for several alloy concentrations in Figure 32. The pinning force density now can be expressed by

$$F_p = D_1 V^3 \rho \frac{H_{c_2}^4 h^{1/2}}{(1-h)^2} \quad , \tag{4.34}$$

where the parameter D_1 is dependent on the Ginzburg-Landau parameter k_1.

The fact that a fit of K_1' can be found for both $V^4\rho^2$ and $V^3\rho$ is understandable. The product $V\rho$ is the total volume per cubic centimeter of the vanadium-carbide in the specimens. This product reflects the concentration of carbon introduced in the specimen. Several concentrations, varying from 0.07 to 0.4, were used, as shown in Table 1. For specimens with the same concentration of carbon and negligible amount of carbon in solid solution, ρV is a constant (again, see Table 1). For each alloy concentration, the specimens that show a line-pinning region have the same carbon concentration. The product $V\rho$ is therefore a constant for each alloy concentration. The product $V^3\rho$ can be multiplied by this "constant," $V\rho$, yielding $V^4\rho^2$.

The parameter D_1, defined by Equation (4.34), can be obtained for each alloy concentration if the specimens in the group have approximately equal values of κ_1. This is done by using the relation

$$D_1 = \frac{\Sigma K_1'}{\Sigma V^3 \rho} \tag{4.35}$$

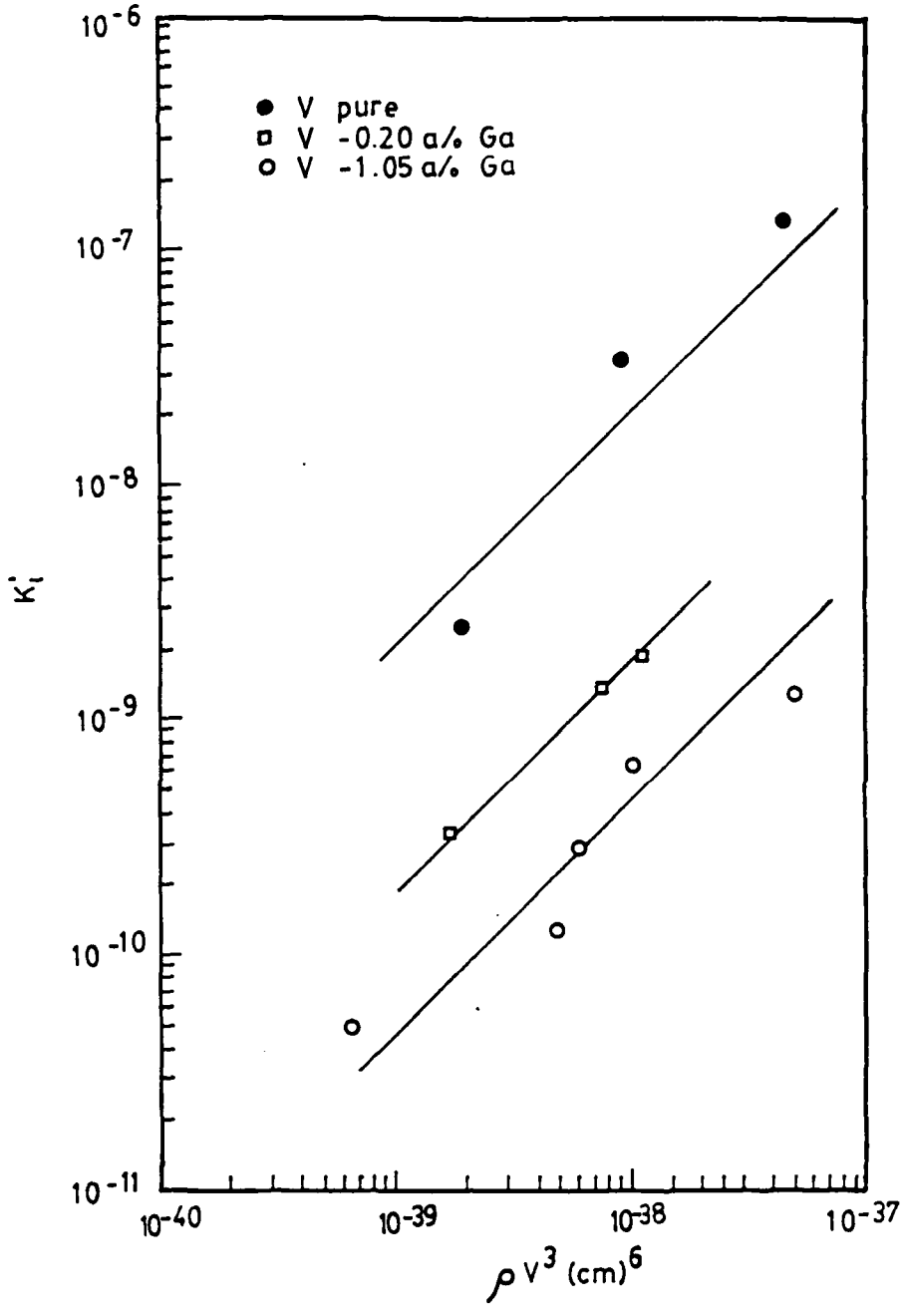

Figure 32) Variation of the parameter K_1' versus $V^3\rho$ for various alloy concentrations. The straight lines show the relationship $K_1' \propto V^3\rho$ for each alloy concentration.

summed over all specimens of an alloy concentration. The dependence of this parameter on κ_1 can be obtained from a least mean square fit of log D_1 versus log κ_1. Figure 33 shows such a plot, which yields.

$$D_1 \propto \kappa_1^{2.37}(o) \tag{4.36}$$

The exponent of κ_1 can be rounded off to the nearest half-integer, i.e., 2.5.

The pinning force density now is given by

$$F_p = q_1 \rho V^3 \frac{H_{c_2}^4(T)}{\kappa_1^{2.5}(o)} \frac{h^{1/2}}{(1-h)^2} \quad . \tag{4.37}$$

The value of q_1 is a constant for all specimens. This value is obtained from the equation

$$q_1 = \frac{\Sigma(K_1' \kappa_1^{2.5}(o))}{\Sigma(V^3 \rho)} \quad , \tag{4.38}$$

summed over all the specimens. The result of this equation is $q_1 = 5.3 \times 10^{31}$, with a standard deviation of 2.9×10^{31}. The fit of the specimens to this equation is illustrated in Figure 34.

There are several sources of error in the calculations of the pinning force parameters C, K, D, and q. The biggest source of error is the uncertainty in the cross-sectional area of the specimen, ΔA. The cross-sectional area is used to calculate the pinning force density. Equation (4.5) shows that there is an

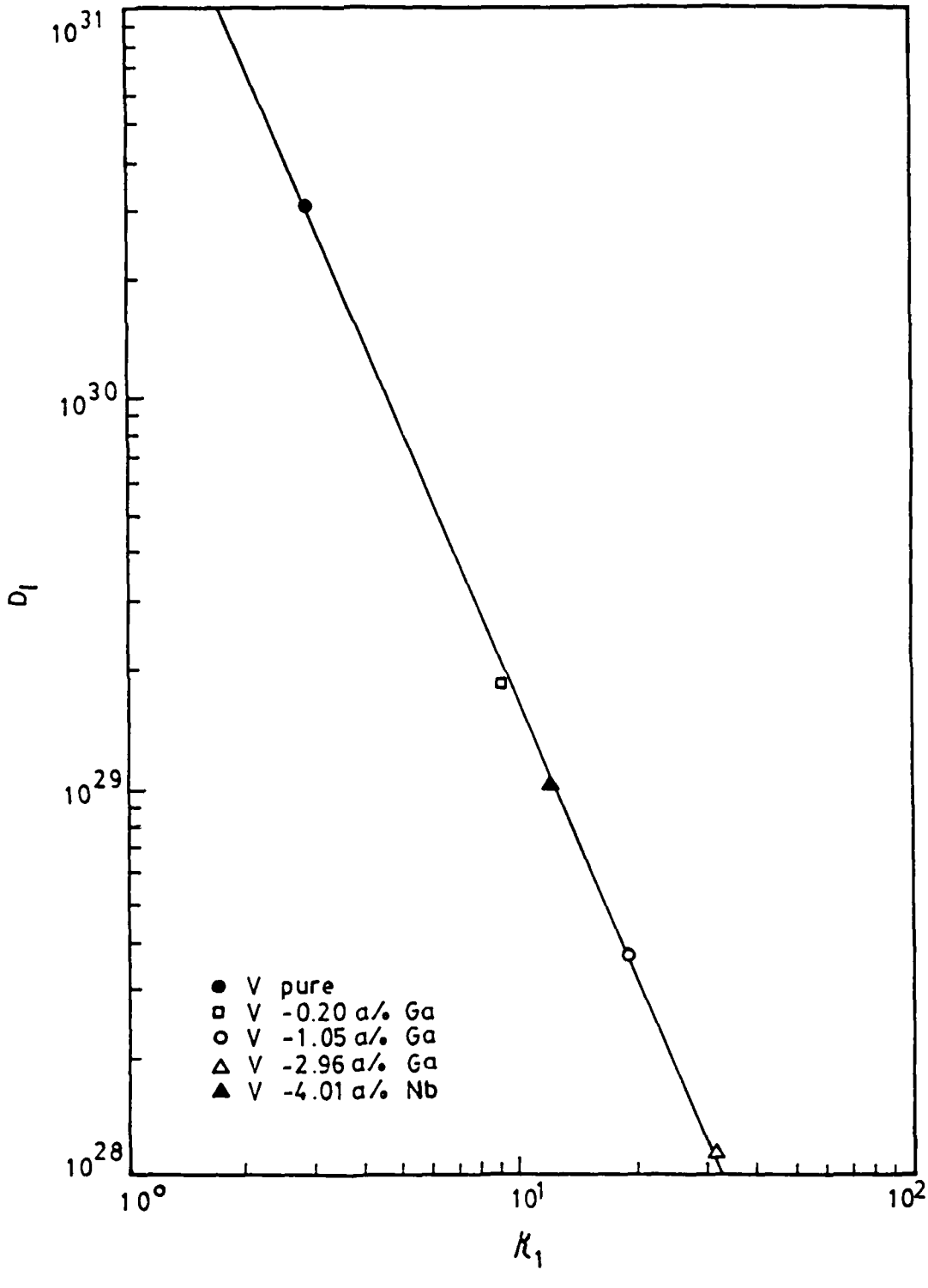

Figure 33) Log-log plot of D_l versus K_1 for the various alloy concentrations. The slope of the straight line is equal to -2.37.

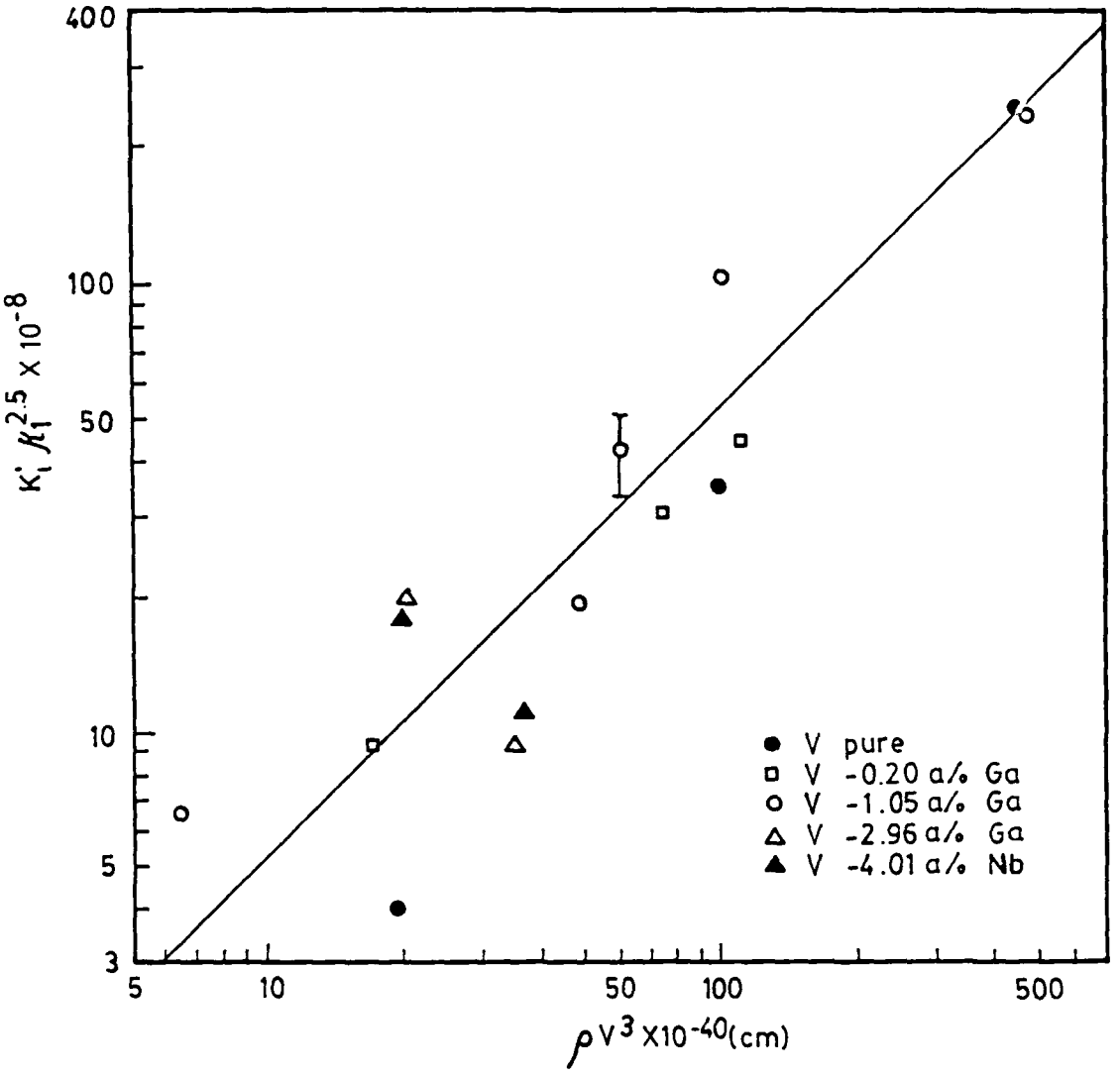

Figure 34) Log-log plot of the product $K_p' K_1^{2.5}$ versus $V^3\rho$ for most of the specimens. The straight line is given by $q_1 = 5.3 \times 10^{31}$.

uncertainty of nearly 15% in the resistivity. Most of this error is due to ΔA. The uncertainty ΔH_{c_2}, listed in Table 3, provides an approximate value of the precision of $H_{c_2}(T)$. The average value of ΔH_{c_2} is 1.2%. There is also uncertainty in obtaining the values for the critical current from the I-V curve (see Figure 23). This error is larger for the plastic deformation region, where the voltage increases imperceptibly from zero at I_c. In the line-pinning region and in the transition region, the value of I_c is usually more easy to define (see Figure 29). The uncertainty ΔI_c is usually between 0.5% and 3%. These uncertainties, ΔA, ΔH_{c_2} and ΔI_c, are probably the biggest sources of error. There are also errors due to the various approximations used in computing κ_1 and the pinning constants.

The error in the parameter K_1' can be described by

$$\Delta K_1' = \Delta A + \Delta I_c + 4\Delta H_{c_2} + \ldots$$

This equation yields an uncertainty of at least 20%. Similar relations can be found for the other parameters.

The uncertainty in the microstructural analysis is unavailable. Some comments can be made about this uncertainty. The uncertainty in ρ is much higher for specimens with small precipitates. The specimen thickness in the area which is under the transmission electron microscope is computed to find ρ. This thickness is computed from the diameter of the precipitates that cut through

both surfaces of the area under observation. The specimen thickness cannot be accurately calculated for specimens without precipitates large enough to cut through these surfaces. Hence, there is a larger uncertainty in the density of precipitates for these specimens.

Most of the specimens that show a line-pinning region have precipitate diameters smaller than 2ξ. For these specimens, it can be assumed that the whole volume of a precipitate, V, can lie within a fluxoid. Specimens #83 and #94 have diameters much larger than 2ξ. These two specimens fit the curve shown in Figure 34 only if the volume $\overline{V}$, given by Equation (2.72), is used.

For high pinning center densities, the pinning center density per unit length of flux line, n_1, is proportional to $\rho^{1/3}$, and the density of pinned fluxoids per cross-sectional area of the specimen, ρ_1, is roughly proportional to $\rho^{2/3}$. Equation (2.19), derived by Kramer [1] for the line-pinning region, can be expressed as

$$F_p \propto \rho^2 V^4 H_{c_2}{}^{4.5} \frac{(2\kappa_1{}^2-1)^3}{\kappa_1{}^8} \frac{h^{6.5}}{(1-h)^2} \quad , \tag{4.39}$$

which for high values of κ yields

$$F_p \propto \rho^2 V^4 \frac{H_{c_2}{}^{4.5}}{\kappa_1{}^2} \frac{h^{6.5}}{(1-h)^2} \quad . \tag{4.40}$$

The temperature and microstructure dependence of this equation is similar to that found for our specimens (Equation 4.37), the form factor f(h) is not. If the proximity effect on the precipitates

is taken into consideration, Equation (2.75) must be used in calculating F_p from Equation (2.90). The result of this calculation is

$$F_p \propto \rho^2 d^2 V^4 \frac{H_{c_2}^{4.5}}{\kappa_1^2} (1-t)^4 \frac{h^{6.5}}{(1-h)^2} \quad . \tag{4.41}$$

The temperature and reduced field dependence of this equation is not similar to that obtained for our specimens.

Labush's equation (Equation 2.82) is of the form

$$F_p \propto \rho d V^2 \frac{H_{c_2}^{3.5}}{\kappa_1^4} f(h) \quad , \tag{4.42}$$

where

$$f(h) = h^{2.5}(1-h)^2 \left\{ \left[h^2 + \frac{0.18(1-h)^2}{(2\kappa_1^2-1)} \right]^{-1/2} + \frac{2.36(2\kappa_1^2-1)^{1/2}}{(1-h)} \right\} \tag{4.43}$$

The fit of this equation to our specimens is improved if the proximity effect is included. Using Equation (2.75), Equation (2.81) yields

$$F_p \propto \rho d^2 V^2 \frac{H_{c_2}^{3.5}}{\kappa_1^4} (1-t^2) f(h) \quad , \tag{4.44}$$

The dependence on the microstructure and on temperature of this equation is similar to that of Equation (4.37). The form factor and the κ-dependence of the two equations are quite different.

A slight change in Kramer's theory of line pinning [1] yields a form of the pinning force density similar to that given by Equation (4.37). Kramer considers the case where the fluxoids can move a distance f_p/c_{66} to thread through more pinning centers. This yields an effective interaction force

$$f_p^* \propto \frac{f_{pl}^2}{c_{66}} \quad . \tag{4.45}$$

The effective interaction force, f_p^*, is then used in calculating the pinning force density from Equations (2.83) and (2.84).

If the material has a high density of pinning centers, Equation (4.45) is invalid. In this case, the interaction force per unit length of fluxoid, f_{p_l}, is used directly in Equation (2.88) to find the elastic energy density per unit length of pinned fluxoid, E_{sp}. The pinning force density is then calculated as for Equation (2.91), obtaining

$$F_p \propto \rho_l n_l^2 V^2 H_{c_2}^{3.5} \frac{(2\kappa_l^2-1)}{\kappa_l^4} h^{3.5} \quad . \tag{4.46}$$

For high precipitate densities n_l is proportional to $\rho^{1/3}$, and ρ_l is roughly proportional to $\rho^{2/3}$. If the contribution of the proximity effect on the precipitates, given by Equation (2.75), is used, Equation (2.88) yields

$$F_p \propto \rho^{4/3} d V^2 H_{c_2}^{3.5} (1-t)^2 \frac{(2\kappa_l^2-1)}{\kappa_l^4} h^{3.5} \quad . \tag{4.47}$$

A numerical analysis shows that, for values of the reduced field greater than h = 0.2 and less than h = 0.8, $h^{3.5}$ is approximately proportional to $h^{1/2}(1-h)^{-2}$. Furthermore, for several specimens $h^{3.5}$ is actually a better description of the reduced-field behavior than $h^{1/2}(1-h)^{-2}$, as sown in Figure 35. Therefore, the form factor of Equation (4.37) can be substituted by

$$f(h) = h^{3.5} \quad , \tag{4.48}$$

with an appropriate change in q_1. Equation (4.47) is then similar to Equation (4.37) in its variation with reduced field, temperature, κ, and microstructure.

c) Plastic Deformation Region

At high reduced fields, usually above h = 0.85, the specimens behave as predicted by Kramer [1]. Kramer predicts a pinning force density,due to plastic deformation of the fluxoid lattice, of the form (Equation 2.97)

$$F_p \propto \frac{K_p H_{c_2}^{5/2} h^{1/2}}{\kappa_1^2} (1-h)^2 \quad , \tag{4.49}$$

where the parameter K_p has a weak dependence on the density of precipitates.

At these high fields, the specimens follow the form factor of Equation (4.49), as seen in Figure 19. This form factor has been observed elsewhere [1,54]. Equation (4.49) can be expressed as

$$F_p = C_p h^{1/2}(1-h)^2 \quad . \tag{4.50}$$

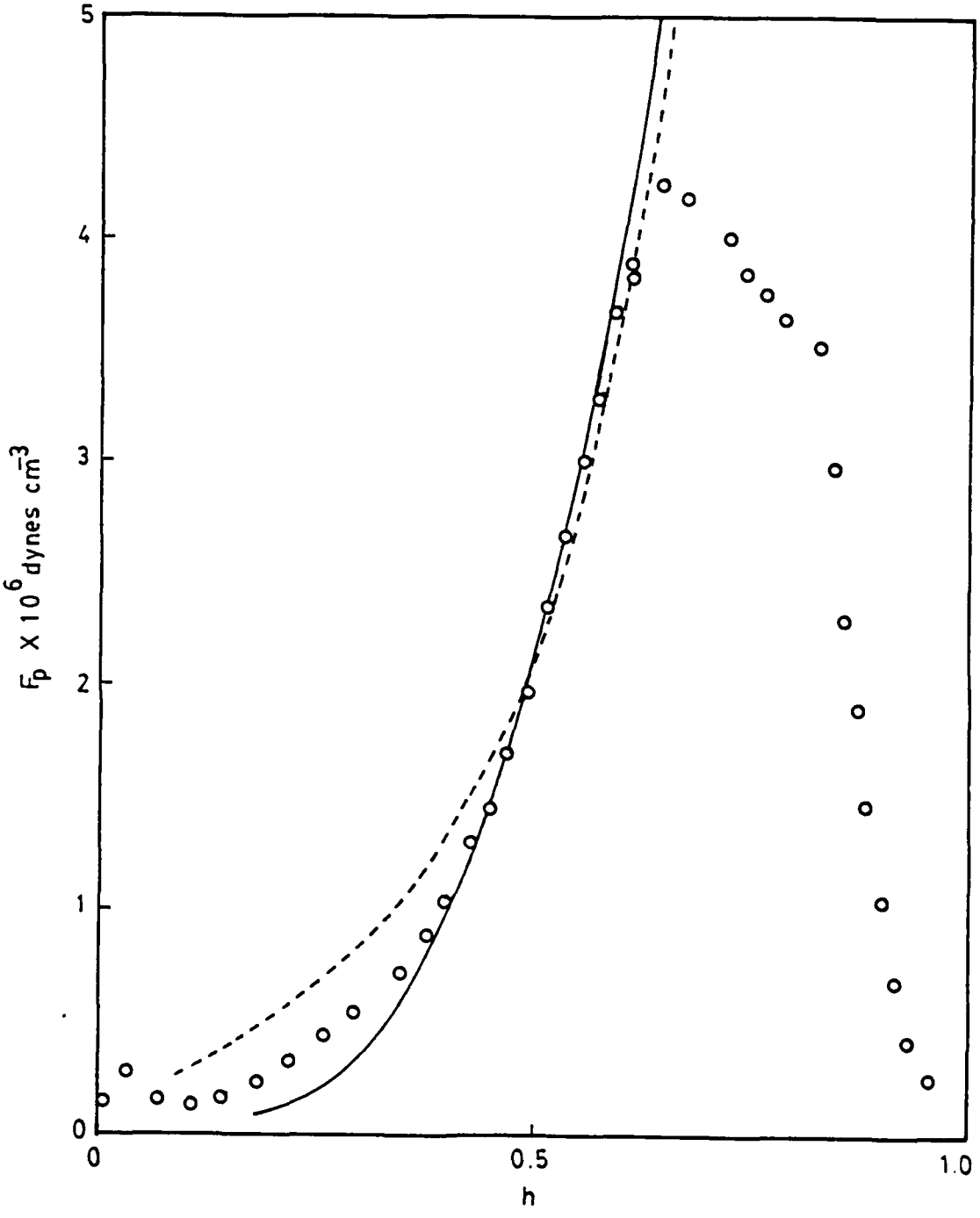

Figure 35) Pinning force density, F_p, versus reduced field, h, for specimen #93 at 2.5 K. The solid line shows $f(h) = h^{3.5}$, and the dash line shows $f(h) = h^{1/2}(1-h)^{-2}$.

The temperature dependence of C_p is calculated, as in the line-pinning region, from a least mean square fit of ln C_p versus ln $H_{c_2}(t)$ for each specimen. The value of n, the exponent of $H_{c_2}(t)$, is given for each specimen in Table 5. The average value of n is 2.3, with a standard deviation of 0.8. There is a weak dependence on alloy concentration, with n increasing as the alloy concentration increases. The expression for the pinning-force density now becomes

$$F_p = K_p \, H_{c_2}{}^{2.5}(t) \, h^{1/2}(1-h)^2 \quad . \tag{4.51}$$

The parameter K_p is calculated for each specimen from

$$K_p = \frac{C_p(t)}{H_{c_2}{}^{2.5}(t)} \quad , \tag{4.52}$$

and averaged over all temperatures. Again, temperatures within 9% of T_c are not used in this calculation.

According to Kramer's theory [1], the parameter K_p has a weak dependence on the precipitate density, ρ. In this theory, the pinning force density in the plastic deformation region is independent of the elementary interaction force, f_p, and independent of V. If the parameter K_p is plotted against the density of precipitates, it shows a dependence on $\rho^{1/3}$ for the pure vanadium specimens. When each alloy concentration is treated individually, these groups do not show this dependence on precipitate density.

Several combinations of density and volume were also tried. The alloyed specimens do not seem to follow any specific combination. The pure vanadium specimens also fit to a dependence on ρd^2. As noted in the previous section, ρV is a constant for many of these specimens. Hence, a dependence on $\rho^{1/3}$ can be approximated by a dependence on ρd^2.

If we assume that the pinning force density of the alloys do depend on $\rho^{1/3}$, a dependence of F_p on the Ginzburg-Landau parameter, κ_1 is satisfied using κ_1^2. Figure 36 shows a plot of

$$F_p = q_p \rho^{1/3} \frac{H_{c_2}^{2.5}(T)}{\kappa_1^2(o)} h^{1/2}(1-h)^2 \quad . \tag{4.53}$$

for most of the specimens. This plot shows that the apparent failure of the F_p of the alloys to show a dependence on $\rho^{1/3}$ is probably due to the large uncertainty involved in calculating C_p. The parameter q_p of Equation (4.53) is calculated from

$$q_p = \frac{\Sigma K_p \kappa_1^2(o)}{\Sigma \rho^{1/3}} \tag{4.54}$$

summed over most of the specimens, yielding, $q_p = 4.9 \times 10^{-5}$ with a standard deviation of 3.3×10^{-5}. Specimens #42 and #94 are not used in this calculation because their value of $K_p \kappa_1^2/\rho^{1/3}$ are more than two standard deviations higher than the mean. Equation (4.53) is similar to that predicted by Kramer for plastic deformation of the FLL, Equation (4.49).

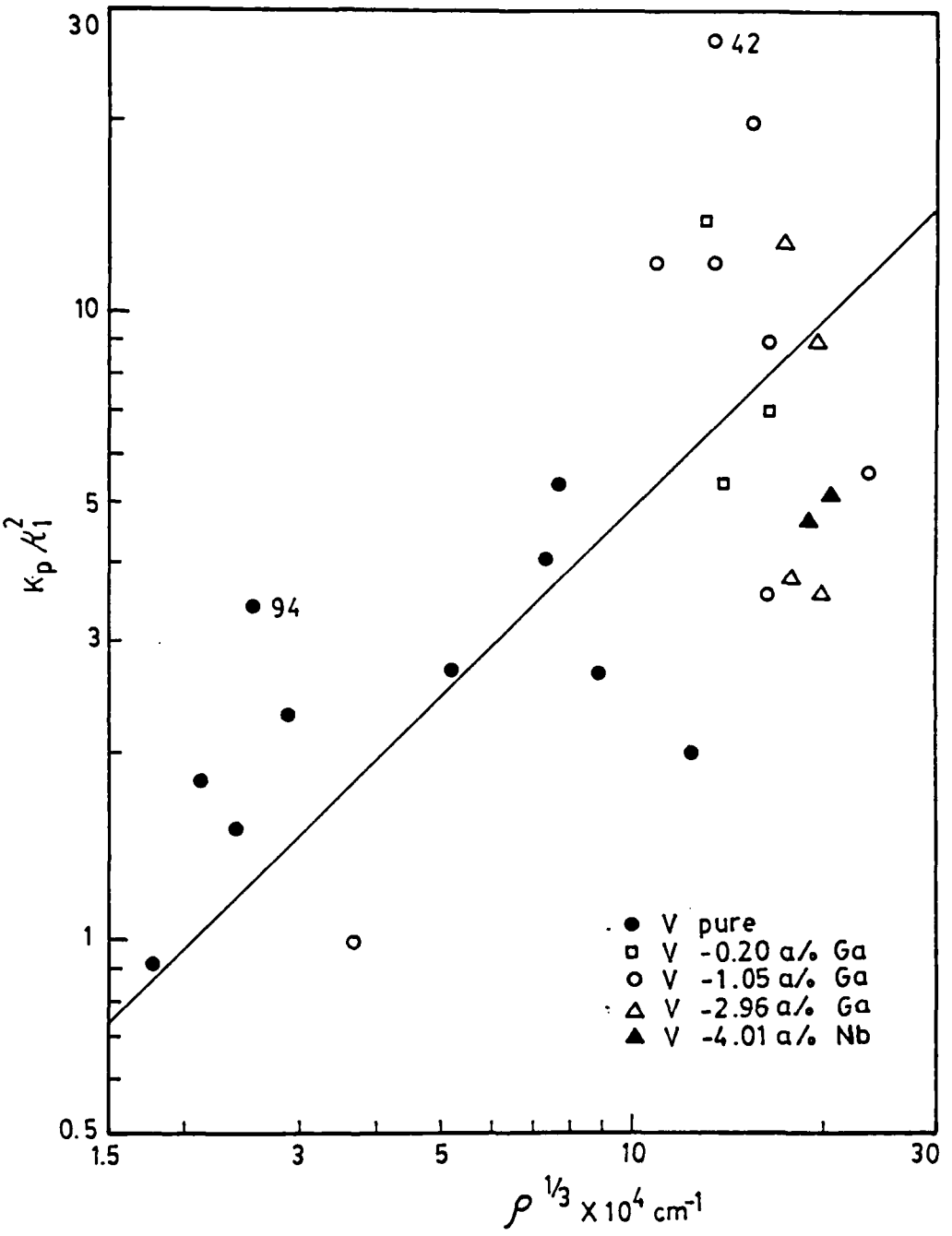

Figure 36) Log-log plot of $K_p \kappa_1^2$ versus $\rho^{1/3}$ for most of the specimens. The straight line shows the fit to $q_p = 4.9 \times 10^{-5}$.

d) Transition Region

Most of the specimens exhibit a transition region between the line-pinning region and the plastic deformation region; only the specimens with very small precipitates ($d<<\xi$) do not show this region. In the case of the specimens with a high density of large pinning centers ($d>\xi$), the transition region occupies a large fraction of the reduced field range. There is no direct equivalent in Kramer's theory [1] to this transition region. In Kramer's theory, the transition from the line-pinning region to the plastic deformation region occurs smoothly over a certain reduced-field region. The pinning force density in Kramer's transition region results from a statistical summation of line-pinning forces and plastic deformation depinning forces. As such, it is strongly dependent on the precipitate dimensions. No such dependence is found for the specimens in this research for the "transition region." Furthermore, there is usually a clearly defined boundary between this region and the others, whereas Kramer's transition region smoothes out the boundaries. The observed transition region can also be detected in the pinning force densities obtained by other authors, particularly in the data from Kes, et al. [54] for voids in superconducting vanadium. However, none of these authors identify this region as a distinct reduced-field region.

The transition region, as opposed to the two regions discussed in the previous sections, shows a marked dependence on the alloy

composition. In this region, the pure vanadium specimens exhibit a form factor of the form

$$f(h) = h(1-h) \quad , \tag{4.55}$$

as shown in Figure 37. However, the alloys exhibit a more complicated behavior. Certain reduced field regions can be accurately described by (see Figure 38)

$$F_p = C_A h^{1/2}(1-h)^2 + b \quad , \tag{4.56}$$

where b is a constant of the order of $F_p max$, usually near $F_p max/2$. The behavior of the alloys on the higher reduced fields can also be roughly described by

$$f(h) = (1-h)^{1/2} \quad . \tag{4.57}$$

Figure 39 illustrates the fit of several specimens to this equation. This equation does not provide as close a fit to the data as Equation (4.56), but it is useful in describing, in a simple way, the total shape of the transition region for most alloys.

In this region there is no reduced field dependence common to both the pure vanadium specimens and the alloyed specimens. Furthermore, the reduced field dependence of the alloyed specimens is only roughly described by Equation (4.57). Therefore, the pinning force F_p at h = 0.7 was used in the least mean fit of log F_p versus log $H_{c_2}(T)$ used to find n, the exponent of $H_{c_2}(T)$, and in other calculations. Again, the value of n varies with the

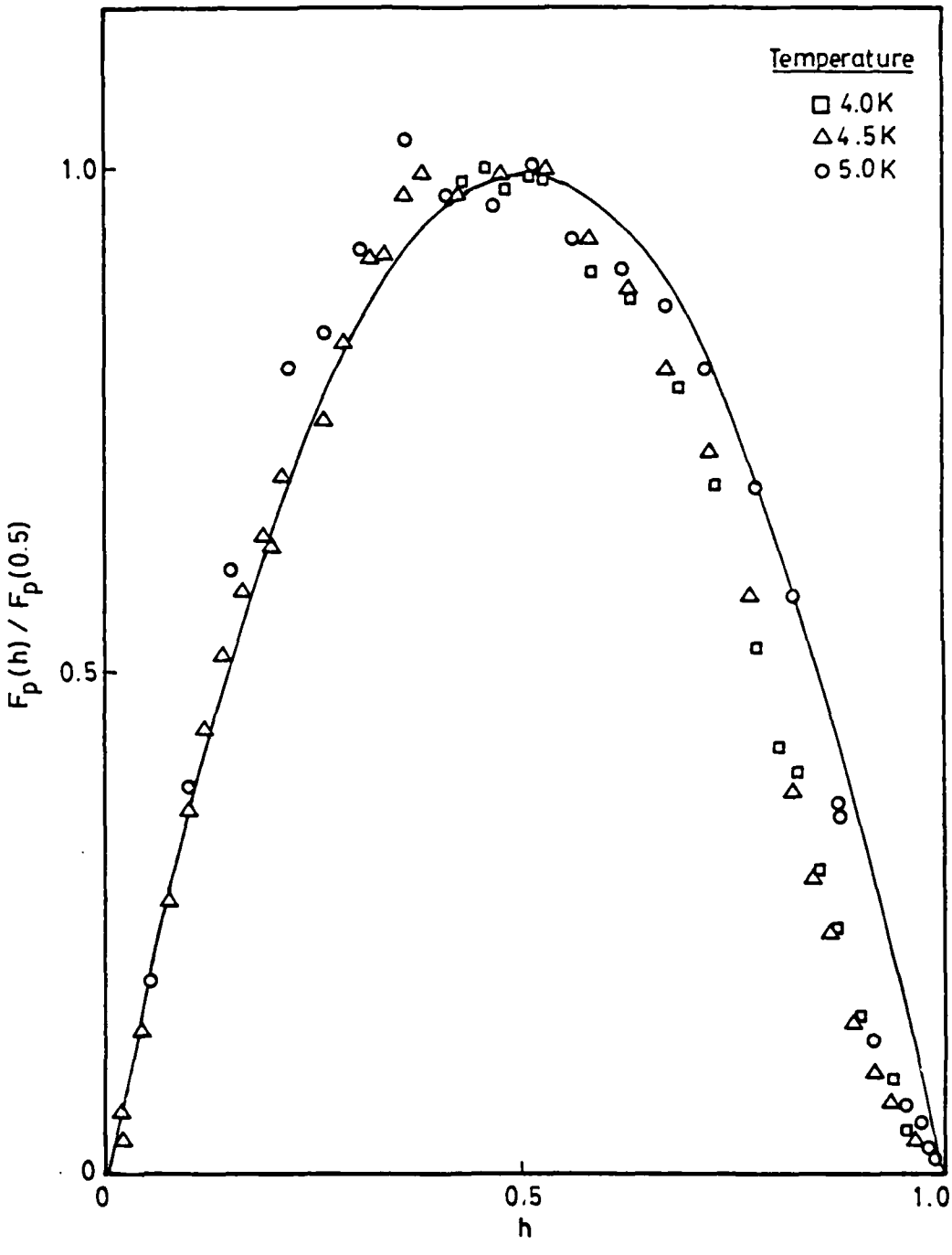

Figure 37) Reduced pinning force versus reduced field, h, for specimen #65 at the temperatures 4.0K, 4.5K, and 5.0K. The solid line indicates the form factor f(h) = h(1-h).

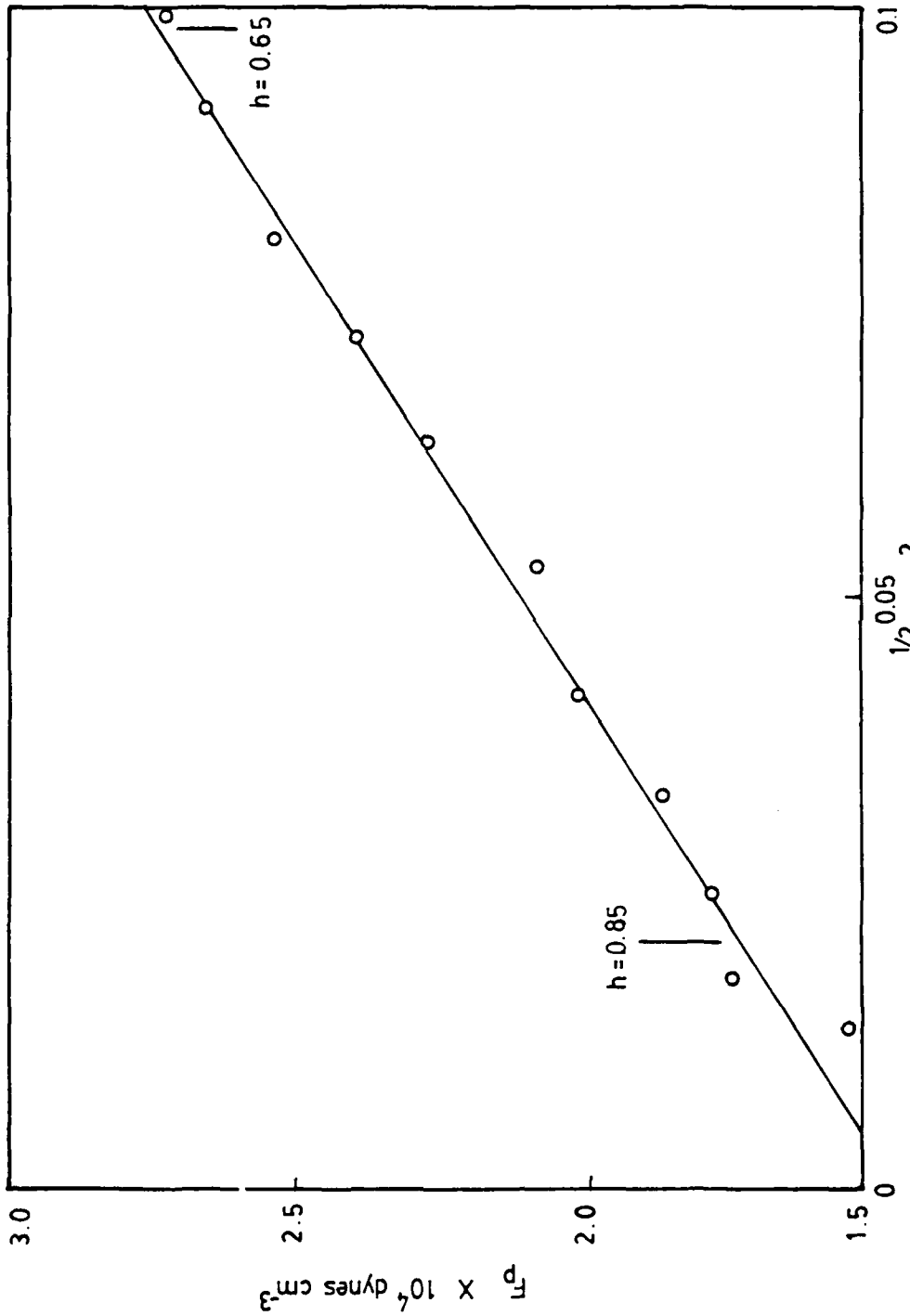

Figure 38) Pinning force density versus $h^{1/2}(1-h)^2$ for specimen #67 at 1.5K.

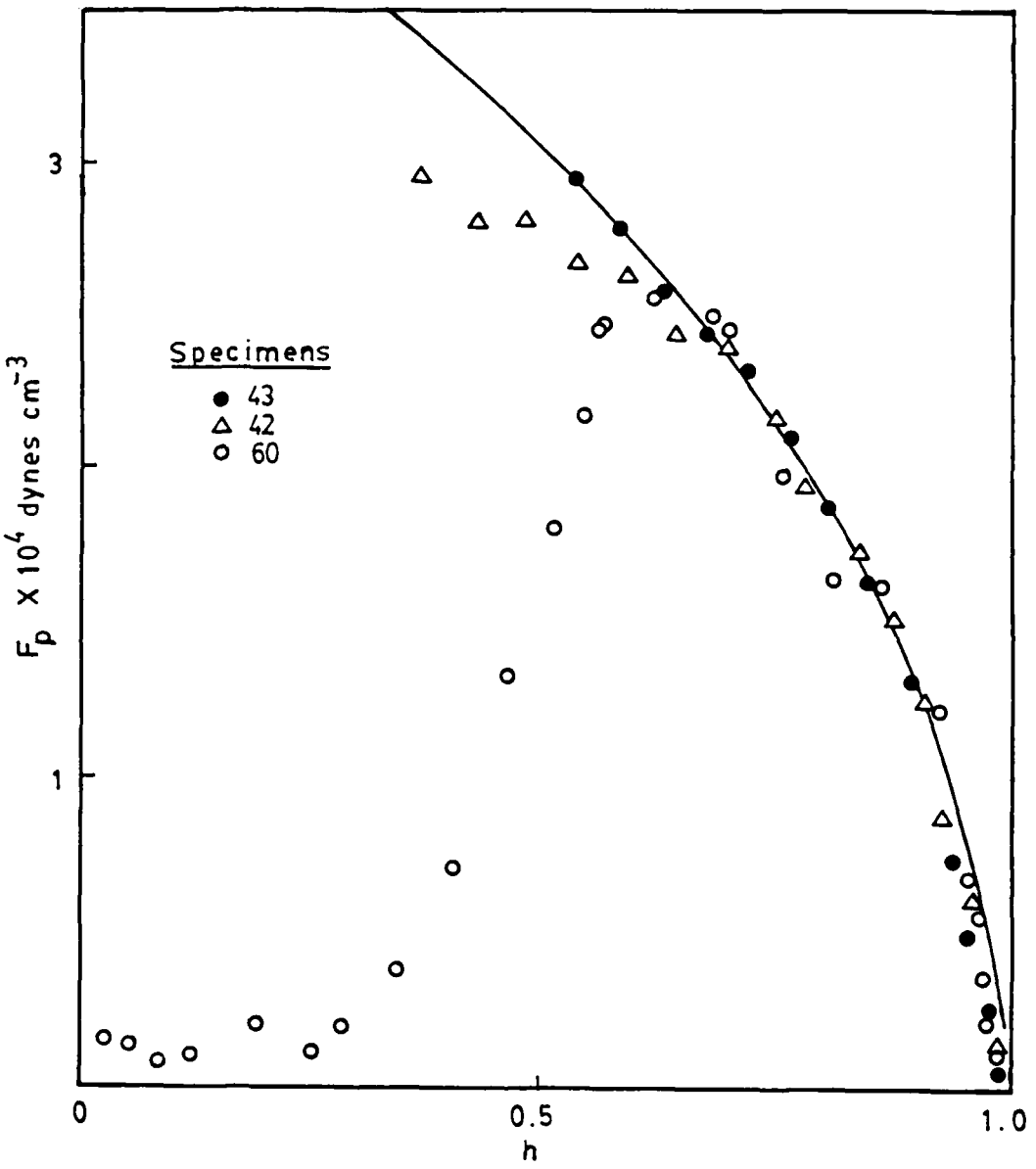

Figure 39) Pinning force density, F_p, versus reduced field, h, for specimens #42, #43 and #60 at 2.0K. The solid line indicates the form factor $f(h) = (1-h)^{1/2}$.

alloy concentration. The average value of n for pure vanadium is 2.1, and that for the alloys is 2.6, with a standard deviation of 0.3 for both of the averages.

The pinning force density of the pure vanadium specimens can now be expressed as

$$F_p = K_v H_{c_2}^{\ 2} h(1-h) \quad . \tag{4.58}$$

The parameter K_v is obtained, for each specimen, at h = 0.7 using

$$K_v = \frac{F_p(h)}{H_{c_2}^{\ 2} h(1-h)} \tag{4.59}$$

averaged for all temperatures. For the alloys we have

$$F_p = K_a H_{c_2}^{\ 2.5} (1-h)^{1/2} \tag{4.60}$$

where

$$K_a = \frac{F_p(h)}{H_{c_2}^{\ 2.5} (1-h)^{1/2}} \quad , \tag{4.61}$$

calculated at h = 0.7 and averaged for all temperatures.

Several combinations of the microstructural parameters, such as ρV, ρA, etc. were plotted against K_a. Of these, only $\rho^{1/3}$ gives some correlation. The V - 1.05a/o Ga specimens show the best fit to this dependence. The V - 2.96a/l specimens show a poor dependence on $\rho^{1/3}$, and there are not enough V - 0.20a/o Ga and V - 4.01a/o Nb specimens that show the transition region to test their dependence

on $\rho^{1/3}$, most of the alloyed specimens seem to fall on a line given by

$$F_p = q_a \rho^{1/3} \frac{H_{c_2}^{2.5}(T)}{\kappa_1^2(o)} (1-h)^{1/2} \qquad (4.62)$$

where $h = 0.7$. The parameter q_a is calculated, at $h = 0.7$, using

$$q_a = \frac{\Sigma K_a \kappa_1^2(o)}{\Sigma \rho^{1/3}} \quad , \qquad (4.63)$$

summed over most of the alloyed specimens yielding $q_a = 9.3 \times 10^{-7}$, with a standard deviation of 2.6×10^{-7}. Specimen #81 is not used in this calculation because its value of $K_a \kappa_1^2/\rho^{1/3}$ is more than two standard deviations lower than the mean. Figure 40 shows the fit of most of the alloyed specimens to Equation (4.62).

The pure vanadium specimens do not fit the same line, given by Equation (4.62), with the alloyed specimens. In fact, if Equation (4.63) is used for the pure vanadium specimens, the value of q_a obtained for these specimens is about ten times larger than that obtained for the alloys. The analysis of the pinning force of the pure specimens is therefore treated independently from that of the alloys. There is at present no way to find the dependence of F_p on κ_1 for the pure specimens.

As seen in Figure 41, the pure vanadium specimens show a weak dependence of K_v on $\rho^{1/3}$. However, attempts to find a better correlation of K_v with other combinations of microstructural parameters such as ρA, ρV, etc., were futile. There is a poor correlation of K_v

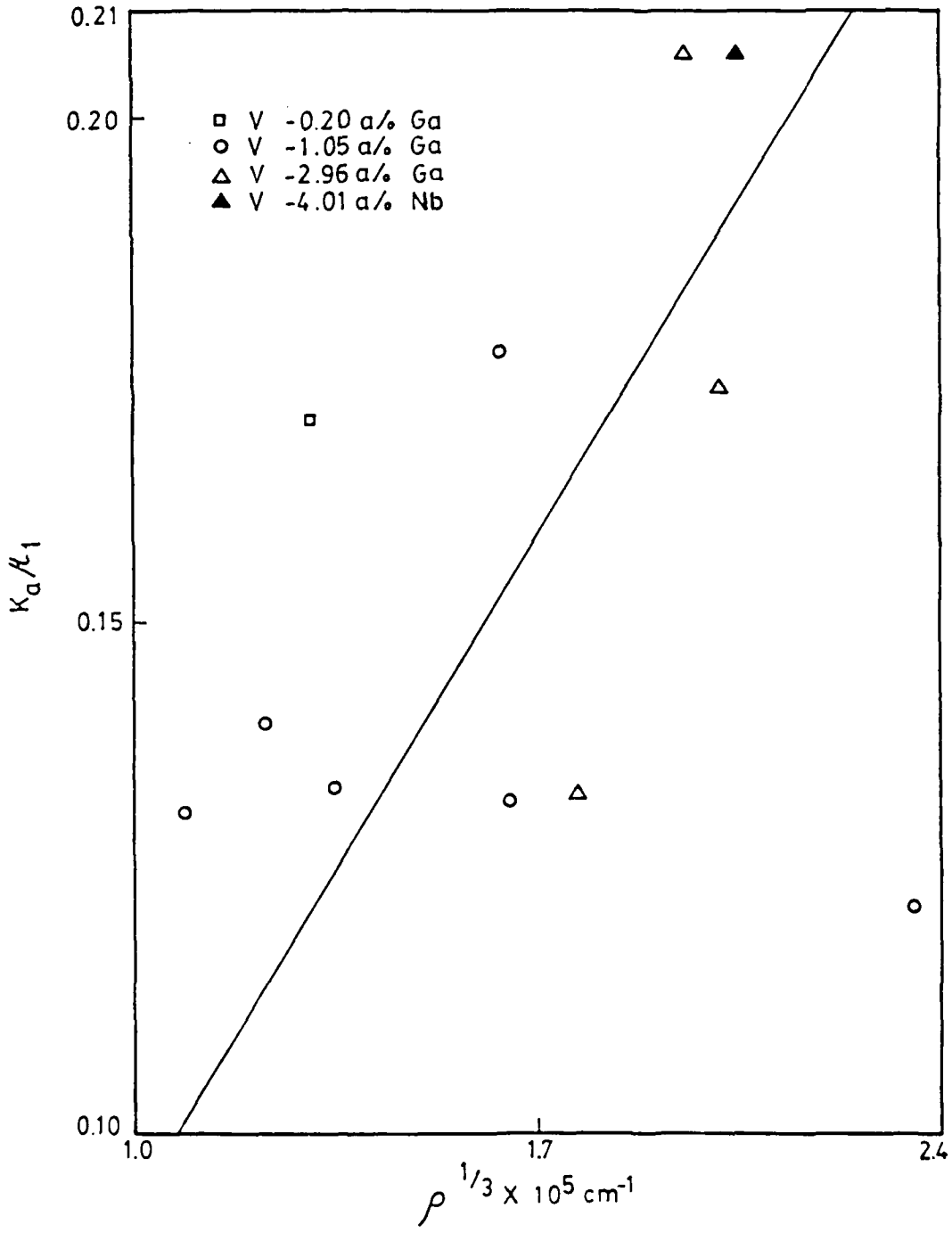

Figure 40) Plot of the product $K_a\kappa_1^2$ versus $\rho^{1/3}$, at h = 0.7, for most of the alloyed specimens. Solid line indicates the fit to $q_a = 6.8 \times 10^{-7}$.

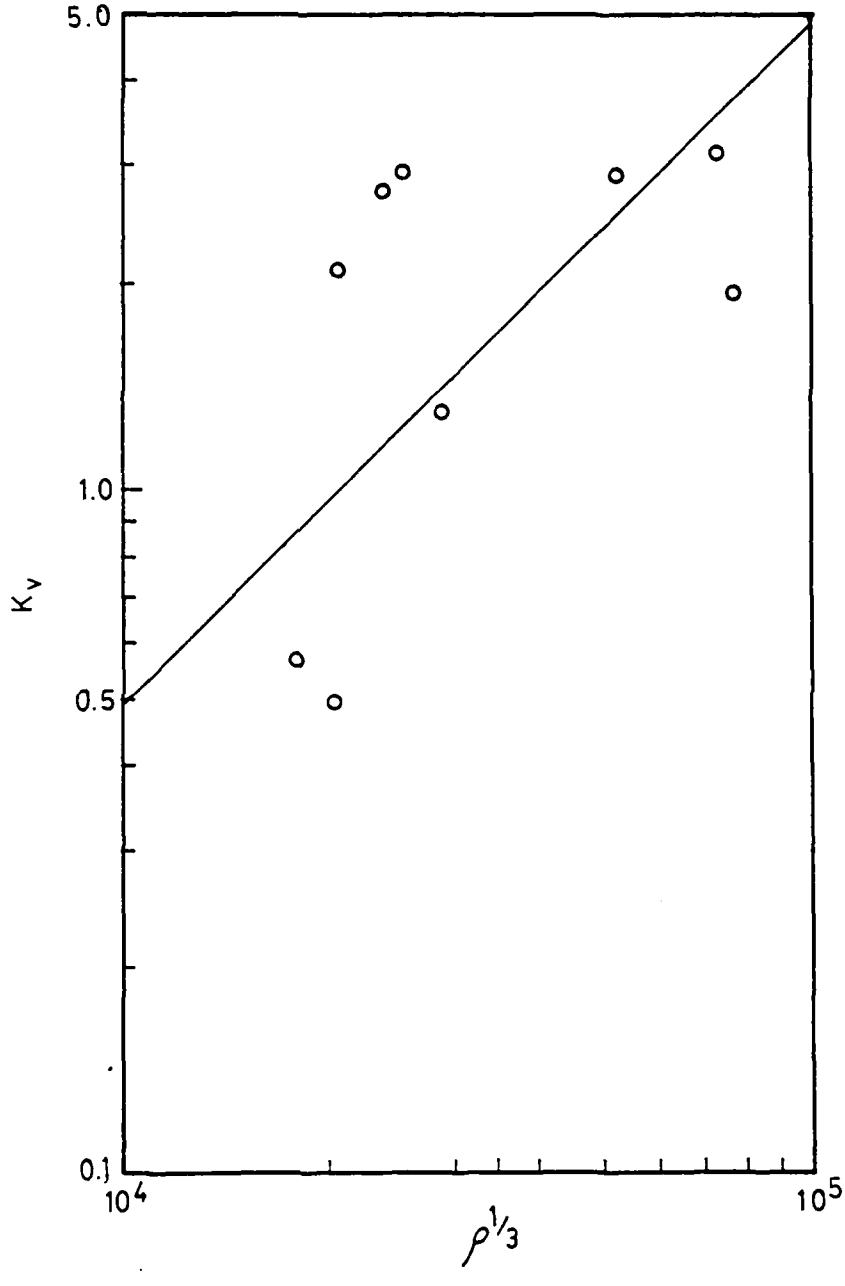

Figure 41) Log-log plot of K_v versus $\rho^{1/3}$, at h = 0.7, for most of the pure vanadium specimens. The straight line is given by $q_v = 4.9 \times 10^{-5}$.

with $\rho V^{2/3}$. For our specimens, $V^{2/3}$ is a meaningless parameter. The parameter $V^{2/3}$ is not equal to an area of the precipitate. This correlation of $\rho V^{2/3}$ with K_v is due to the fact that $V\rho$ is a constant for specimens with the same carbon concentration and that $K_v \alpha \rho^{1/3}$. Therefore, for the pure vanadium specimens we have

$$F_p = q_v \rho^{1/3} H_{c_2}^{\ 2}(T)\ h(1-h) \quad . \tag{4.64}$$

where q_v is calculated at $h = 0.7$ using the equation

$$q_v = \frac{\Sigma K_v}{\Sigma \rho^{1/3}} \tag{4.65}$$

summed over all pure vanadium specimens. The constant q_v equals 5.6×10^{-5} with a standard deviation of 3.7×10^{-5}.

There is no direct equivalent in the theory to Equations (4.62) and (4.64). However, Equation (4.62) is somewhat similar to Kramer's equation for the plastic deformation mechanism (Equation 2.97). On the other hand, Equation (4.64) is similar to Schmucker's (Equation 2.105). In any case, this region seems to be strongly influenced by a plastic deformation of the FLL mechanism because there is no dependence of F_p on precipitate volume; no dependence on V means no dependence on f_p. This implies that the fluxoids are not breaking their individual bonds with the pinning centers; the FLL is deforming plastically around the pinned fluxoids.

e) Resulting Scaling Law

Apart from the point pinning region, the pinning force density for a given reduced field is given by the mechanism which yields

the lowest pinning force density for that reduced field. There are at least four pinning force density equations, which are:

i) in the line pinning region ($h_1 < h < h_T$), using Equation (4.48),

$$F_p = 5.3 \times 10^{31} \rho V^3 \frac{H_{c_2}^4(T)}{K_1^{2.5}(o)} \frac{h^{1/2}}{(1-h)^2} \qquad (4.66)$$

ii) in the transition region ($h_T < h < h_p$)

$$F_p = 5.6 \times 10^{-5} \rho^{1/3} H_{c_2}^{2.5}(T) h(1-h) \qquad (4.67)$$

for the pure specimens, and

$$F_p = 9.3 \times 10^{-7} \rho 1/3 \frac{H_{c_2}^{2.5}(T)}{\kappa_1^2(o)} (1-h)^{1/2} \qquad (4.68)$$

for the alloys.

iii) in the plastic deformation region ($h_p < h < 1.0$)

$$F_p = 4.9 \times 10^{-5} \rho^{1/3} \frac{H_{c_2}^{2.5}(T)}{\kappa_1^2(o)} h^{1/2}(1-h)^2 \qquad (4.69)$$

An example of a resulting pinning force density for a specimen is shown in Figure 42.

Each reduced-field region has a different temperature dependence. Hence, the resulting pinning force density does not scale with temperature over all the reduced field regions. The boundary between the line-pinning region and the next higher region moves to lower reduced fields as the temperature is decreased (see Figure 43).

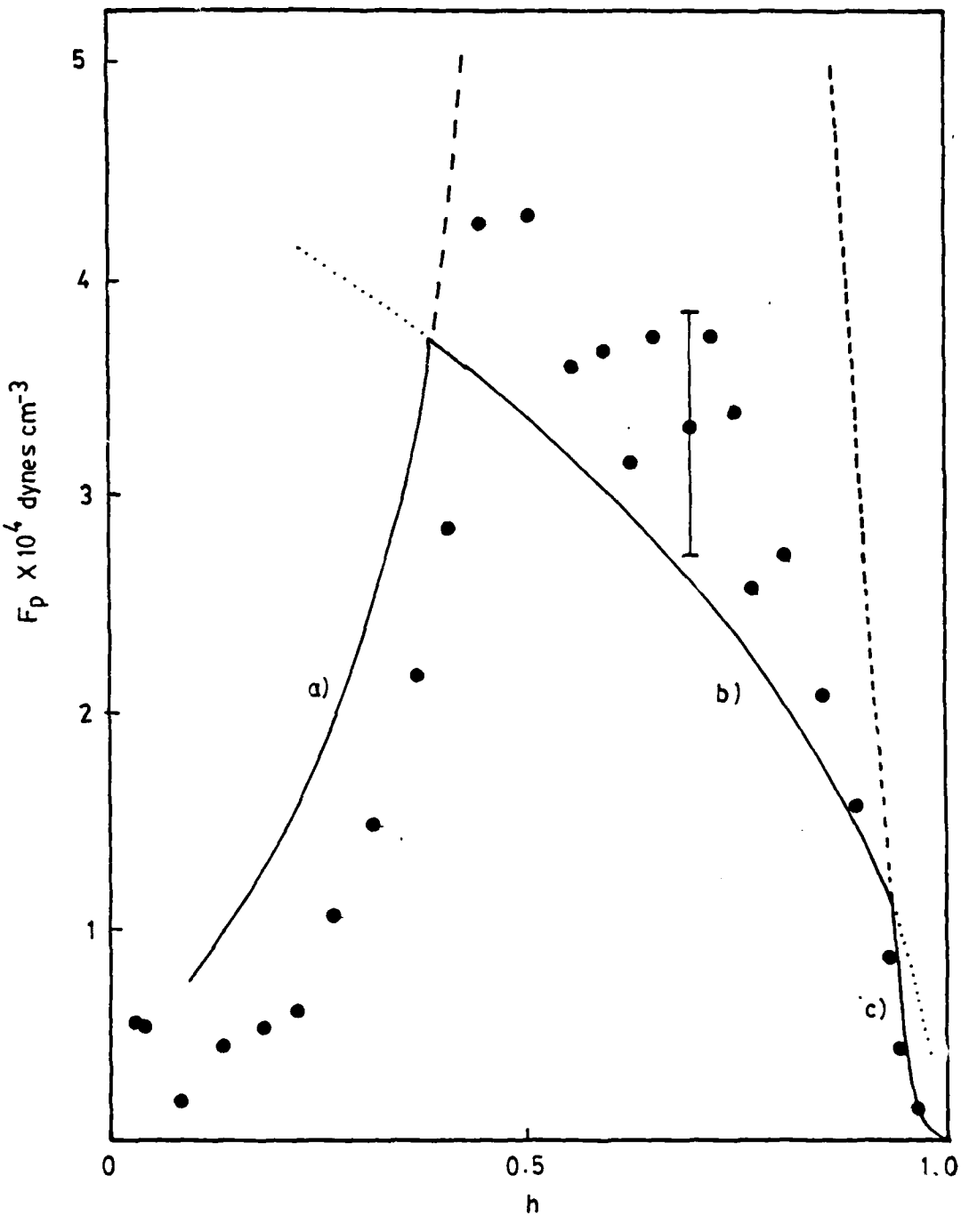

Figure 42) Pinning force density versus reduced field for specimen #47 at 3.5K. The solid line shows the pinring force density predicted for this specimen by a) Equation (4.66), b) Equation (4.68), and c) Equation (4.69).

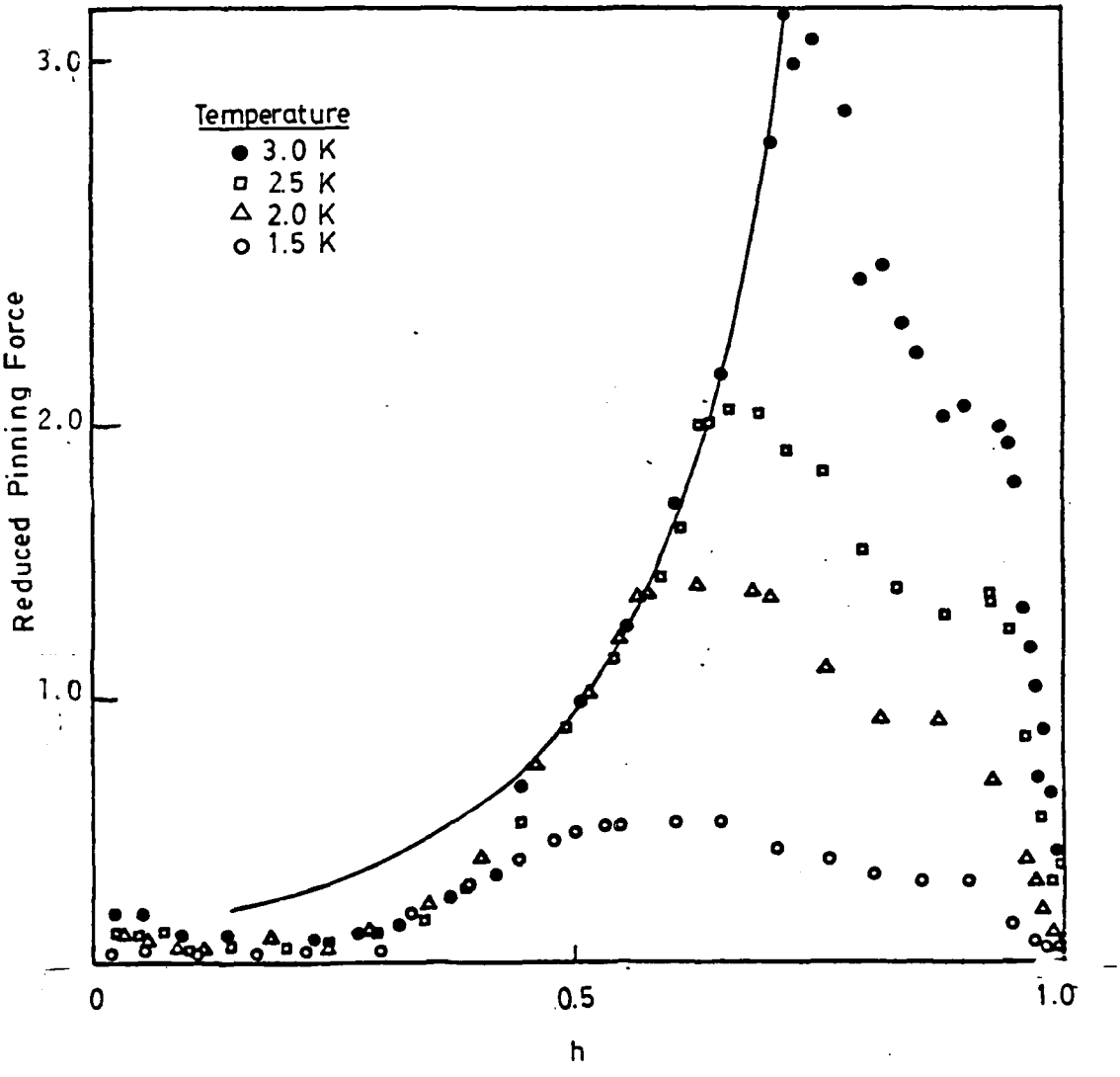

Figure 43) Scaling of the pinning force density in the line-pinning region versus the reduced field for specimen #60.

f) General Comments

The theories of Dew-Hughes [32] and of Labush [33] fail to predict the appearance of the several reduced-field pinning regions. On the other hand, the theories of Kramer [1] and Campbell and Evetts [9] predict different depinning mechanisms for discrete reduced-field regions. The scaling laws obtained from Kramer's theory are similar to our empirical relations. On the other hand, the theory of Campbell and Evetts fails to describe the data.

Campbell and Evetts [9] do not provide a set of scaling laws for their theory. However, several things can be inferred from their theory. In this theory, our empirical "line-pinning region" is supposed to be described by an unsynchronized FLL region, where the pinning force is basically that given by Dew-Hughes. This fact fails to explain the empirical dependence of the pinning force on the precipitate volume cubed. Furthermore, the character of the empirical V-I curves (Figure 29) is opposite to the one inferred from this theory. When an "unsynchronized fluxoid" moves, it is likely to move to another pinning center. There are no free pinning centers for a fluxoid on a synchronized FLL to move to. Therefore, a moving synchronized-fluxoid can precipitate a massive movement of the lattice. This depinning behavior of the synchronized and unsynchronized fluxoids is opposite to the one observed on the V-I curves. These curves show an abrupt depinning in the "line-pinning region" and a smooth depinning in the other reduced-field regions.

An explanation of the character of the empirical V-I curves can be inferred from Kramer's depinning theory. In the line-pinning region, a fluxoid depins by breaking the bond with the pinning centers along its length. The sudden loss in elastic energy creates a local heat burst that can cause similar depinning in neighboring fluxoids. This effect can cascade and even create a total quench. The plastic-deformation depinning mechanism can be smoother than the line pinning depinning mechanism described above. Therefore, the voltage rise at J_c is less abrupt in the plastic deformation region than in the line pinning region.

As previously mentioned, the specimens alloyed with gallium exhibit a decrease in the critical current when trained. This can be explained if the precipitate expells some gallium from the volume it occupies [48]. The area surrounding the precipitate acquires a higher density of gallium. Therefore, the local value of H_{c_2} increases and that of T_c decreases. At temperatures near the critical temperature of the bulk, the energy well due to the normal precipitate becomes wider with the addition of the now-normal surrounding volume. At lower temperatures, the increased value of the local H_{c_2} creates an energy barrier around the precipitate due to the increase in condensation energy (see Figure 44). When a specimen is cooled from the normal state while it is in a magnetic field, the fluxoids are attracted to the broad well produced by the precipitate and the gallium enriched region. With further cooling and the advent of the energy barrier, the fluxoids remain pinned inside the well. However, if the fluxoids are driven

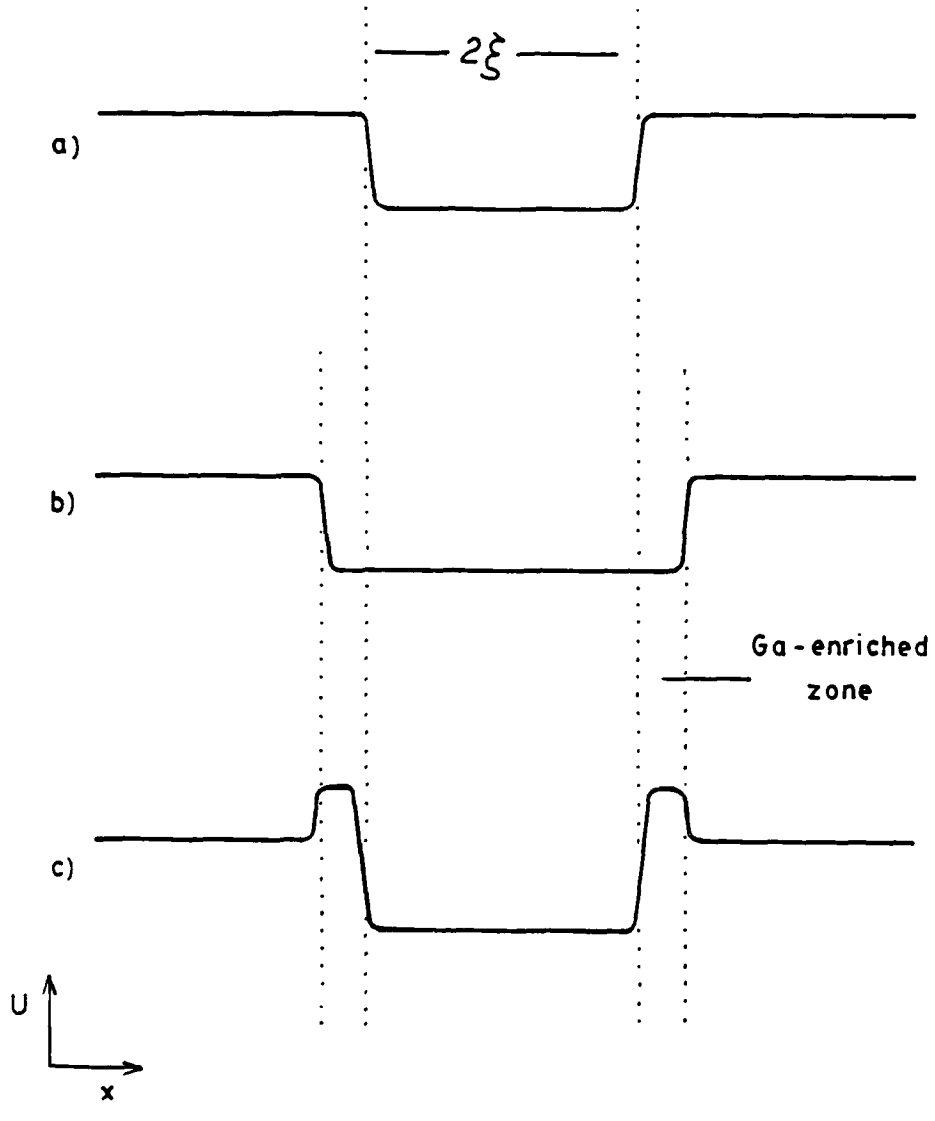

Figure 44) Potential well due to a) a normal precipitate, b) a normal precipitate surrounded by a gallium-rich zone, at a temperature above the T_c of the zone, and c) a normal precipitate surrounded by a gallium-rich zone, at a temperature below the T_c of the zone.

out by a transport current and the current is brought back to zero, some fluxoids cannot re-enter into the well because of the energy barrier. Therefore, these fluxoids are not strongly pinned and the pinning force density decreases. This idea is supported by the fact that the pure vanadium specimens do not exhibit any effects due to training. Furthermore, this effect is absent in the transition and plastic deformation regions, where the pinning force is not expected to be dependent on the elementary interaction forces.

Another way to analyze the pinning force data is to compute the pinning force per pinning center [55,56]

$$Q = F_{p/\rho} \quad , \tag{4.70}$$

and to plot it versus the elementary interaction force, f_p. In this way, it can be verified whether the direct summation, where $Q = f_p$ (Equation 2.77), or the statistical summation, where $Q \propto f_p^2$ (Equation 2.81), can properly describe the data. Figure 45 shows this method applied to most of the specimens. This graph shows a qualitative agreement with the direct summation theory over several orders of magnitude of the interaction force. There is a sudden drop in Q at low interaction forces. This behavior has been observed elsewhere [55,56]. However, as it will be demonstrated below, the fit of the specimens in this research to this direct summation curve is misleading. The specimens with weak interaction forces do not fall on this line. These specimens are the ones that show line pinning up to high reduced fields. Hence, the pinning force density for these specimens is strongly dependent on the magnitude of f_p.

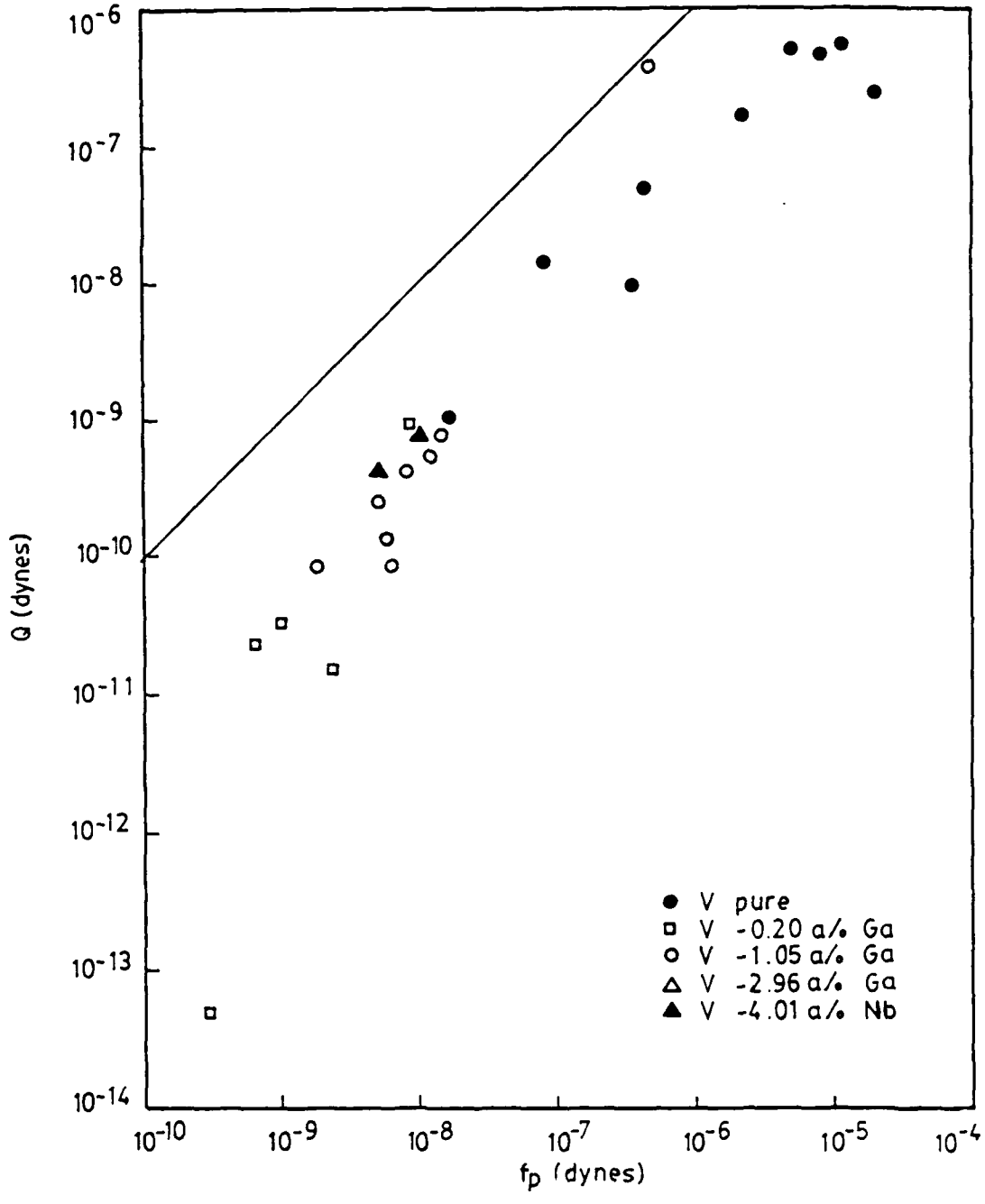

Figure 45) Log-log plot of Q versus f_p, for most of the specimens, at T = 2.5K and h = 0.7. The solid line represents the direct summation.

If the pinning force density of the specimens can be described by the direct summation, a plot of F_p versus ρf_p should be linear. Figure 46 shows that for our specimens, this plot is not linear. Hence, the pinning force density of the specimens in this research cannot be described by the direct summation theory. The fact that Figure 45 seems to indicate that there is a direct summation of forces is easy to explain. The specimens with large precipitates usually have pinning force densities of the same order of magnitude. For these specimens, a plot of Q versus f_p is equivalent to a plot of ρ^{-1} versus V. Due to the fact that the product ρV is almost a constant, this plot yields a straight line.

3) Uncarburized Specimens

All annealed specimens with no precipitates behave in a similar way. As seen in Figures 24-27, as the magnetic field is increased from zero, these specimens show a sharp drop in critical current density. This drop levels off at higher fields, then it usually peaks near $H_{c_2}(T)$.

The pinning force density behaves fairly erratically as a function of reduced field. Furthermore, the reduced-field dependence sometimes changes from one temperature to another. For most of these specimens, the reduced field dependence of F_p can be approximated at low reduced fields by

$$f(h) = h^{1/2}(1-h)^2 \quad , \tag{4.71}$$

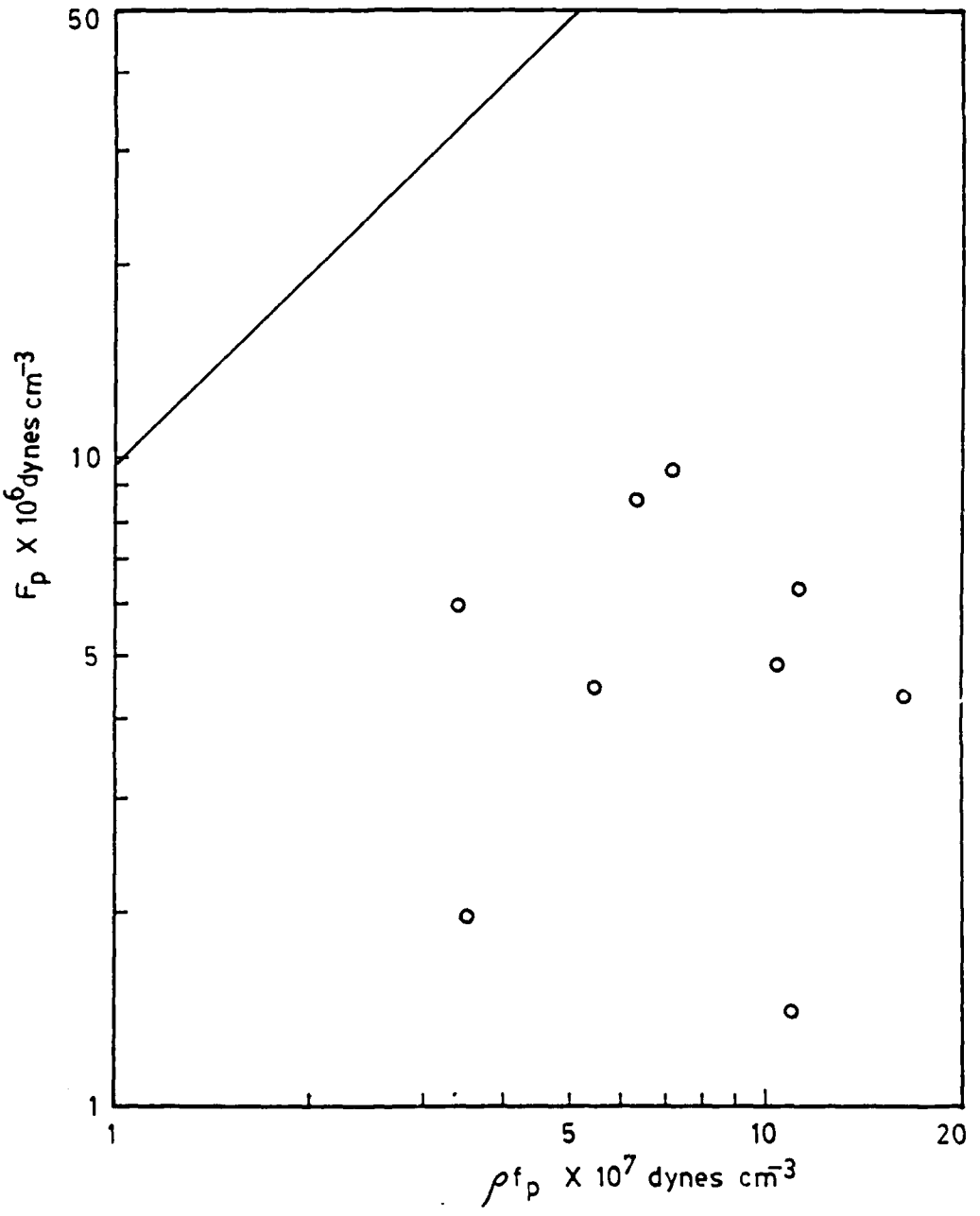

Figure 46) Log-log plot of F_p versus ρf_p for the vanadium specimens at T = 2.5K and $h \leq 0.7$. The solid line represents the direct summation.

as illustrated in Figure 47. The temperature dependence of this region, obtained from

$$\ln F_p(h = 0.5) = n \ln H_{c_2}(T) + \text{constant} \tag{4.72}$$

is approximately given by $H_{c_2}{}^{2.5}(T)$. Following the general trend, we assume a quadratic dependence on the Ginzburg-Landau parameter, yielding the equation

$$F_p = C_{nc} \frac{H_{c_2}{}^{2.5}(T)}{\kappa_1{}^2(o)} h^{1/2}(1-h)^2 \tag{4.73}$$

The parameter C_{nc} is obtained for all temperatures from

$$C_{nc} = \frac{F_p(h)\kappa_1{}^2(o)}{H_{c_2}{}^{2.5}(T)h^{1/2}(1-h)^2} \quad , \tag{4.74}$$

where h = 0.5, and averaged for each specimen. The value for this parameter, as seen in Table 6, is similar for all annealed and uncarburized specimens and even for some specimens with carbon in solid solution. This implies that the assumption of a quadratic dependence on κ_1 is probably correct and that these annealed specimens have similar microstructures.

Most of these specimens show a peak in the pinning force density near $H_{c_2}(T)$. The rise in F_p shows a form factor given by

$$f(h) = h^{1/2}(1-h)^{-2} + b \quad . \tag{4.75}$$

Then, very close to $H_{c_2}(T)$, F_p drops rapidly to zero.

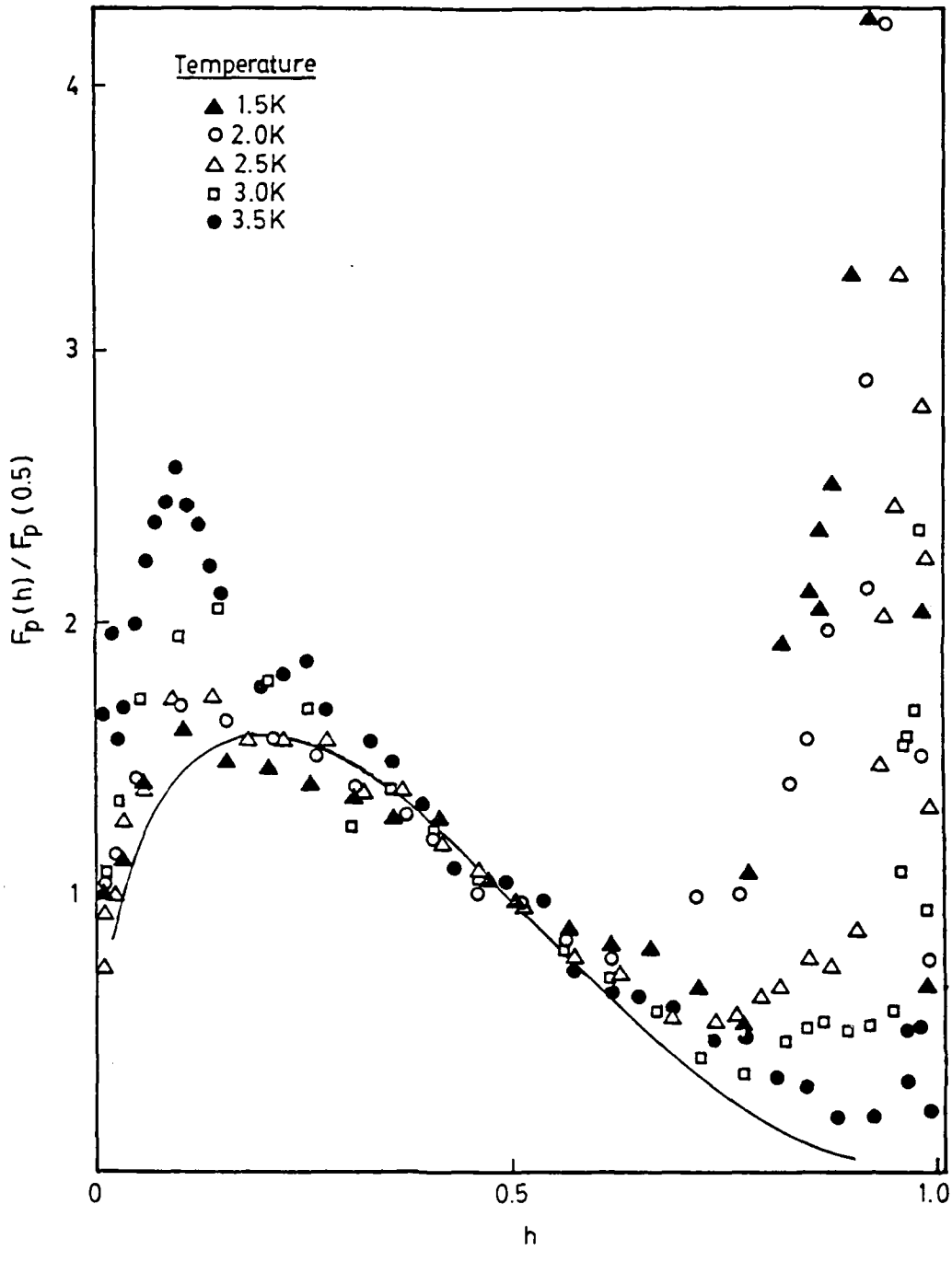

Figure 47) Reduced pinning force density versus reduced field for specimen #61. Solid line indicates the form factor $h^{1/2}(1-h)^2$.

Table 6. Pinning Force Density Parameters for Specimens With No Precipitates.

Specimen #	Alloy Concentration	Carbon Concentration a/o	n	C_{nc} x 10^{-4}
8	pure V	-	2.5	5.97
54	pure V	-	2.4	6.63
86	0.20a/o Ga	0.13	2.5	3.18
30	1.05a/o Ga	-	2.3	1.35
61	1.05a/o Ga	0.20	2.2	2.82
7	2.96a/o Ga	-	2.2	2.05
63	2.96a/o Ga	0.20	2.5	3.21
27	4.01a/o Nb	-	1.6	2.76

The reduced field dependence of F_p seems to indicate a plastic deformation region followed by a line-pinning region. This is the inverse of the usual order of appearance of these regions. This can be explained if one assumes that the fluxoids are pinned by imperfections on the specimen surface. There is a low density, per volume, of these imperfections. Hence, the plastic deformation of the FLL starts at low reduced fields. At higher fields, line pinning forces in the bulk of the material become stronger than the surface pinning forces. These bulk pinning forces are mainly due to elastic interaction forces due to the grain boundaries and other crystal defects.

CHAPTER V

CONCLUSIONS

There is no one scaling law that will universally describe the pinning force F_p. The pinning force for a particular reduced field region is determined by the depinning mechanism active in the region. At least four depinning mechanisms are present.

The first region, which is only present at the lower reduced fields, is of little interest because of its low critical currents. No analysis was attempted for this region which, for simplicity, we call the "point pinning region." At the next higher reduced fields, there is a region where F_p shows a strong dependence on temperature, reduced field, and microstructure. The relation to the microstructure is approximately given by $V^3\rho$. In this region, which is identified with Kramer's line-pinning region, F_p varies with the square of the interaction force f_p.

At the highest reduced fields, usually above $h = 0.8$, all specimens show the same reduced field behavior for F_p, given by $f(h) = h(1-h)^2$. In this region, the dependence of the pinning force on the microstructure is given by $F_p \propto \rho^{1/3}$. This region is well described by Kramer's theory of depinning by plastic deformation of the FLL.

The specimens usually show another region, the transition region, at intermediate fields between the line pinning region and the plastic deformation region. The pinning force in this region

is similar to that of the plastic deformation region in its temperature and microstructure dependence. The reduced field dependence is not the same as that for the plastic deformation region. This is the only region where there is a distinct difference in the form factor of the pure vanadium specimens and that of the alloyed specimens The transition region was unnoticed by previous authors.

The only reduced-field region exhibited by all the specimens is the high-reduced-field plastic deformation region. The appearance of any of the other regions is determined by the microstructure of the specimen. Specimens with small precipitates exhibit the "point-pinning" region and the line-pinning region. Specimens with large precipitates show a broad transition region and barely, if any, of the "point-pinning" or line-pinning regions. Specimens with intermediate-sized precipitates exhibit the transition region at all temperatures, and a clear line-pinning region only at the higher temperatures.

The optimum microstructure for obtaining high pinning force densities can now be described. In the line-pinning region, the pinning force density depends on the cube of the precipitate volume which lies inside the fluxoid core, V^3. For large precipitates ($d>2\xi$), part of the precipitate volume would lie outside any fluxoid core that threads it. This extra volume has a negligible effect on F_p, as seen in specimens #83 and #94. Hence, the optimum precipitate diameter is about 2ξ. Spherical precipitates

have a larger volume than disk-like precipitates of the same diameter. Hence, spherical precipitates would make better pinning centers. Voids are not affected by the proximity effect, hence, a void makes a better pinning center than a precipitate of the same dimensions. Strongly pinned specimens, which are those with a high density of large precipitates, exhibit a broad transition region. This region is dependent on the density of precipitates. Hence, the optimum microstructure would be composed of the higher attainable density of precipitates, or voids, with diameters near 2ξ.

The alloying of small quantities of gallium is a good way of varying κ, providing a range of $\kappa \approx 2.0$ for pure vanadium to $\kappa \approx 20$ for the V - 2.96a/o Ga alloys. The critical temperature and upper critical field, H_{c_2}, can be calculated, from empirical curves, for any dilute V - Ga alloy with a known resistance ratio. However, the V - 4.01a/o Nb specimens do not fit the empirical curves found for the vanadium-gallium alloys.

Except for the transition region, there is not much difference in the form of the pinning force of the low-κ pure vanadium specimens, and the high-κ alloys. For most of the regions, the pinning force can be described as varying with the inverse of κ_1 squared.

New studies on pinning should be directed in another, maybe more practical direction; pinning by vanadium-carbide precipitates has little, if any, practical application. A pinning center with

a broader range of values for ρ and ρV is desirable. Voids are currently used for this reason [54,55] and, in addition, voids are not affected by the proximity effect.

Pinning by crystal dislocations caused by cold working the material, is currently the main source of pinning in most commercial superconductors. During the microstructural analysis of our specimens it was observed that the carbon in solid solution tends to accumulate along crystal grain boundaries. If carbon also accumulates along the dislocations caused by cold work of the material, this accumulation can be used to enhance the pinning force caused by these defects, thus providing a valuable research tool.

BIBLIOGRAPHY

1) E.J. Kramer, J. Appl. Phys., 44, 1360 (1973).

2) A.J. Marker, Fluxoid Pinning by Vanadium Carbide precipitates in Superconducting Vanadium, Ph.D. thesis, The Pennsylvania State University (1977).

3) H. Kamerlingh Onnes, Commun. Kamerling Onnes Lab. Univ. Leiden. 122b (1911).

4) W.A. Fietz, and W.W. Webb, Phys. Rev., 178, 657 (1969).

5) M. Tinkham, Introduction to Sueprconductivity, McGraw-Hill, Inc., New York (1975).

6) C.G. Kuper, An Introduction to the Theory of Superconductivity, Clarendon Press, Oxford (1968).

7) D. Saint-James, G. Sarma, and E.J. Thomas, Type II Superconductivity, Pergamon Press, Oxford (1969).

8) P.R. Huebener, Magnetic Flux Structures in Superconductors, Springer-Verlag, Berlin (1979).

9) A.M. Campbell and E.J. Evetts, Critical Currents in Superconductors, Taylor & Frances LTD, London (1972).

10) R. Radebaugh and P.H. Keesom, Phys. Rev., 149, 209 (1966).

11) W. Meissner and R. Ochsenfeld, Naturwiss., 21 787 (1933).

12) C.J. Gorter and H. Casimir, Physica, 1, 306 (1934).

13) F. London and H. London, Proc. Roy. Soc. (London), A149, 71 (1935).

14) A.B. Pippard, Proc. Roy. Soc. (London), A216, 547 (1953).

15) T.E. Faber and A.B. Pippard, Proc. Roy. Soc. (London), A231, 336 (1955).

16) J. Bardeen, L.N. Cooper, and J.R. Schrieffer, Phys. Rev., 108, 1175 (1957).

17) V.L. Ginzburg and L.D. Landau, Zh. Eksp. Teor. Fiz., 20, 1064 (1950). English translation in Men of Physics: L.D. Landau, Vol. I, (D. ter Haar, Ed.), Pergamon Press, Oxford (1965).

18) L.D. Landau and E.M. Lifshitz, Statistical Physics, Pergamon Press, Oxford (1958).

19) L.D. Gor'kov, Zh. Eskp. Teor. Fiz., 36, 1918 (1959). English translation in Soviet Phys. - JETP, 9, 1364 (1959).

20) B.B. Goodman, IBM J. Res. Dev., 6, 63 (1962).

21) A.A. Abrikosov, Sov. Phys. - JETP, 5, 1174 (1957).

22) F. London, Superfluids, Vol. I, John Wiley & Sons, Inc., New York (1950).

23) R. Labush, Phys. Stat. Sol., 32, 439 (1969).

24) Y.B. Kim, C.F. Hempstead, and A.R. Strnad, Phys. Rev. A, 139, 1163 (1965).

25) J. Schelten, H. Ullmaier, and G. Lippmann, Phys. Rev., 139A, 1163 (1965).

26) P.W. Anderson, Phys. Rev. Lett., 9, 309 (1962).

27) E. Schneider, J. Low Temp. Phys., 29, 573 (1977).

28) E.J. Kramer, Report #4142, Mater. Sci. Center, Cornell Univ. (1979).

29) M. Fähnle, Phys. Stat. Sol. (b), 83, 433 (1977).

30) R.L. Schuyler, The Preparation and Characterization of Carbide Containing Samples to Study Vortex Pinning in Superconducting Vanadium, Ph.D. thesis, The Pennsylvania State University (1975).

31) P.G. DeGennes, Superconductivity of Metals and Alloys, W.A. Benjamin, Inc., New York (1966).

32) D. Dew-Hughes, Philos. Mag., 30, 293 (1974).

33) R. Labush, Cryst. Lattice Defects, 1, 1 (1969).

34) E.J. Kramer, J. Appl. Phys., 41, 621 (1970).

35) R. Schmucker, Phys. Stat. Sol. (b), 80, 89 (1977).

36) J.H.N. van Vucht, H.A.C.M. Bruming, H.C. Donkersloot, and A.H. Gomes de Mesquita, Philips Res. Rep., 19, 407 (1964).

37) A.I. Golovashkin, I.S. Levchenko, I.E. Leksina, G.P. Motulevich, and A.A. Shubin, JETP Letters (USA), 10, 328 (1969).

38) A.I. Golovashkin, I.S. Levchenko, and G.P. Motulevich, Sov. Phys. JETP, 30, 44 (1970).

39) V.M. Pan, Yu. I. Beletskiy, V.S. Flis, S.A. Firstov, and G.F. Sarzhan, Fiz. Metal. Metalloved., 40, 281 (1975).

40) F.G. Brickwedde, Physica, 24, S128 (1958).

41) V.M. Azhazha, N.V. Volkenshteym, V. YE. Startsev, V.A. Finkel', V.I. Cherepanov, and B.P. Chernyy, Fiz. Metal. Metalloved., 41, 1188 (1976).

42) J. Bass, Adv. in Phys., 21, 431 (1972).

43) W.D. Jung, F.A. Schmidt, and G.C. Danielson, Phys. Rev. (B), 15, 659 (1977).

44) C.L. Tsai, R.L. Fagaly, H. Weinstock, and F.A. Schmidt, Phys. Rev. (B), 23, 6430 (1981).

45) N.N. Sirota and E.A. Ovseichuk, Sov. Phys. Doklady, 12, 516 (1967).

46) J.M. Corsan and A.J. Cook, Phys. Stat. Sol. 40, 657 (1970).

47) J.A. Waynert, H. Salvo, and M. Levy, Phys. Rev. (B), 10, 1859 (1974).

48) C. Baker and J. Sutton, Phil. Mag., 19, 1223 (1969).

49) A.M. Campbelll, J. Phys. C, 4, 3186 (1971).

50) M. Steingart, A.G. Putz, and E.J. Kramer, J. Appl. Phys., 44, 5580 (1973).

51) C.C. Koch, A. DasGupta, D.M. Kroeger, and J.D. Scarbrough, Phil. Mag. (B), 40, 361 (1979).

52) K.M. Ralls, A.L. Donlevy, R.M. Rose, and J. Wulff, Weld. J. (S), 42, S411 (1963).

53) K.E. Osborne and E.J. Kramer, Phil. Mag., 29, 685 (1974).

54) P.H. Kes, D. de Klerk, G.P. van der Mey, and J. Bressers, J. Nuc. Mater., 72, 40 (1978).

55) E.J. Kramer, J. Nuc. Mater., 72, 5 (1978).

56) E.J. Kramer, J. Appl. Phys., 49, 742 (1978).

VITA

Pedro J. Javier was born in Mayaguez, Puerto Rico, on May 31, 1953. He received a Bachelor of Science degree in Physics from the University of Puerto Rico at Mayaguez. He participated in the Brookhaven National Lab Summer Program in 1974, where he worked on transition-radiation detectors.

DISTRIBUTION LIST FOR TM 81-182

Commander (NSEA 0342)
Naval Sea Systems Command
Department of the Navy
Washington, DC 20362

Copies 1 and 2

Commander (NSEA 9961)
Naval Sea Systems Command
Department of the Navy
Washington, DC 20362

Copies 3 and 4

Defense Technical Information Center
5010 Duke Street
Cameron Station
Alexandria, VA 22314

Copies 5 through 10